MEASUREMENT OF HIGH-MASS DIMUON PRODUCTION FOR P+P AND P+D COLLISIONS WITH 120 GEV PROTON BEAM AT FERMILAB

BY

SHIVANGI PRASAD

DISSERTATION

Submitted in partial fulfillment of the requirements
for the degree of Doctor of Philosophy in Physics
in the Graduate College of the
University of Illinois at Urbana-Champaign, 2020

Urbana, Illinois

Doctoral Committee:

Professor Douglas H. Beck, Chair
Professor Jen-Chieh Peng, Director of Research
Professor Scott S. Willenbrock
Professor Brian D. Fields

Abstract

SeaQuest is a fixed-target experiment at Fermilab using 120 GeV proton beam from the Main Injector. High-mass muon pairs from the interaction of proton beam with various liquid and solid targets were detected in a newly constructed spectrometer. The primary goal of the experiment is to study the sea quark contents in nucleons and nuclei. In particular, the Drell-Yan cross section ratios for liquid deuterium over hydrogen will allow the measurement of sea quark asymmetry, $\bar{d}/\bar{u}$, for Bjorken-x ranging from 0.1 to 0.45, extending the measurements of the previous experiment NuSea/E866. Improved statistics expected at SeaQuest for $x > 0.25$ will allow us to check the surprising behaviour of $\bar{d}/\bar{u}$ at large x observed in NuSea. Additionally, SeaQuest data also provide the opportunity to study other very interesting physics. One such physics is the absolute p+d and p+p Drell-Yan differential cross-section ($M^3 d^2\sigma/dM dx_F$). The measurement of Drell-Yan cross section allows improved constraints on magnitude and shape of sea and valence parton distribution functions (PDFs). In particular, the p+d measurement is sensitive to the $\bar{d}(x) + \bar{u}(x)$ distribution. This quantity is required for extracting $\bar{d}(x) - \bar{u}(x)$ from $\bar{d}(x)/\bar{u}(x)$. The current global PDFs for light sea quarks are very poorly constrained beyond Bjorken-$x > 0.3$. SeaQuest coverage in dimuon mass ($M_{\mu^-\mu^+}$) ranging from 4.2 GeV to 8.8 GeV (equivalently $\sqrt{\tau}$ in range 0.3 to 0.9) and Feynman-x (x_F) ranging from 0 to 0.8 will extend the measurement from NuSea. Current results are presented in chapter 5. A comparison of E866 p+d and E772 p+d measurement is presented in chapter 8

The transverse momentum dependence of the Drell-Yan cross sections has also been presented. Results on double differential cross sections ($d^2\sigma/dM dp_T$ and $d^2\sigma/dx_F dp_T$) from p+d and p+p Drell-Yan data from SeaQuest are presented in chapter 7. The analysis of p_T distribution from SeaQuest data will provide the value of $< p_T >$ for the lowest value of $\sqrt{s}$ in the study of dependence of $< p_T >$ on $\sqrt{s}$. Additionally, p_T data from existing Drell-Yan experiments have been analysed and compiled systematically to study possible dependence such as $< p_T >$ on x_F and $M_{\mu^-\mu^+}$ of dimuon. The only published result on the dependence of $< p_T >$ on x_F has been reported by pion induced Drell-Yan experiment, E615. This thesis presents the dependence of $< p_T >$ on x_F for proton-induced Drell-Yan data from E866 and E906.

To Mummy and Papa,

Thanks for being courageous enough to support my decision to travel half way across the globe to pursue Ph.D.

Acknowledgments

This thesis is a cumulative effort of several individuals who provided me the motivation, guidance, and strength to keep moving and enjoy graduate school. I would like to take this opportunity to thank them for their love, care and support, without which it would not have been possible to achieve this milestone.

I wish to extend my sincere thanks to my supervisor, Professor Jen-Chieh Peng, for his continuous support and assistance. His dedicated involvement, constant feedback and valuable discussions at every step have helped enrich this research. I would also like to express my appreciation for his efforts and encouragement that has helped me learn and develop a broad knowledge and understanding of the field.

I would like to thank all the SeaQuest collaborators for their dedication and hard work which is instrumental in the completion of this thesis. Special thanks to my senior colleagues at UIUC: Evan, Bryan D., Bryan K. and Markus for always willing to help understand experimental and technical details. Also, many thanks to my fellow lab-mates, Jason and Hugo, for productive and detailed discussions on analysis techniques. I owe a special thanks to my dear friend and colleague, Mae, for her immense support and help when I moved to Fermilab.

I would like extend my heartfelt gratitude to the administrative staff at Loomis, especially Mike and Wendy, for taking care of all the important paper-works and always willing to help graduate students in every possible way.

A huge thanks and gratitude to all my friends, Mansi, Harpreet, Harshala, Ravi, Nikita and Atul, for being my family away from home and making my stay in Urbana-Champaign memorable.

I would like to extend my gratitude to my family for their constant cheering and belief that kept me going. Special thanks to my brother, Rituraj, for always being there with words of encouragement throughout my Ph.D.

Lastly, I would like to extend my heartfelt gratitude to my friend and loving husband, Shubhanshu, who stood by my side at every stage of Ph.D. His companionship has taught me to navigate positively through every situation with a smile.

Table of Contents

List of Tables

List of Figures

Chapter 1

Introduction

1.1 100 years of proton

The famous gold-foil scattering experiment, conducted by Rutherford along with Marsden and Geiger in 1909, showed that atoms constituted of positively charged dense core (nucleus) orbited by negatively charged electrons, thus implying that atom is divisible [9]. Following the discovery of atomic nucleus, Rutherford conducted series of experiments by bombarding alpha particle on several materials and observed that a particle (named as H-particle initially) was produced. In subsequent years these observations led to the discovery of protons in 1919 - 1920 [10].

$$\alpha + {}^{14}N \rightarrow p + {}^{17}O \tag{1.1}$$

The Rutherford's model of atom consisted of protons and electrons thus explaining the observations from alpha-particle scattering experiments. However, this model was not able to explain why the mass of nucleus was almost twice of what can be accounted for by the mass of protons itself. This contradiction led the scientists to speculate that the nucleus also contained neutral particles with similar mass as proton. The discovery of neutron by James Chadwick in 1932 [11] was an important step towards the understanding of atomic nucleus. The discovery of proton and neutron (collectively known as nucleon) was just the beginning. In the following decades, with the study of cosmic rays it was clear that the universe consisted of plethora of 'elementary' particles hinting towards the existence of even smaller sub-particles that made up the observed 'elementary' particles. In an attempt to organize the large number of observed particles, Murray Gell-Mann proposed the 'Eightfold Way' in early 1960s which classified these particles (now known as hadrons) in groups of eight, based on unitary symmetry. The hadrons were sub-divided into two class, baryons (or the heavy hadrons) and mesons (lighter hadrons). See figure 1.1.

In 1964, Gell-Mann[12] and Zweig[13, 14] independently proposed the existence of fractionally charged point particle called quarks held together by strong force. At the time, this idea was considered more as a

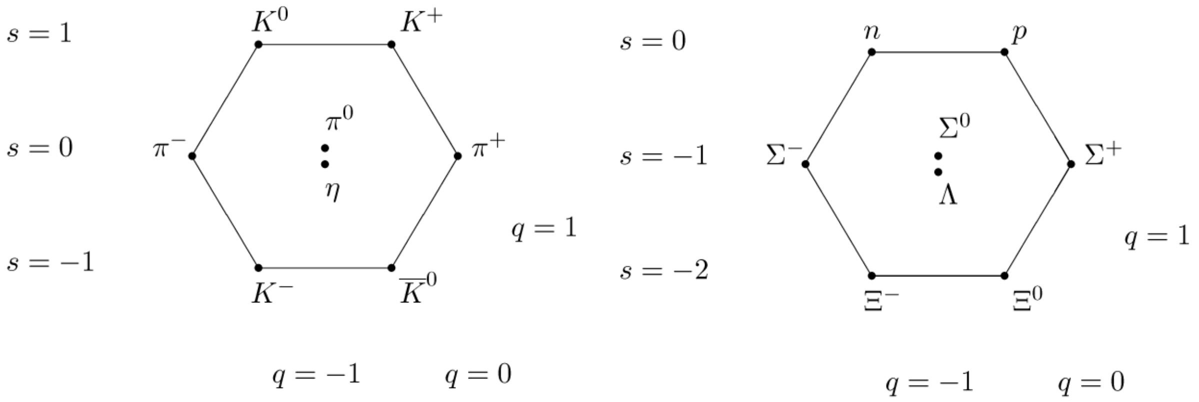

Figure 1.1: Meson (left) and baryon(right) octet

mathematical construct to arrange hundreds of observed hadrons. In late 1960s, scattering experiments at SLAC (Stanford Linear Accelerator) began to reveal a much richer picture of proton, the spatial distribution of charge and current inside it, thus requiring the scattering cross-section to include the structure functions. The structure function can depend on the scale of interaction which is essentially the momentum-squared of the virtual photon. They also depend on a kinematic variable x which is a measure of the inelasticity of the scattering reaction. A striking finding at SLAC[15] showed that for large momentum transfers, the structure functions were independent of Q^2 (a phenomenon later termed as 'scaling' [16]), which would be only possible if the electrons were scattering off point particles. The scattering in this regime is termed Deep Inelastic Scattering (DIS) discussed in more detail in section 1.2. The SLAC experiment also revealed that these point particles have spin 1/2. The observations at SLAC confirmed the existence of fractionally charged point-particles inside protons. Feynman proposed the parton model to explain the scaling phenomenon. According to parton model, the hadron is treated in 'infinite-momentum' frame which is a valid approximation only at high energies. The choice of this frame Lorentz contracts the hadron and the partons do not interact among themselves. In the case of DIS the interaction of high-energy photons can be described as an incoherent sum of photon-parton interaction. At the time it was not immediately clear that Gell-Man's quark and Feynman's parton are the same entities. With further scattering experiments and the development of theory of strong interaction QCD (Quantum Chromodynamics), quarks in the Quark model were identified as partons in Feynman's parton model.

1.2 Deep Inelastic Scattering

The evidence of point-like constituents in nucleons was first observed using deep inelastic scattering (DIS) in which high energy lepton is inelastically scattered off a nuclear target [17]. It is an extension of Rutherford's scattering to high energy, thus providing much finer resolution for probing the internal structure of nucleons. The differential cross section for DIS is given as

$$\frac{d\sigma}{dE'd\Omega} = \frac{\alpha^2}{4E'\sin^4\frac{\theta}{2}}\left[\frac{1}{\nu}F_2(x,Q^2)\cos^2\frac{\theta}{2} + \frac{1}{M}F_1(x,Q^2)\sin^2\frac{\theta}{2}\right], \tag{1.2}$$

where E' and θ are energy and angle of scattered lepton in the laboratory frame, M is the mass of nucleon, and ν is the energy transferred by the scattering lepton. Q^2 and x are Lorentz-invariant quantities, namely, $Q^2 = -q^2$, where q is the momentum 4-vector of the exchanged virtual photon, and $x = Q^2/2p.q = Q^2/2M\nu$. $F_1(x,Q^2)$ and $F_2(x,Q^2)$ are the structure functions. The fact that structure functions, F_1 and F_2, become independent of Q^2 and only dependent on a single variable x is known as Bjorken scaling [16]. The scaling behaviour of structure functions implied scattering from point-like charged particle inside nucleon.

As mentioned in Section 1.1 Feynman proposed the parton model in 1969 in order to describe the scaling behaviour observed in the deep inelastic scattering process [18]. According to this model, hadrons are composed of point-like particles called partons (now identified as quarks and gluons). Fig.1.2 shows the Feynman diagram for DIS. In a frame where proton has very large momentum , its constituents will have mostly collinear momentum and each parton of type i has a probability $f_i(x)$ to carry fractional momentum x of the proton. In the parton model, structure functions are expressed in terms of parton distribution functions (PDFs), $f_i(x)$, as shown below

$$F_1(x) = \frac{1}{2}\sum_i e_i^2 f_i(x) \tag{1.3}$$

and

$$F_2(x) = \sum_i e_i^2 x f_i(x), \tag{1.4}$$

where the sum is over quark flavor i with charge e_i. Measurement of DIS cross section, which is expressed in terms of structure functions, is then used to extract PDFs. Fig.1.3 shows a recent extraction of the $f_i(x)$ based on a global fit to existing DIS data and the Drell-Yan data (to be described next).

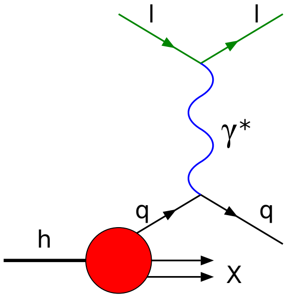

Figure 1.2: Deep inelastic scattering

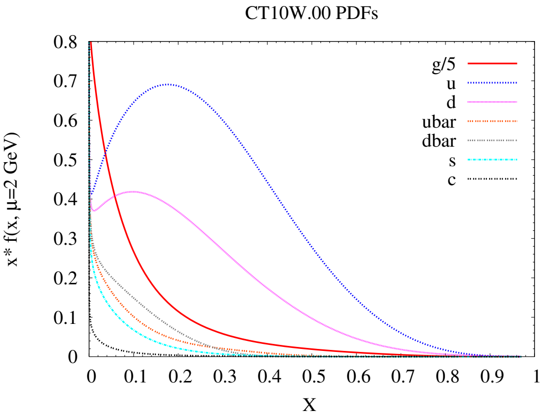

Figure 1.3: Parton distribution functions extracted from DIS and Drell-Yan data

1.3 From DIS to Drell-Yan process

In 1970, soon after the discovery of scaling in DIS Christenson et al. reported the first measurement of massive lepton pairs produced in $p + A$ collision at 29 GeV [1]. Fig.1.4 shows the dimuon mass spectrum with a remarkable drop in the cross section with increasing dilepton mass. Soon after Christenson et al. reported their findings, S. Drell and T.M. Yan proposed a mechanism (Fig.1.5) for massive dilepton production [19, 20]. It is an electromagnetic process in which a quark from one hadron annihilates with an antiquark from another hadron to form a virtual photon which then decays into a lepton pair. A comparison between Fig.1.2 and Fig.1.5 shows that the Drell-Yan process is closely connected to the DIS. Both are electromagnetic processes involving an exchange of virtual photon. While the DIS is a t-channel process with an exchange of space-like ($q^2 < 0$) virtual photon, the Drell-Yan is an s-channel process involving a time-like ($q^2 > 0$) virtual photon. While the DIS cross section is usually dominated by the contribution from the abundant valence quarks, Fig.1.5 shows that the Drell-Yan process must involve an antiquark and is a powerful tool to probe the antiquark distributions in the nucleons or nuclei. Another unique feature of the Drell-Yan process is that the parton distribution of mesons and antiproton, which cannot be accessed by DIS, can be measured using meson or antiproton beam via the Drell-Yan process.

1.3.1 Drell-Yan Kinematics

Consider the reaction

$$A + B \rightarrow l^- + l^+ + X, \tag{1.5}$$

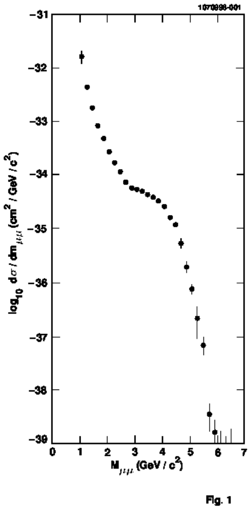

Figure 1.4: Cross section as a function of dimuon mass from [1]

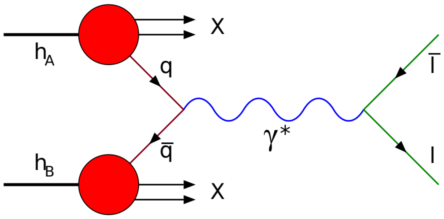

Figure 1.5: Drell-Yan process

where hadron A collides with hadron B, producing a pair of charged leptons, l^- and l^+, together with a collection of undetected particles called 'X'. In the nucleon-nucleon center-of-mass (CM) frame the momenta of the interacting quark and antiquark are respectively, $x_1\sqrt{s}/2$ and $-x_2\sqrt{s}/2$. $\sqrt{s}$ is the CM total energy and $x_1(x_2)$ refers to the momentum fraction of the beam (target) nucleon carried by the quark (antiquark). The energy is given by $x_1\sqrt{s}/2$ and $x_2\sqrt{s}/2$, ignoring the mass of quarks. The dilepton energy, E and longitudinal momentum P_l are obtained straightforwardly as

$$E = \frac{(x_1 + x_2)\sqrt{s}}{2} \tag{1.6}$$

$$P_l = \frac{(x_1 - x_2)\sqrt{s}}{2} \tag{1.7}$$

The experimental observables M and x_F, where x_F is the ratio of P_l over the maximal value of P_l, are related to x_1 and x_2 as

$$M^2 = E^2 - P_l^2 = s x_1 x_2 \tag{1.8}$$

and

$$x_F = \frac{p_l}{p_l^{max}} = \frac{(x_1 - x_2)\sqrt{s}/2}{\sqrt{s}/2} = x_1 - x_2 \tag{1.9}$$

Equivalently, x_1 and x_2 can be calculated from M and x_F as

$$x_1 = \frac{1}{2}[(x_F^2 + 4\frac{M^2}{s})^{1/2} + x_F] \tag{1.10}$$

and

$$x_2 = \frac{1}{2}[(x_F^2 + 4\frac{M^2}{s})^{1/2} - x_F] \tag{1.11}$$

Equations 1.10 and 1.11 show that one could deduce the values of x_1 and x_2 for each Drell-Yan event, simply from the mass and momentum of the detected dilepton.

The cross section for $q\bar{q} \to l^- l^+$ can be calculated from quantum electrodynamics, and is given as

$$\sigma = \frac{1}{3}\frac{4\pi\alpha^2 Q^2}{3M^2}, \tag{1.12}$$

where M is the invariant mass of the dilepton and the color factor 1/3 is to take into account the fact that only quark and antiquark of the opposite colors can annihilate to form a virtual photon, and there is 1 in 3 chance of that happening. At leading order, the Drell-Yan cross section is a convolution of the $q\bar{q} \to l^- l^+$ elementary cross section with the parton densities in the colliding hadrons. Hence, the above equation is multiplied by $q_A(x_1)dx_1$, the probability that a quark in beam hadron A has a momentum fraction x_1, and $\bar{q}_B(x_2)dx_2$, the probability that an anti-quark in target hadron B has a momentum fraction x_2. The differential cross section can then be written as

$$d^2\sigma = \frac{4\pi\alpha^2 Q^2 q_A(x_1)\bar{q}_B(x_2)dx_1 dx_2}{9M^2}, \tag{1.13}$$

where Q is the charge of the annihilating quarks. Similarly, an antiquark from hadron A can annihilate with quark from hadron B. Summing over the quark flavor i, we have

$$\frac{d^2\sigma}{dx_1 dx_2} = \frac{4\pi\alpha^2}{9M^2}\sum_i Q_i^2[q_{i,A}(x_1)\bar{q}_{i,B}(x_2) + \bar{q}_{i,A}(x_1)q_{i,B}(x_2).] \tag{1.14}$$

The above can be rewritten in terms of the measurable quantities M and x_F as

$$\frac{d^2\sigma}{dM^2 dx_F} = \frac{4\pi\alpha^2}{9M^4}\frac{x_1 x_2}{x_1 + x_2}\sum_i Q_i^2[q_{i,A}(x_1)\bar{q}_{i,B}(x_2) + \bar{q}_{i,A}(x_1)q_{i,B}(x_2)], \tag{1.15}$$

which can be rearranged as

$$M^3\frac{d^2\sigma}{dM dx_F} = \frac{8\pi\alpha^2}{9}\frac{x_1 x_2}{x_1 + x_2}\sum_i Q_i^2[q_{i,A}(x_1)\bar{q}_{i,B}(x_2) + \bar{q}_{i,A}(x_1)q_{i,B}(x_2)], \tag{1.16}$$

known as the scaling form of cross section. This form of cross section is independent of beam energy provided it is measured at same value of $x_F(= x_1 - x_2)$ and $\tau(= x_1 x_2)$. An alternative way to write the scaling form of differential equation is to express it in terms of dimensionless variables $\tau = M^2/s$ and rapidity $y = (1/2)ln(x_1/x_2)$ as

$$s\frac{d^2\sigma}{d\tau dy} = \frac{4\pi\alpha^2}{9\tau}\sum_i Q_i^2[q_{i,A}(x_1)\bar{q}_{i,B}(x_2) + \bar{q}_{i,A}(x_1)q_{i,B}(x_2)] \tag{1.17}$$

1.3.2 Successes of naive Drell Yan process

Drell-Yan process was successful in explaining the large drop-off in the cross-section at high mass as is evident from equation 1.15 that cross section is inversely proportional to M^3. It also gave several predictions which were confirmed subsequently in the experiments to follow.

a) Scaling behaviour

As shown in equation 1.16, the scaling form of Drell-Yan cross section is independent of the centre of mass energy $\sqrt{s}$ for a given x_F and τ. This was tested by the CFS collaboration with proton beam at three different beam momenta (200, 300 and 400 GeV/c)[21]. Another experiment carried out at the CERN ISR [5] also verified the scaling behaviour at $\sqrt{s}$ of 44 and 62 GeV. Scaling results are shown in Figure 1.6

b) Decay angular dependence

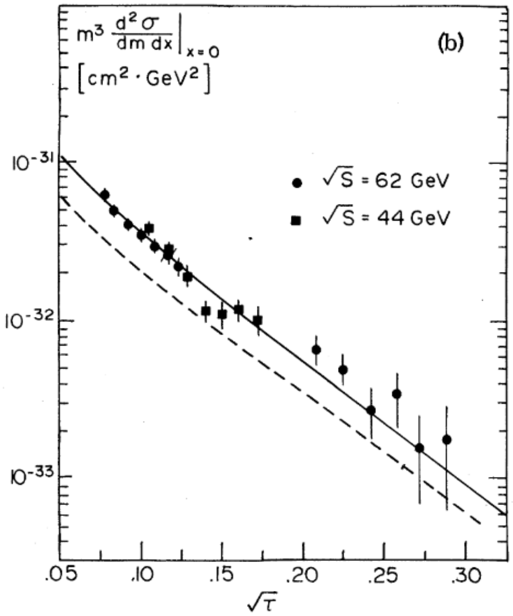

Figure 1.6: Scaling form of cross section plotted as a function of $\sqrt{\tau}$ for $\sqrt{s} = 44$ and $62 GeV/c$

Another important initial success of Drell-Yan prediction was the shape of angular distribution of the produced dileptons. If the lepton pair is produced from head-on collision of quark and anti-quark, the angular distribution would have the same shape as in case of $e^-e^+ \rightarrow \mu^-\mu^+$, that is, $1 + cos^2\theta$. Here, θ is the angle of

μ^+ in the dilepton rest frame. Such a dependence on θ was first observed in several early experiments [22, 23].

1.3.3 Inadequacies of naive Drell-Yan process

Despite making successful predictions, the naive Drell-Yan process was still inadequate in explaining certain observations.

a) Transverse momentum distribution

The averaged transverse momentum of the observed dileptons was too large (>1 GeV/c) [24] to be explained by the naive Drell-Yan process. According to the naive Drell-Yan process, the dilepton transverse momentum should be the vector sum of the intrinsic transverse momentum of the annihilating quark and anti-quark. The mean transverse momentum of the quarks due to fermi motion is $\sim 0.35 GeV/c$ which is much smaller than the observed $< p_T >$ of the dileptons. This discrepancy indicated that naive Drell-Yan process was not enough to explain all the observation.

b) Absolute cross section

A second observation that indicated an adequacy in the naive Drell-Yan process was the absolute cross section. The data from several experiments [24] showed that the prediction was about a factor 2 lower than the observation. Table 1.1 shows a tabulation of the ratio of measured to predicted cross-section ($K = \sigma_{measured}/\sigma_{naiveDY}$) from various experiments[4].

Experiment	Beam+Target	Beam momentum (GeV/c)	$K = \sigma_{meas.}/\sigma_{naiveDY}$
E288	$p + Pt$	300/400	~1.7
WA39	$\pi^{\pm} + W$	39.5	~ 2.5
E439	$p + W$	400	1.6±0.3
NA3	$\bar{p} + Pt$	150	2.3±0.4
	$p + Pt$	400	3.1±0.5±0.3
	$\pi^{\pm} + Pt$	200	2.3±0.5
	$\pi^- + Pt$	150	2.49±0.37
	$\pi^- + Pt$	280	2.22±0.33
NA10	$\pi^- + W$	194	~2.77±0.12
E326	$\pi^- + W$	225	2.70±0.08±0.40
E537	$\bar{p} + W$	125	2.45±0.12±0.20
E615	$\pi^- + W$	252	1.78±0.06

Table 1.1: K factors ($\sigma_{meas.}/\sigma_{naiveDY}$) for previous Drell-Yan cross section measurements

1.4 Quantum Chromodynamics

Gell-Mann's quark model was successful in explaining that the large number of observed hadrons are not fundamental particles, instead they consist of fractionally charged spin 1/2 elementary particles. However, there were two puzzles that this model was unable to explain: Why were free quarks not observed and the existence of Δ^{++} baryon (which consists of three up quarks each with spin +1/2, which will have symmetric wavefunction, hence, violating the Pauli's exclusion principle). To solve this puzzle, a new quantum number 'color' was proposed. The existence of 'color' quantum number would satisfy Pauli's exclusion principle in case of Δ^{++} baryon by assigning three different colors (red (r), green(g), blue(b)) to the three u quarks. It should be noted that color quantum number has to satisfy the following two conditions to address the problem: i) the quarks must carry at least three different types of colors, ii) the quark wavefunction must by anti-symmetric (for the total wavefunction of Δ^{++} to be anti-symmetric).

To address the issue of non existence of free quarks, the concept of 'color confinement' was proposed, according to which all observed hadrons are 'colorless' combination of quarks. Thus, baryons are formed with three quarks in color neutral combination (rgb) and mesons in color-anticolor combinations ($r\bar{r}$, $g\bar{g}$, $b\bar{b}$). On the other hand, the SLAC experiment revealed that for very high energy interaction (high Q^2), the quarks behave freely. A quantum field theory must contain both features: i) strong enough at large length scales such that the quarks always occur in bound states, ii) weak enough at small length scales such that quarks behave nearly free. Amongst all the rapid developments to understand the theory of 'strong' force, it was the discovery of asymptotic freedom by Frank Wilczek, David Gross[25] and David Politzer[26], that Quantum Chromodynamics (QCD) was established as the correct theory of strong interactions.

QCD differs from the field theory for electromagnetic interactions, QED, in many aspects. The electric charge equivalent in QCD is 'color' charge. However, unlike electric charge there exists three types of color charge (r,g,b). The strong force is mediated by vector bosons, called gluons which also carry color charge, unlike QED where the mediator, virtual photon is electrically neutral. The fact that gluons carry color charge makes QCD crucially different from QED. The strength of the strong force and its dependence on the length scale can be qualitatively understood as follows. A quark is surrounded by virtual gluons appearing due to the quantum fluctuations, which is similar to vacuum polarization (charge anti-charge pairs) in case of electric charge. The electric charge is 'screened' because of the presence of charge-anticharge pairs around it. The bare charge is only revealed in high energy measurements which probes short-length scales. The dependence of the strength of the force on the probed length scale is termed as 'running coupling constant' $\alpha(Q^2)$. Similar screening effect of the color is also observed. However, in case of strong interactions the gluons themselves carry color. The quark is continuously emitting and reabsorbing the gluons which possess the property to carry away its color (referred as ‘anti-screening’). Therefore, unlike electromagnetic force, the strength of strong force decreases with decrease in anti-screening effects at high energy or short-length scales. This phenomenon is termed asymmptotic freedom.

1.5 QCD corrections

The inadequacy of naive Drell-Yan process to explain the large dilepton p_T and the discrepancy between data and theory on cross section suggested the importance of QCD. Bringing QCD into the picture allowed the emission and absorption of gluons by quarks and anti-quarks. The hard gluons emitted by quarks can impart large transverse momentum, thus explaining the large observed p_T in early Drell-Yan experiments. Additionally, with the inclusion of gluons, higher order feynman diagrams will also contribute to the total cross-section. The next-to-leading order (NLO) diagrams that would contribute to the process are subdivided into 3 categories, namely, gluon bremstrahlung, gluon Compton scattering and vertex correction (interference term). The gluon bremstrahlung is still a $q\bar{q}$ interaction, with either quark or anti-quark emitting a gluon before annihilating into a virtual photon as shown in Figure 1.7. The gluon Compton scattering is different in terms of initial state interaction. In this case, a quark or anti-quark scatters off a gluon to produce a virtual photon (Figure 1.8). These two subprocesses contribute to large p_T of the virtual photon and eventually the dileptons. Specifically, the Compton process is more dominant when $p_T > M/2$, implying that at high p_T Drell-Yan events are more sensitive to gluon distribution than anti-quark distribution [27] inside the nucleon. The third type of contribution is the vertex correction or the interference term (Figure 1.9) which comes from the cross term between $O(\alpha_s^0)$ and $O(\alpha_s^2)$. As depicted in Figure 1.9, the initial and final states are the same for both diagrams and should be added coherently.

Figure 1.7: Gluon Bremstrahlung $q\bar{q}g$

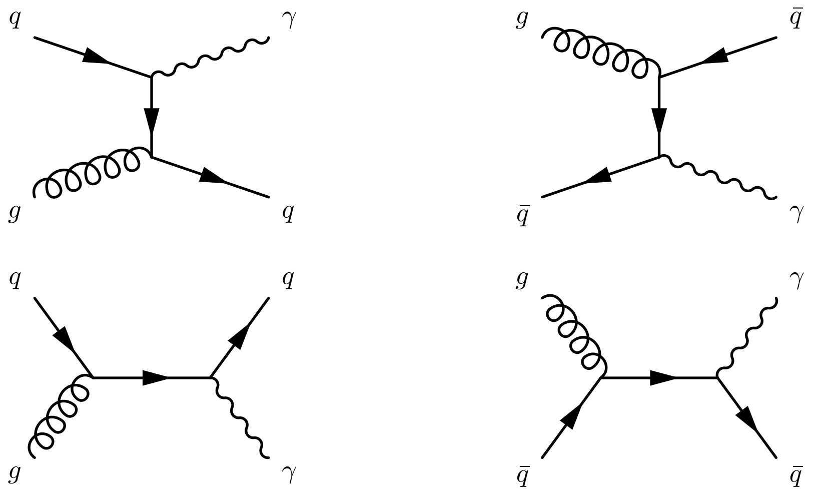

Figure 1.8: Gluon compton scattering (qg or $\bar{q}g$)

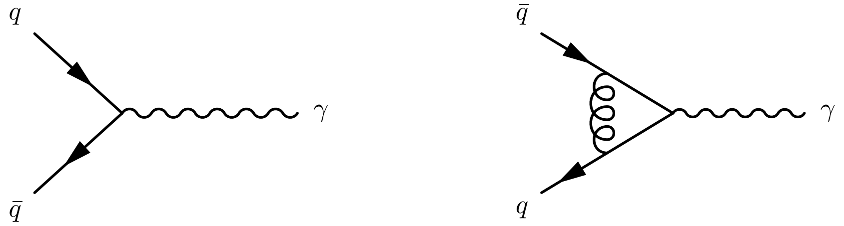

Figure 1.9: Vertex correction or interference term

1.6 Probing the flavor structure of nucleon

The earliest parton model assumed that the proton sea was flavor symmetric ($\bar{u}(x) = \bar{d}(x) = \bar{s}(x)$), even though the valence quark distributions are clearly flavor asymmetric ($u(x) \sim 2d(x)$). The assumption of sea-quark flavor symmetry was not based on any known physics principles. Indeed, the strange-quark sea was later found to be only about half of the up or down quark sea. This flavor asymmetry was attributed to the heavier strange-quark mass, suppressing the gluon splitting to quark-antiquark process $g \rightarrow q\bar{q}$ for the strange quarks. The similarity between the u and d quark masses suggests that the proton's sea should be nearly up-down symmetric, since the $g \rightarrow u\bar{u}$ and $g \rightarrow d\bar{d}$ processes should occur with very similar probabilities. It is important to note that proton contains two u valence quarks and only one d valence quark. This up-down asymmetry could lead to asymmetry in the $\bar{u}$ and $\bar{d}$ sea quark distributions. The quest to understand the light sea quark asymmetry led to several experiments. New Muon Collaboration (NMC) carried out a DIS experiment to extract the Gottfried integral by scattering muons off proton and deuteron targets. Their results indicated that indeed there exists asymmetry between $\bar{d}$ and $\bar{u}$. This result motivated physicists at CERN to conduct another experiment (NA51) using the complementary Drell-Yan process to verify this observation. Their results also confirmed the NMC observation that $\bar{d} > \bar{u}$. However, NA51 spectrometer acceptance was limited to a region of $x = 0.18$. NuSea/E866 experiment at FermiLab was designed to study the dependence of $\bar{d}/\bar{u}$ on x ranging from 0.04 to 0.3. The results from E866 are shown in figure 1.10, which shows an intriguing dependence of $\bar{d}/\bar{u}$ on x. The ratio rises with x until $x \sim 0.2$ and drops beyond that. In fact, the results indicate that $\bar{u} > \bar{d}$ for the highest x. Due to limited statistics in higher x, it is difficult to arrive at a definitive conclusion. E906/SeaQuest, the successor of E866/NuSea, was proposed to pin down the behaviour of asymmetry at high x region using 120 GeV proton beam. Since the differential cross section at a fixed x_1 and x_2 depends inversely on centre of mass energy squared, s, reducing the beam energy from 800 GeV to 120 GeV provides enhancement of a factor ∼7 in the cross section measurement (see equation 1.14).

Although the flagship measurement of SeaQuest/E906 is to measure the sea-quark asymmetry, the collected data can very well be used to understand other very important physics. This thesis focuses on two topics: absolute Drell-Yan cross-section measurement for p+p and p+d interaction and p_T distribution from SeaQuest data and its comparison with existing Drell-Yan data on transverse momentum distribution.

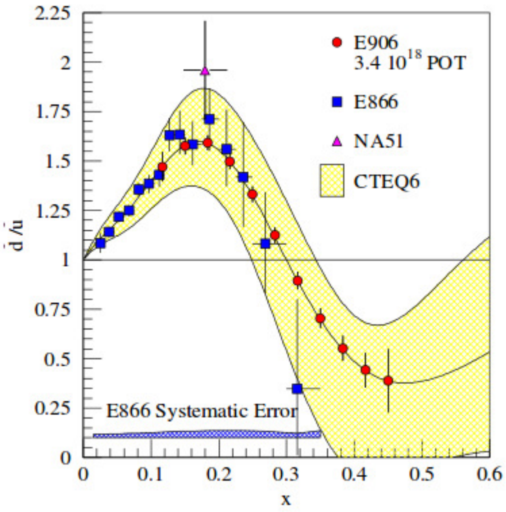

Figure 1.10: $\bar{d}(x)/\bar{u}(x)$ from various experiments and the CTEQ6 global fit. NA51 measured the ratio of $\bar{d}(x)/\bar{u}(x)$ at a single value of x. E866 extended the measurement to a broad range of x. Red dots show projected sensitivity of SeaQuest at 3.4×10^{18} protons on target (POT).

1.6.1 Absolute cross-section measurement

The invariant form of p+p LO Drell-Yan cross section can be written as

$$M^3 \frac{d^2\sigma_{pp}}{dM dx_F} = \frac{8\pi\alpha^2}{9} \frac{x_1 x_2}{x_1 + x_2} \left[\frac{4}{9} u(x_1)\bar{u}(x_2) + \frac{1}{9} d(x_1)\bar{d}(x_2) + \frac{4}{9} \bar{u}(x_1) u(x_2) + \frac{1}{9} \bar{d}(x_1) d(x_2) \right] \tag{1.18}$$

In the above expression, contribution from heavier quarks ($s(x)\bar{s}(x), c(x)\bar{c}(x)$ terms) have been ignored. For large x_F, the terms where the anti-quark is coming from the beam and quark from the target can be ignored. Hence the above equation can be approximately written as

$$M^3 \frac{d^2\sigma_{pp}}{dMdx_F}|_{x_F>>0} \approx \frac{8\pi\alpha^2}{9}\frac{x_1x_2}{x_1+x_2}\left[\frac{4}{9}u(x_1)\bar{u}(x_2)+\frac{1}{9}d(x_1)\bar{d}(x_2)\right]. \tag{1.19}$$

Due to the charge squared weighting factor and the fact that $u(x) \sim 2d(x)$the dominant contribution ($> 80\%$) in p+p Drell-Yan cross-section is the $u(x)\bar{u}(x)$ term. Hence, the p+p data can be used to constrain the $\bar{u}(x)$ distribution. Similarly, the p+d cross-section is written as a sum of p+p and p+n contribution, ignoring the nuclear effects in deuterium. For large x_F, it can be approximated as

$$M^3 \frac{d^2\sigma_{pd}}{dMdx_F}|_{x_F>>0} \approx \frac{8\pi\alpha^2}{9}\frac{x_1x_2}{x_1+x_2}\frac{1}{9}\left[(4u(x_1)+d(x_1))(\bar{u}(x_2)+\bar{d}(x_2))\right] \tag{1.20}$$

The above equation shows that the p+d Drell-Yan data are sensitive to the $\bar{d}(x)+\bar{u}(x)$ distribution in proton, the knowledge of which is required to obtain $\bar{d}(x)-\bar{u}(x)$ from the measurement of $\bar{d}(x)/\bar{u}(x)$. The quantity $\bar{d}(x)-\bar{u}(x)$ is a measure of the non-perturbative contribution to the nucleon sea as perturbative processes are known to produce almost symmetric sea ($\bar{d}(x) \sim \bar{u}(x)$)[28].

Uncertainty bands from NNPDF3.0[29] for $u(x)$ and $d(x)$ quark distributions plotted in Figure 1.11 show that $u(x)$ and $d(x)$ are reasonably well constrained at least up to $x = 0.7$ and $x = 0.5$, respectively. On the contrary Figure 1.12 shows that $\bar{u}(x)+\bar{d}(x)$ is constrained only up to $x = 0.3$. Data from HERA, E605 and E866 [30, 4] constrained the sea quark distributions at low x. However, there are no measurements to constrain them at intermediate x. SeaQuest data will be able to improve the constraints on light sea-quark PDFs in this region.

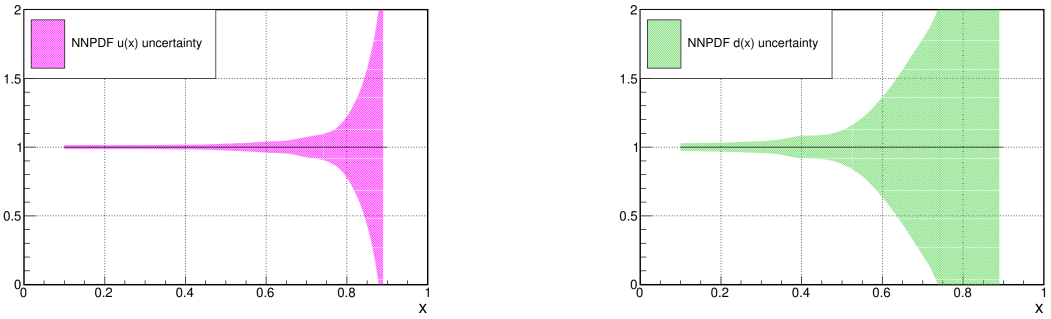

Figure 1.11: NNPDF 3.0 (NLO) uncertainty band for $u(x)$ and $d(x)$ quark distributions at Q=5 GeV

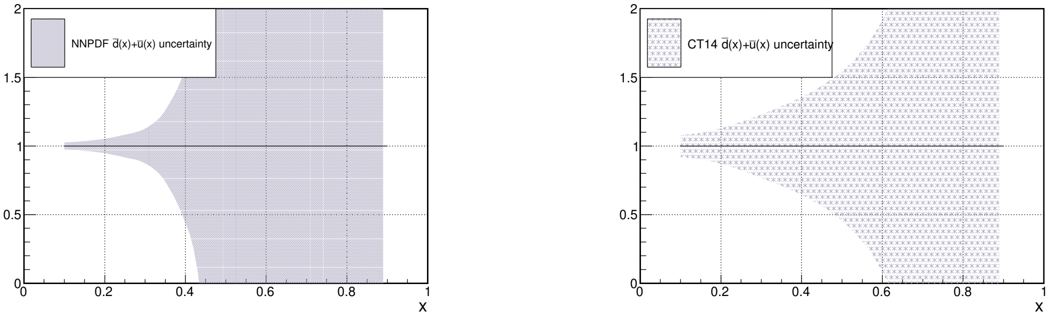

Figure 1.12: NNPDF 3.0 (NLO)(left) and CT14 (NLO)(right) uncertainty band for $\bar{u}(x) + \bar{d}(x)$ quark distribution at Q=5 GeV

1.6.2 Drell-Yan p_T distribution

The parton distribution functions (PDFs) describe the distributions of quarks and gluons as a function of Bjorken-x which is the longitudinal momentum fraction of the hadron carried by the quark. Hence, PDFs provide a single dimension picture of the nucleon structure. To get a 3-dimensional picture of the parton momentum, it is important to understand the momentum of partons in transverse direction. These types of generalized three dimensional PDFs are referred to as Transverse Momentum Dependent PDFs (TMD PDFs). Measurements from various experiments using different mechanisms are useful resources in testing the universality of PDFs and TMD PDFs.

While the study of TMD in general requires transverse polarization of the beam and/or target, SeaQuest can provide useful information on the p_T distributions of the Drell-Yan cross section. In LO Drell-Yan, the p_T distribution reflects the intrinsic k_T distribution of the interacting quarks and antiquarks. When gluon emission is taken into account in the higher-order Drell-Yan, the p_T distribution is expected to broaden. A study of p_T distribution in unpolarized Drell-Yan could probe both quark/antiquark's k_T distribution and the effect of QCD from gluon emission.

Double differential cross sections $d^2\sigma/dMdp_T$ and $d^2\sigma/dx_F dp_T$ from SeaQuest have been analyzed and preliminary results on possible dependence of $< p_T >$ on x_F and M will be presented. The SeaQuest data provide a unique opportunity to explore the p_T distribution at lowest $\sqrt{s}$ amongst other existing p_T data. Additionally, a systematic study of p_T distribution from existing Drell-Yan data will also be presented.

Chapter 2

SeaQuest experimental setup

The E906 apparatus is designed to measure high energy muons produced in forward rapidity region from interaction of 120 GeV proton beam with various targets. Figure 2.1 shows a schematic of the E906 spectrometer. The positive z is chosen along the beam direction, positive y-axis points upward and positive x-axis is oriented to form a right-handed coordinate system. The origin of the coordinate system is at the centre of the front face of the upstream magnet (FMAG). Muons produced from the interaction of proton beam with liquid or solid targets go through the FMAG, which bend muons horizontally (along x-axis). The FMAG also serves as a beam dump and a hadron absorber. Further downstream, there are four tracking stations. Each station is equipped with hodoscope arrays and tracking devices. The fast signals from hodoscopes at each station are used for events triggers. Additionally, the first 3 stations comprise of drift chambers

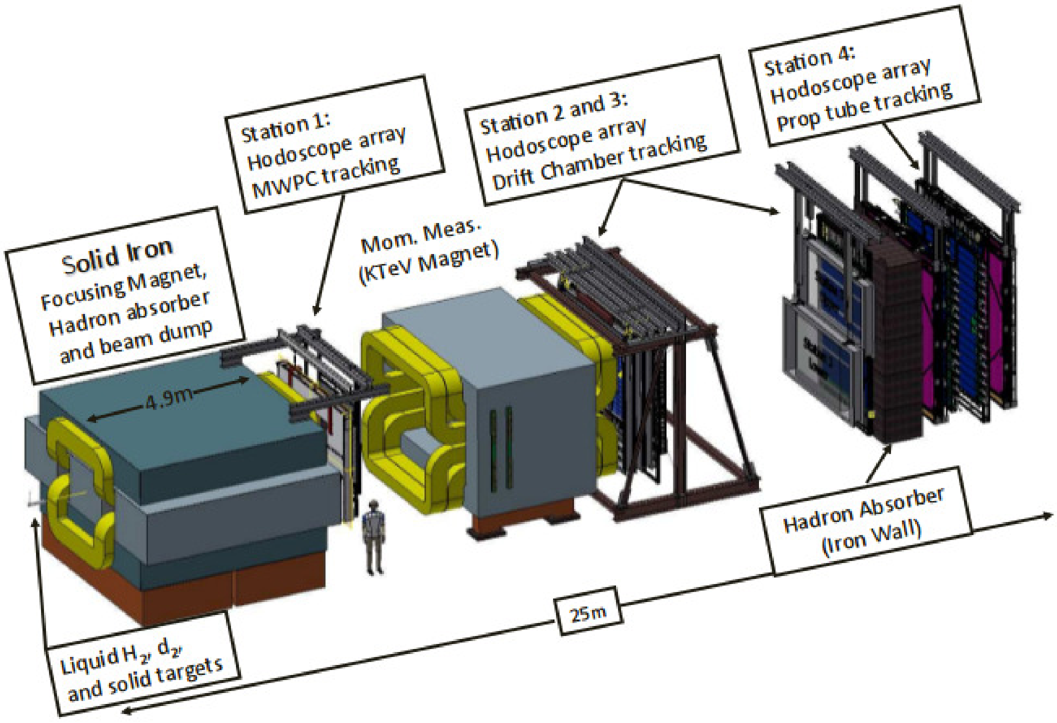

Figure 2.1: Schematic of SeaQuest spectrometer

and the fourth one contains proportional tubes. The drift chambers provide high spatial resolution required for precise track reconstruction. In between stations 1 and 2, there is an analysing magnet (KMAG) for measuring the momentum and charge of the muon tracks. In between stations 3 and 4, there is a 1 meter thick iron wall which absorbs background hadrons. Energetic muons can penetrate this wall. Hence, station 4 is used for muon identification.

Details about the beamline, targets, and different components of the spectrometer are described in more details in the following sections.

2.1 Proton Beam

2.1.1 Main injector

The accelerator complex at FermiLab is shown in Figure 2.2. SeaQuest receives 120 GeV/c proton beam from the Main Injector (MI). Before reaching the Main Injector, proton beam goes through the following stages:

1) An ion source generates 35 KeV proton beam by accelerating ionized hydrogen with a static electric field.

2) A Radio Frequency Quadrupole (RFQ) accelerates the beam to 750 KeV and bunches them into 2 ns long buckets, each separated by 18.9 ns, which is a direct result of the operating frequency 53.1 MHz of RFQ

3) The beam then enters the linear accelerator (or Linac) where it is accelerated to 400 MeV, preparing protons for booster accelerator.

4) The booster accelerator is a circular ring of approximately 1500-foot circumference where the energy of the beam is ramped to 8 GeV. A set of 84 RF buckets called 'booster batch' is inserted into the Recycler for the next phase of acceleration. Typically, 6 booster batches are inserted into the Recycler.

5) The Recycler is a 2 mile circumference ring where the proton beam can be 'slip stacked', i.e., booster batches can be inserted on top of one another, hence more intense proton beam can be produced. Recycler has the capacity to hold 588 RF bucket(7 booster batches), however only 494 (6 booster batches) of them are filled. The remaining buckets are intentionally left vacant to serve as abort gap.

6) The proton beam then reaches the Main Injector, which is the final stage before it gets delivered to SeaQuest. The MI sits right beneath the Recycler in the same tunnel and accelerates the proton beam from 8GeV to 120 GeV/c.

120 GeV/c proton beam is extracted from the MI over a duration of 4 seconds every minute. This is known as a spill. An electromagnetic septum is used to scrape the beam off MI and deliver it to SeaQuest.

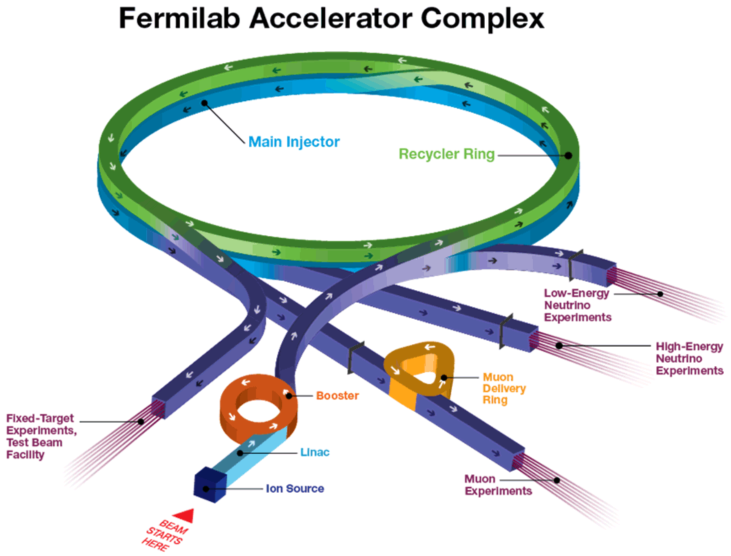

Figure 2.2: Accelerator Complex of FermiLab

This method is known as slow-spill extraction. The extracted beam retains the 53.1 MHz beam structure. The protons arrive in 2 ns bunch, known as an RF bucket, every 18.9 ns during each spill. As described previously there are 588 RF buckets in a single turn. 369k such turns constitute one spill.

$$369k \times 588 \times 20ns \sim 4.1s \tag{2.1}$$

A typical RF bucket has approximately 10^4 protons, which sums upto 2 x 10^{12} protons every second leading to approximately 1 x 10^{13} protons per spill.

2.1.2 Beam intensity monitor

Unfortunately, the slow spill extraction method, does not provide a uniform beam intensity for SeaQuest. The beam intensity distribution peaks at approximately 25k protons per RF bucket. However, some of the buckets have very high intensity (greater than 100k protons per bucket). Such buckets are termed ‘super-buckets’. These types of buckets generate events with a large number of hits on detectors. Hence, triggers are easily satisfied for such events. Once the trigger is satisfied, signals are sent to the Data Acquisition System (DAQ) to start recording the hits. The deadtime of DAQ is proportional to number of hits. Therefore, for such events it generates several hundred microseconds of deadtime for the DAQ. Moreover, for events with very high chamber occupancy, the tracking software has very low efficiency to reconstruct a true signal, if present. To get around this issue, a Beam Intensity Monitor (BIM) was installed at SeaQuest. BIM is a cerenkov counter that outputs fast analog signal proportional to the number of protons. BIM is connected to a QIE (charge integrated encoder) which converts the signal into a digital output. The cerenkov counter is synchronized to main injector RF clock. Whenever the number of protons in the triggering bucket or any of the neighbouring ± 8 RF buckets is higher than the preset value, the BIM sends an inhibit signal to the trigger system to prevent it from firing. Therefore, such high intensity events are not recorded.

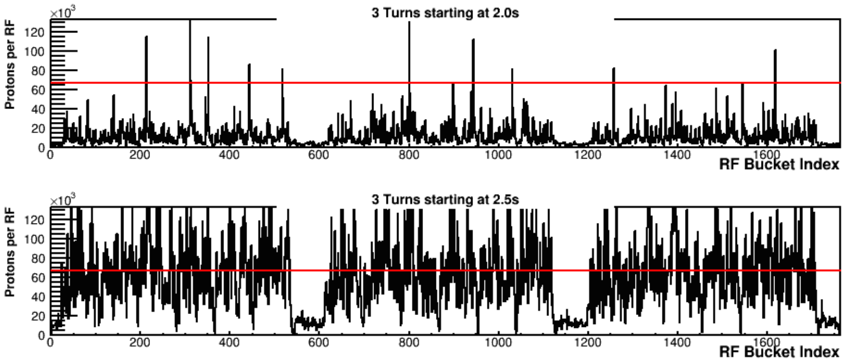

Figure 2.3: A plot showing number of protons per RF bucket as a function of RF bucket number (or time). The red line indicates the threshold setting during the above data taking period. The RF buckets that exceed the threshold are inhibited. The lower panel shows a situation when most of the RF buckets were above the threshold.

A diagram of the BIM is shown in figure 2.4. The cerenkov detector uses Photo Multiplier Tube (PMT) to detect cerenkov light induced by the interaction of proton beam with a gaseous mixture (80% Argon and 20%CO_2) at atmospheric pressure. The cerenkov light produced between baffle and mirror is reflected by the mirror to reach the PMT. Neutral density filters are installed before the PMT to ensure a linear response over the range of instantaneous intensity that SeaQuest receives.

The output signal from PMT is fed into QIE module which integrates and digitizes it. The high timing resolution of the QIE module is capable of measuring the proton intensity for each RF bucket. The BIM measurement is normalized using the Secondary Emmission Monitor (SEM) counter placed upstream of the Cerenkov detector. The SEM itself is caliberated by activation of a thin foil placed in the beam.

Apart from inhibiting triggers when the instantaneous intensity is higher than the threshold, the BIM also provides beam intensity information needed to calculate the live proton on each target during data taking. In particular, it measures

a) integrated beam intensity over each spill (I_{QIE}),

b) integrated beam intensity when trigger inhibit is imposed ($I_{inhibit}$).

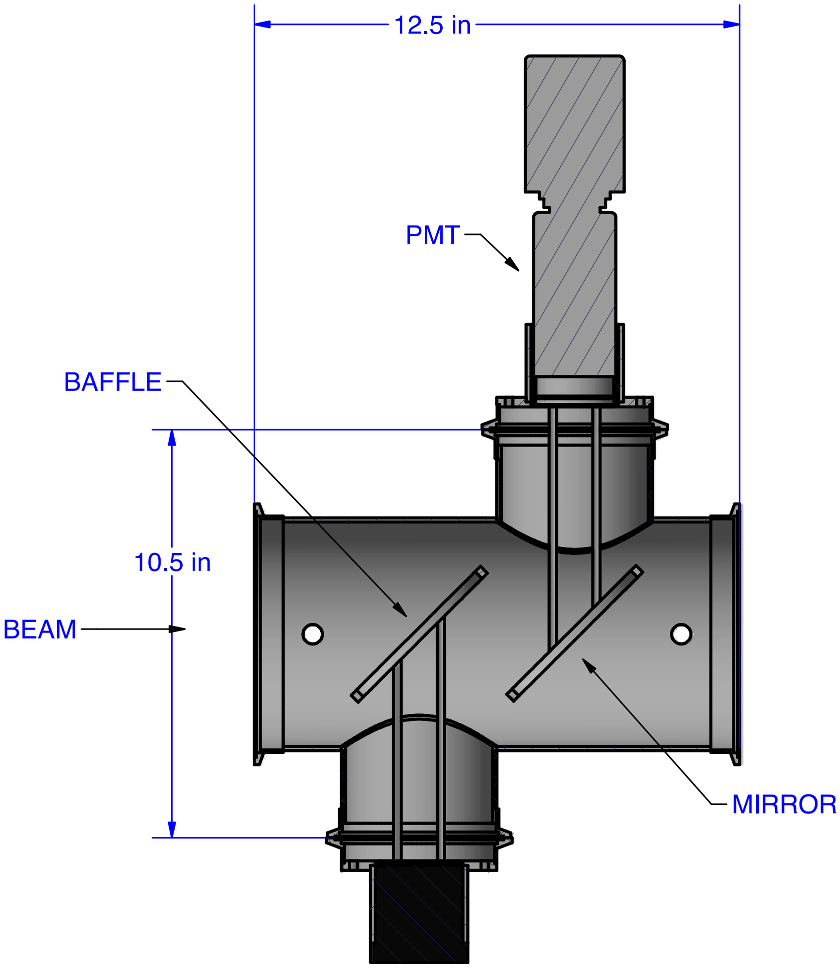

Figure 2.4: BIM Cerenkov counter

c) integrated beam intensity when DAQ is busy excluding the trigger inhibit buckets ($I_{DAQbusy}$).

d) intensity information of triggering RF bucket along with ± 16 RF buckets around it.

e) complete intensity information of each bucket during a spill.

The above measurements along with SEM measurement are used to calculate the live proton as

$$\text{live proton} = \frac{I_{G2SEM}}{I_{QIE}}(I_{QIE} - I_{inhibit} - I_{DAQbusy}), \tag{2.2}$$

where I_{G2SEM} is the intensity of the SEM counter. Linear response of BIM measurement has been verified using SEM2.5[31]

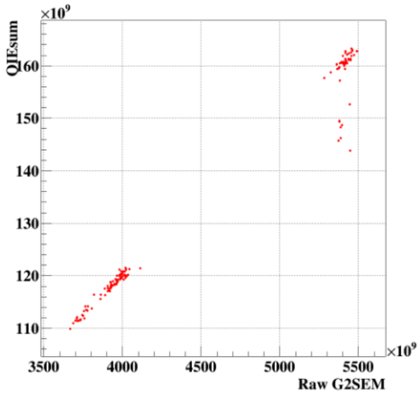

Figure 2.5: The phototube saturation can result in the QIE response being saturated with G2:SEM (SEM). The plot here shows the response of QIE as a function of SEM measurement for two runs (9338, 9339). The mirror in the BIM gets damaged over time due to radiation hence can also affect the QIE response with the phototube being saturated. Hence it is important for the two analyzed runs to be as close to each other in time as possible to avoid the effect of mirror damage.

2.2 Targets

The SeaQuest target system is placed downstream of the Beam Intensity Monitor and 129 cm upstream of the front face of the focusing magnet. There are two liquid targets, hydrogen and deuterium, which are contained in flasks. A third target is a vacuum filled flask of the same dimensions known as the empty flask. It is used for background subtraction for the liquid targets. There are three solid targets; namely Iron, Carbon and Tungsten. A fourth target, known as no-target, which is nothing but solid target holders and air. It is used for background subtraction for solid targets. Each solid target is divided into 3 discs of equal length, which are spatially separated along the beam direction to minimize variation in acceptance between the solid and liquid targets. The targets are mounted on a motorized up-down motion table. The target control system accurately lines up one target at a time in front of the beam and switches to the next target position in between spills. Table 2.1 shows the length, density, interaction length and spills/cycle of each target position. The spills/cycle is the number of spills during which the beam interacts with a particular target in one cycle.

Target	Position	Density(g/cm^3)	Length(cm)	# of Interaction length	Spills/cycle
LH2	1	0.071	50.8	0.069	10
Empty Flask	2	–	–	0.0016	2
LD2	3	0.163	50.8	0.120	5
No target	4	–	–	0	2
Iron	5	7.87	1.905	0.114	1
Carbon	6	1.80	3.322	0.0696	2
Tungsten	7	19.30	0.953	0.096	1

Table 2.1: SeaQuest target configuration

A typical cycle lasts for 23 spills before a reverse cycle for another 23 spills. The target rotation is necessary to reduce any systematic differences between targets that may arise due to any time-dependent changes in beam or spectrometer. A schematic layout of the target table is shown in figure 2.6.

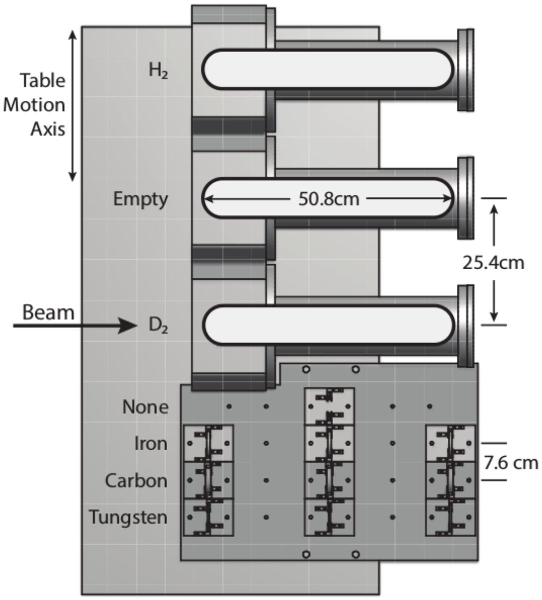

Figure 2.6: Target table layout

2.3 Magnets

SeaQuest uses two dipole magnets, namely, focusing magnet (FMAG) to focus high mass dimuon pairs into spectrometer acceptance and analyzing magnet (KMAG) to measure the momentum of muon tracks. The magnetic field of both magnets point in the same direction vertically i.e.; $\pm y$ direction, which bends muons horizontally along $\pm x$ direction, depending on the direction of magnetic field and charge associated with the muon track. Thus, X-Z plane is the bend plane and Y-Z plane is the non-bend plane.

A Perspective drawing of the FMAG is shown in figure 2.7. It consists of a stack of high purity solid iron blocks of dimension 43.2 cm(H) x 160 cm(W) x 503 cm(L) with embedded aluminium coils taken from the E866 SM3 magnet. The coil is excited to 2000 A which is able to generate an almost uniform magnetic field of 1.9 T within the iron block. This corresponds to a transverse p_T kick of 3.07 GeV. The magnetic field inside FMAG is modeled using a magnetostatic program. The magnetic field calibration is done by studying the reconstructed mass of the J/ψ (3097) resonance peak. FMAG serves three main purposes: focusing high mass muon pairs, a beam dump, and a hadron absorber. First, FMAG focuses high p_T or

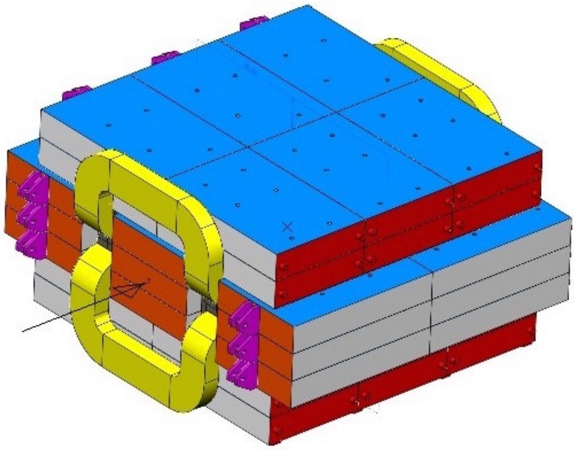

Figure 2.7: Schematic of focusing magnet

high mass dimuons into the spectrometer acceptance. High mass dimuons also correspond to high x_T, hence a good spectrometer acceptance of such events is valuable. Additionally, it also defocuses low momentum muon pairs, hence reducing the low momentum muon background. The solid iron block also serves as a beam dump. Only $\sim 10\%$ of the beam protons interact with targets. The remaining 90 % interacts within the FMAG, thus preventing the proton beam from going through the tracking stations. FMAG also absorbs hadrons produced via interaction of the beam with the target or beam dump itself.

A 25 cm deep and 5 cm in diameter hole is drilled at the centre on the front face of the FMAG. This increases the distance between the target cave and interaction point inside the dump, hence lowering the amount of radiation in the target area produced via dump interactions. This is important as the target cave needs to be frequently accessed for maintenance work. Additionally, it decreases the possibility of misidentifying dump events as target events to some extent.

The momentum analysing magnet, KMAG, is positioned further downstream, in between stations 1 and 2. It is used for analysing the momentum of muon tracks. It is 3 meters long with an open aperture as shown in Figure 2.1. The coils are excited to 1600 A which produces a magnetic field of 0.4 T corresponding to a transverse p_T kick of 0.41 GeV. The magnetic field distribution is measured using a hall probe and the calibration is determined using reconstructed mass of J/ψ (3097) resonance peak.

2.4 Tracking stations

The SeaQuest detector system comprises of 4 tracking stations. All four of them have hodoscopes, while only the first three of them have drift chambers and the fourth one has proportional tubes. The fast signals from the hodoscopes at each of these stations are used for triggering. The drift chambers provide good spatial resolution required for precise track reconstruction of muon tracks. The proportional tubes at station 4 is used for muon identification.

2.4.1 Hodoscopes

Hodoscope paddles are made of scintillating material with a photo-multiplier tube at their ends. When a charged particle passes through a scintillator paddle, photons are emitted. The scintillation light is converted to photo-electron and amplified by the photo-multiplier tube. This electric signal is recorded by the DAQ (Data Acquisition System). The hodoscopes being fast in response are used to make the trigger decisions. However, the hodoscope sizes are not fine enough to provide the spatial resolution required to estimate the kinematics of the charged particle. In addition to serving as input for trigger system, hodoscope hits are used for finding chamber hits which match the hit pattern of the hodoscope paddles. This helps to reduce the random hits on drift chamber and hence improve the efficiency of tracking software.

SeaQuest uses 4 hodoscopes, one at every station. Specifications of each hodoscope is given in table 2.2 At each station, arrays of paddles are arranged in 2 orientations. Vertical arrays of paddles measure the track position horizontally (along the x-direction) and are called the X-planes. Similarly horizontal arrays of paddles can measure the track position in the y-direction and called the Y-planes. There is a slight overlap of paddles ($\sim$ 0.32 cm) to avoid gaps in acceptance. Both X and Y measuring planes are further divided into two sets each. The X-planes can measure the x-position for tracks with $y > 0$ (denoted as Top or T) or with $y < 0$ (denoted as Bottom or B). Similarly, Y-planes can measure y-positions for tracks with $x > 0$ (denoted as Left or L) or with $x < 0$ (denoted as Right or R).

Name	# of Paddles	Paddle Width [cm]	Overlap [cm]	Width x Height [cm x cm]	z-Position [cm]
H1L	20	7.32	0.3175	78.74 x 140.117	654.03
H1R	20	7.32	0.3175	78.74 x 140.117	654.03
H1B	23	7.32	0.3175	162.008 x 69.85	667.118
H1T	23	7.32	0.3175	162.008 x 69.85	667.118
H2L	19	13	0.3175	132 x 241.285	1402.86
H2R	19	13	0.3175	132 x 241.285	1402.86
H2B	16	13	0.3175	203.238 x 152	1421.06
H2T	16	13	0.3175	203.238 x 152	1421.06
H3T	16	14.5875	0.3175	227.518 x 167.64	1958.51
H3B	16	14.5875	0.3175	227.518 x 167.64	1958.51
H4Y1L	16	23.4775	0.3175	152.4 x 365.797	2130.27
H4Y1R	16	23.4775	0.3175	152.4 x 365.797	2146.45
H4Y2L	16	23.4775	0.3175	152.4 x 365.797	2200.44
H4Y2R	16	23.4775	0.3175	152.4 x 365.797	2216.62
H4T	16	19.6475	0.3175	304.518 x 182.88	2235.5
H4B	16	19.6475	0.3175	304.518 x 182.88	2250.68

Table 2.2: Hodoscope specifications during Run 2

Name	z-Position [cm]
H1L	653.923
H1R	653.923
H1B	666.681
H1T	666.681
H2L	1404.93
H2R	1404.93
H2B	1421.11
H2T	1421.11
H3T	1958.62
H3B	1958.62
H4Y1L	2130.27
H4Y1R	2146.45
H4Y2L	2200.44
H4Y2R	2216.62
H4T	2234.91
H4B	2251.09

Table 2.3: Hodoscope positions during Run 3

2.4.2 Drift chambers

A drift chamber measures the drift time of electrons created inside the chamber due to ionization of the gas mixture when a charged particle passes through it. This allows precise measurements of the positions of charged particles. SeaQuest uses drift chambers in the first three tracking stations to accurately determine the x and y coordinates of muons passing through it. Table 2.4 lists the specifications of the wire chambers used in SeaQuest. Stations 1 and 2 have one chamber each and are referred as D1 and D2. Station 3 has two chambers, D3p and D3m, where p and m stands for ± y-direction. Each chamber has six wire planes categorized into 3 different views with two planes each. The x and x' are oriented along the y-direction, u and u' are tilted 14° , and v and v' are tilted -14°. The 'primed' planes are shifted horizontally by a distance of half a cell-width (distance between two wires) relative to the 'unprimed' planes. This configuration helps resolve the left-right ambiguity, which is essential to differentiate which side of the sense wire did the muon track passed through.

The signals from the sense wires are fed to ASDQ (Amplification, Shaper, Discriminator and Charge integrator) cards which are used for amplification and discrimination. The processed signal is sent to the LSB (Level Shifter Board), which converts it to standard LVDS (low voltage differential signal). These LVDS outputs are transmitted to the TDC module for digitization and readout by DAQ. Specifications of each chamber are listed in table 2.4. D1 and D3m were upgraded for later datasets and are listed as a version number after decimal. The upgrade was done to increase the acceptance in kinematic variable $x2$ which is important for the SeaQuest measurements. The dates when these upgrades were installed are given in table

2.5. D1.1 was originally used in the E866/NuSea experiment, while D2 and D3m.1 were built for E605. In order to use them for SeaQuest, significant work was required to bring them back to working condition. D1.2, D3m.2 and D3p were built from scratch for SeaQuest.

The gas mixture used for all chambers except D1.2 is Argon : Methane : CF4 (88% : 8% : 4%). This gas mixture give an electron drift velocity of $20\mu m/ns$. D1.2 used 'fast' gas mixture Argon : CF4 : Isobutane : Methylal (68% : 16% : 13% : 3%). The drift velocity for this chamber is $50\mu m/ns$. Higher drift velocity at station 1 is useful for better chamber performance due to high rate at station 1.

The resolution of the dimuon invariant mass spectrum is dominated by multiple scattering in FMAG. To keep the contribution of position resolution to the overall resolution at less than 10%, the spatial resolution of chamber planes is required to be better than $400\mu m$ which corresponds to a momentum resolution $\Delta p/p = 0.03.p(GeV/c)$

Chamber	Plane	# of wires	Cell width [cm]	Width x Height [cm x cm]	z-Position [cm]
D1.1	X	160	0.64	102 x 122	617
	U,V	201	0.64	101 x 122	±20
D1.2	X	320	0.50	153 x 137	617
	U,V	380	0.50	153 X 137	±1.2
D2	X	112	2.1	233 x 264	1347
	U,V	128	2.0	233 x 264	±25
D3p	X	116	2.0	232 x 166	1931
	U,V	134	2.0	268 x 166	±6
D3m.1	X	176	1.0	179 x 168	1879
	U,V	208	1.0	171 x 163	±19
D3m.2	X	116	2.0	232 x 166	1895
	U,V	134	2.0	238 x 166	±6

Table 2.4: Drift chambers specifications. The z-positions of the U, V planes are relative to the corresponding X plane.

Run	Dates	St1	St2	St3
1	2012 Mar. - 2012 Apr.	D1.1	D2	D3p&D3m.1
2	2013 Nov. - 2014 Aug.	D1.1	D2	D3p&D3m.2
3	2014 Nov. - 2015 Jul.	D1.1	D2	D3p&D3m.2
4	2015 Nov. - 2016 Mar.	D1.2	D2	D3p&D3m.2
5	2016 Mar. - 2016 Jul.	D1.1&D1.2	D2	D3p&D3m.2
5	2016 Nov. - 2017 Jul.	D1.1&D1.2	D2	D3p&D3m.2

Table 2.5: Drift chamber combination during various data-taking periods.

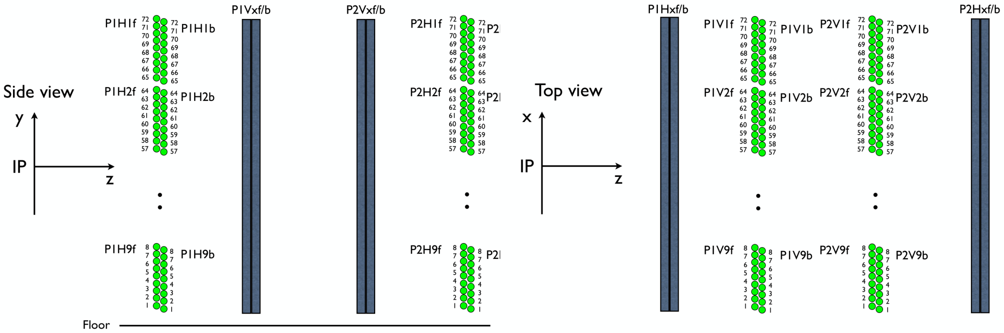

Figure 2.8: YZ (left) and XZ (right) view of the prop tube

2.4.3 Proportional tubes

Proportional tubes are used in Station 4 for muon identification. There is a 1 m thick iron wall in between station 3 and station 4 which absorbs any hadron before it reaches station 4. For precise track reconstruction, there are 4 planes of proportional tubes; first and fourth plane being horizontal and second and third being vertical. Just like hododscopes, the horizontal arrangement measures the y position and vertical arrangement measure the x position. Each plane consists of 9 modules with 16 prop tubes each. Each of these sets is further divided into two staggered sets, with the second layer behind the first one shifted by half a tube width, to solve the left-right ambiguity as in the case of the wire chambers. A schematic of the proptube is shown in figure 2.8. Each tube is made of aluminium tube of 2 in diameter with 1/16 in thick wall. The sense wire at the centre of the tube is a gold-plated $20\mu m$ platinum wire, typically set at 1800 V. Table 2.6 shows the specifications of each plane. The gas used in the proportional tubes is the same Argon : Methane : CF4(88% : 8% : 4%) mixture used for most of the chambers. The maximum drift time is 650 ns, which gives a hit-rate tolerance of up to 2 MHz for a single wire, while the hit rate is in general lower than 1 MHz per wire. The position resolution was found to be $500\mu m$, which suffices for the purpose of muon identification.

Plane Name	# of Tubes	Tube Width [cm]	Width x Height [cm x cm]	z-Position [cm]
P1H	144	5.08	368.3 x 368.3	2100.7
P1V	144	5.08	368.3 x 368.3	2176.6
P2V	144	5.08	368.3 x 368.3	2369.1
P2H	144	5.08	368.3 x 368.3	2392.2

Table 2.6: Proportional tube specifications

2.5 Trigger

The SeaQuest trigger system is optimized for selecting high mass (4-10 GeV) dimuon events and suppressing low mass events arising from charmonium and meson decays and other sources of background from target or beam dump. The trigger system is designed as such, to minimize DAQ deadtime, and hence, maximize trigger rate on high mass dimuon candidates. Two kinds of trigger systems are used in SeaQuest, namely NIM-based and FPGA-based. The signals from hodoscopes are used as input to the triggering system. The time resolution of hodoscopes (determined by the length of the hodoscopes) are of the order of nanoseconds and therefore is well suited for triggering on RF buckets which are separated by approximately 18.9 ns.
The NIM trigger utilizes Nuclear Instrumentation Module for trigger information. During nominal data taking, two types of NIM trigger are active, known as NIM-1 and NIM-3. The NIM-1 trigger is a coincidence of y-measuring hodoscope hits from all 4 stations. This trigger is used for studying the efficiency of the x-measuring hodoscopes. The second NIM trigger, NIM-3 is also known as the random trigger. It triggers on the coincidence of two clocks, 7.5 kHz pulses generated by a gate generator and a 53.1 MHz RF clock. NIM-3 trigger samples the intensity profile of beam, which is utilized for various rate dependence studies. The hits from random trigger are superimposed on top of true Drell Yan signal hits in the Monte Carlo. Such samples of Monte Carlo (known as messy MC) are used to study the dependence of tracker efficiency on the instantaneous beam intensity. This is explained in more detail in the next chapter on Monte Carlo simulation.

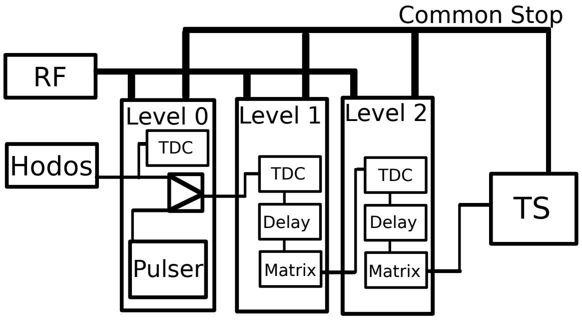

Figure 2.9: Schematic of SeaQuest Trigger

The FPGA trigger system uses 9 CAEN v1495 VME modules, Altera EP1C20F400C6 FPGA (Field Programmable Gate Array), and a “Trigger Supervisor” VME module. A schematic layout of the FPGA based trigger system is shown in figure 2.9. There are 3 levels of v1495 modules from level 0 to level 2. Level 0 and level 1 each has four v1495 modules for measuring the top and bottom halves of both x and y measuring planes. The level 0 operates in two modes, known as pulser mode and production mode. In pulser mode Level 0 output produces random hit patterns. This mode is used to study the response of Level

1 and Level 2 modules. In production mode, the level 0 just transmits the output from the hodoscopes to level 1. The level 1 or the 'track finder' is responsible for finding valid muon tracks from hodoscope hits at each stations in each of the four quadrants. It selects possible tracks by matching the hodoscope hit patterns with a preselected list of hit patterns known as trigger roads. The trigger road combination is generated by examining the path of single muons and dimuons from Monte Carlo simulations. A list of roads (known as roadset) are selected to maximize the signal event rate. The roads which were found to be highly populated by hits from background events (known as hot roads) are removed from the roadset.

Once the trigger roads are identified, level 1 outputs the road information, charge and transverse kick of the tracks to level 2. The level 2 has a single v1495 module and acts as 'track correlator'. At this stage the tracks are combined in all possible pairs and the combinations are matched with the preselected combination of roads for dimuon trigger. A list of possible triggers are given in table 2.7. If any of the listed triggers are satisfied, a signal is sent to Trigger Supervisor which then signals the DAQ to record the event.

Trigger	Half	Charge	$p_T(GeV)$	Notes
FPGA 1	TB/BT	+-/-+	N/A	Dimuon trigger for physics run
FPGA 2	TT/BB	+-/-+	N/A	Not used, too many background events
FPGA 3	TB/BT	++/ - -	N/A	Same sign trigger for estimating combinatoric backgroud
FPGA 4	T/B	+/ -	N/A	Single muon trigger
FPGA 5	T/B	+/ -	$> 3GeV$	High p_T single muon trigger

Table 2.7: Level 2 FPGA trigger logic conditions. In the 'Half' column, T stands for a track in the top half and B stands for a track in the bottom half.

2.6 Data Acquisition, Decoding and Storage

The SeaQuest Data acquisition system is divided into four subsystems, namely, Main DAQ, Scaler DAQ, Beam DAQ and Slow Controls. Main DAQ records spectrometer hits and trigger timing information. Beam DAQ reads out beam information from QIE. Scaler DAQ records scaler information from beam, triggers and detectors used for real time monitoring and diagnosis. Slow Controls record various spill level information like the target position and magnet current.

2.6.1 Main DAQ

The Main DAQ uses VME-based CODA software developed at Jefferson Lab (CEBAF On-line Data Acquisition). Main DAQ consists of multiple VME crates at its front end which receives signal from trigger supervisor. Depending on the spectrometer configurations, the number of VME crates can vary. SeaQuest typically employs 14 VME crates and one crate for trigger supervisor (TS). Each VME crate consists of a single board processor called ROC (Read out controller), a TI (Trigger interface) and several TDCs. The trigger supervisor coordinates with each VME crate through its trigger interface. The trigger supervisor can receive upto 12 trigger inputs. Five of the input channels record FPGA triggers, four of them are for NIM triggers and the last three for BOS, EOS and flush events. Once the TS receives a trigger, it is set to 'busy'. TS interacts with each VME crate through TI to stop the TDCs and to process the collected data. The TS also talks to the BIM before accepting the trigger. If the BIM detects the triggering bucket or neighbouring ±8 RF bucket intensity to be larger than the inhibit value then the trigger is not accepted. In case the beam is not inhibited, the TDCs are read out in series by ROC which is sent to CODA via private network. Once the readout is complete, TI sends a signal to TS. After receiving readout completion signal from each TI, TS is reset and ready to accept next trigger.

The time from acceptance of trigger to readout completion is approximately $150\mu s$. Each TDC takes $10\mu s$ to stop once 'accept trigger' signal is received. Additionally each TDC requires a $32\mu s$ copy-in-progess time even if there are no stored hits. Although all the VME crates are processed and read out parallelly, TDCs in each crate are readout in series by the ROC. This means that the slowest VME crate determines the deadtime during read out.

2.6.2 Scaler DAQ

The Scaler DAQ records beam, trigger and hodoscope data useful for diagnosis during data taking. Scaler DAQ runs independently of Main DAQ and is controlled by a separate CODA software. It has a single VME crate with one processor board and four scaler cards installed. One of the VME scaler card is triggered by coincidence of a 7.5KHz gate generator and a beam spill gate. This records 7.5KHz response of two unrelated hodoscope and can be used to calculate duty factor of the beam. The other 3 VME scalers are triggered by BOS and EOS signals and therefore records integrated counts over a spill. The collected data include number of times each trigger is recorded by Main DAQ, intensity of beam and hodoscope rates. The Scaler DAQ data are processed real time and displayed on the monitor in the SeaQuest Control room.

2.6.3 Beam DAQ

The Beam DAQ records data from cerenkov detector. It has RF bucket resolution and reads 53.1 MHz structure of the beam. It measures duty factor of the beam as $DF = <I>^2 / <I^2>$. Duty factor provides a measure of the beam quality and is required by the accelerator divison for tuning the beam. Apart from measuring the duty factor, Beam DAQ also records the following data: a) Intensity of each bucket b) buckets which have instantaneous intensity higher than inhibit threshold c) buckets during which the trigger was busy due to DAQ dead time (excludes the buckets in b). This allows for calculation of live protons on target during each spill. The Beam DAQ reads data after receiving the EOS signal. In order to read large volume of data (300 MB) in between spills (55s), the DAQ program utilizes multithreading. Three threads are used to read data from BIM's three ethernet chips. Additionally, eight threads are used to analyse the data realtime, so that it can be displayed on the monitor in the control room. Realtime analysis of the Beam DAQ data is useful for monitoring and diagnostic purposes during data taking.

2.6.4 Slow Controls

Slow Controls refer to several different programs or scripts to synchronize DAQ data stream, to monitor various systems during data taking, and to record process variables which have a frequency of a spill or larger. These scripts utilize EPICS (Experimental Physics and Industrial Control System) software to communicate process variables with other systems across servers.

Each DAQ system writes its respective output on separate files and the decoder must know the spill ID (which is a unique number to identify each spill) to which each data corresponds to, in order to synchronize the data collected by each DAQ. Each DAQ is assigned a spill ID. A master spill ID is stored in a text which is incremented at each EOS signal. It is then inserted into the CODA file of both Main DAQ and Scaler DAQ. The master spill ID is also written on the easily accessible but volatile memory of EPICS server. Scripts that perform realtime analysis, read the spill ID from EPICS server and attach it to their output.

The data from Slow Control system is collected after the EOS signal has been received. It includes beam parameters such as quality and intensity of beam, configuration of accelerator and status of magnets. These data are read via Fermilab accelerator control network (ACNET). Additionally, the target in the path of beam, target rotation and temperature and pressure of the cryogenic system are also recorded. A multi-channel digital meter is used to record the environmental conditions such as temperature, humidity and pressure inside the experimental hall. Slow control system also alerts the shifters about low disk space, or if any of the DAQ has stopped working. It is critical in monitoring the status of the experiment and helpful in smooth collection of good quality data.

2.6.5 Decoder

Typically, one run of physics data taking is about an hour long. The approximate size of the raw data file collected is ~ 1 GB. The raw data is in hexadecimal format. The raw CODA file from Main DAQ along with corresponding information from other DAQ systems is stored on the SeaQuest servers and backed up on tape storage provide by FermiLab computing division. The Main DAQ raw file contains TDC information from hodoscopes, drift chambers and proportional tubes of each triggered event. Bucket by bucket intensity information from the Beam DAQ is also attached to the MainDAQ CODA file.

These raw data files are processed by a custom C++ software known as 'decoder'. The decoder converts the data from its original format, calculates additional information and fills the MySQL database with the decoded data. Data from each run is stored in separate MySQL schema.

The Decoder also runs in sampling mode during data taking and quickly decodes the sampled raw data which is displayed on SeaScape, a web based tool to access the collected data in real time. This important feature of decoder provides easy access to the data being collected and facilitates monitoring of the experiment during data taking.

Chapter 3

GEANT Monte Carlo

SeaQuest utilizes two Monte Carlo programs to simulate the performance of the spectrometer, namely, FastMC and GMC. FastMC is a fortran-based simulation code inherited from E866 and modified according to SeaQuest's experimental configurations. The algorithm from FastMC was adopted for another simulation code for SeaQuest, which is based on GEANT to perform more detailed simulations. I have been responsible for running, maintaining and updating the GMC simulations for the collaboration. This chapter describes the GMC program and the improvements made to it during the time period I was responsible for it. As the name suggests GMC is based on the GEANT4 package which is a toolkit to simulate passage of particles through matter. The GMC follows the following architectural setup [32].

- Set the physics processes list. For SeaQuest, the physics list was set to $FTFP\_BERT\_EMX$.
- Initialize the construction of spectrometer with the help of geometry files. These geometry files include information about the size, orientation, material of detector components, magnetic field information etc. These files are produced and updated based on the survey results (details in Section 3.3).
- For GEANT to start simulation of an event, it needs a particle to begin with. Specifically, it needs a particleID, its position and momentum along with the geometry description of the spectrometer. Based on the GMC settings specified at runtime, it will use one of the two generators, namely, gun(background) or dimuon generator, to generate primary particles (to be discussed in the section 3.1 and 3.2).
- Initialize a run. A run is defined as a collection of events. Within a run, the settings such as generator, physics process etc. cannot be changed. This step ends after the number of specified events are processed. It is represented by G4Run class.
- Each event in a run is processed by generating primary particle and all the subsequent secondary and tertiary particles. It is represented by G4Event class.
- A step in GEANT is defined by particle's point of start and end. It contains information such as energy loss in that step. After each step the track information is updated. It is represented by G4Step class.

- A track is defined in GEANT as a snapshot of the particle's status after a step has been completed. A track is deleted or killed if certain criteria are not satisfied, e.g., for SeaQuest it is deleted if the particle's energy is less than 1 GeV, or has a negative z momentum, or could not make it past z=350 cm. It is represented by G4Track class.

3.1 Gun generator

Gun generator starts with 120 GeV proton incident at the target along the beam-axis. The incident proton interacts with the target or dump (as specified in the settings) to create pions and kaons, which further decay into muons and electrons. It is a tool to understand the background tracks and its properties. Unfortunately, it is not very efficient at generating a large background sample, as only a small fraction of background tracks make it all the way through the detectors. A sample of 40 million protons was generated in a period of 1 week of running. The tracking software was able to find ~ 200 tracks in this sample out of which only ~ 30 survived the target selection cuts. SeaQuest, being a high beam intensity experiment receives $\sim 2e12$ protons every second. Even producing a sample equivalent to 1 second of beam would take thousands of weeks. Hence, it is not feasible to use gun Monte Carlo to generate adequate background sample. However, the generated samples are useful for exploring the regions in our detectors which are more prone to background tracks by studying the hit distribution due to these tracks on the detectors. For example, a comparison of the shape of the hit distribution from gun MC simulation and random trigger (NIM3) data shows a good agreement (Figure 3.1). This supports the usage of NIM3 trigger data for investigating accidental dimuon background.

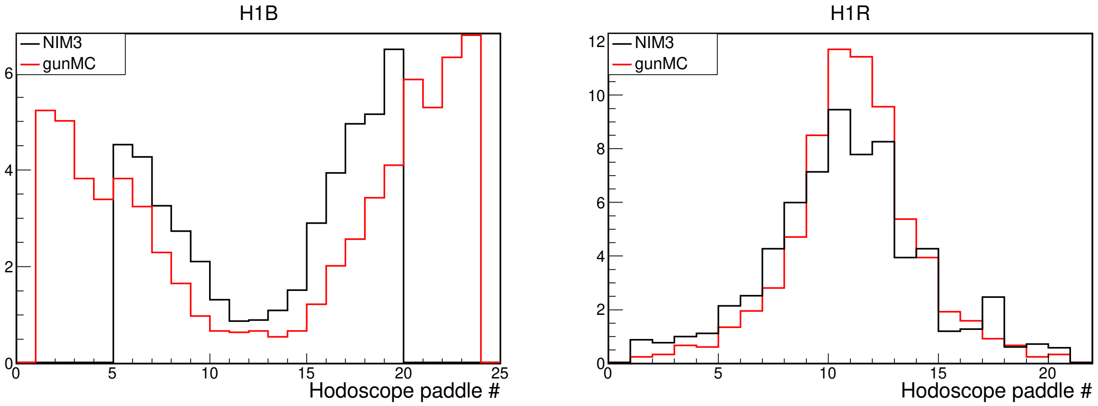

Figure 3.1: H1B (left) and H1R (right) hit distribution comparison between NIM3 data (blue) and gunMC data (red). The x-axis is the hodoscope paddle number. H1B (x-measuring) has 23 paddles, of which 4 paddles were turned off on each side during data taking. H1R (y-measuring) has 20 paddles.

Gun MC samples are also useful in studying the characteristics of the background tracks as well as the effectiveness of the analysis cuts in removing contamination coming from dump and upstream events. Figure 3.2 shows the distribution of types of particles that hit each hodoscope. This study was done using 32 million gun monte carlo sample (which is approximately equivalent to 1300 RF buckets assuming 25000 protons per bucket). Under the mentioned assumption, one can qualitatively estimate that there are about 3 background ($\sim$ 4000/1300) muon tracks per RF bucket that hit Station 1. One can also look at the locations from which these particles originate. Figure 3.3 shows the z distribution of the origin of muon and electron tracks. One can immediately notice that there are more μ^+ than μ^-, which is reasonable given the proton beam is positively charged. There are muons produced upstream of target which can be explained by the decay of πs and Ks produced from the interaction of proton beam with the instrumentation package. The total interaction in the upstream instrumentation is approximately $\sim 0.985\%$ [33]. The plot also shows muons being produced in between target and dump indicating the presence of decay-in-flight pions or kaons which are produced inside the target region. The generated gun MC sample was tracked using the same requirements applied to real data. Approximately 200 tracks were found from a sample generated using 40

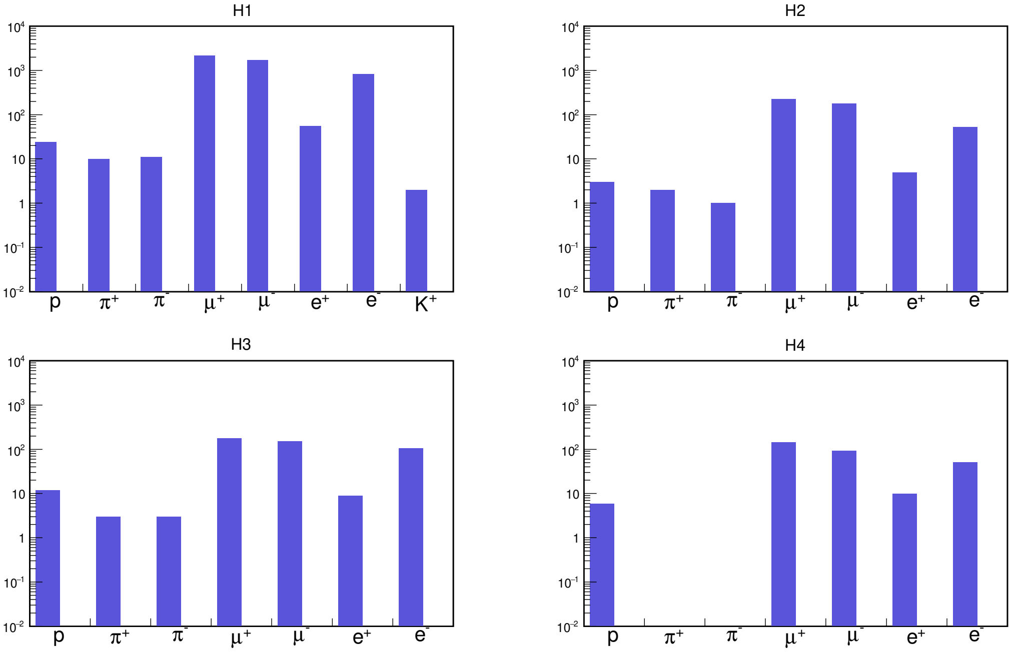

Figure 3.2: Histogram depicting different types of 'particle' that hit hodoscopes at all four stations. This plot was generated using 32 million gun MC events. The Monte Carlo uses $FTFP\_BERT\_EMX$ physics process list and outputs the creation process for each of the generated particle. Pions and Kaons are created in 'ProtonInelastic' process. The muons are created from 'Decay' process of Kaons and Pions. The electrons are created from conversion of photon to e^-e^+ pair ('conv') and bremstrahlung radiation from muons ('bremstrahlung'). e^- is also created by ionization process when a muon passes through gas chambers ('muIoni')

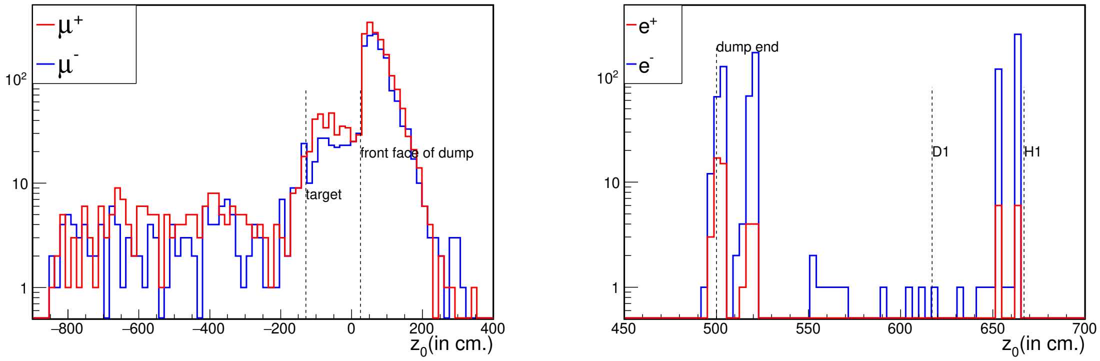

Figure 3.3: z-position (z_0) of the origin of muon and electron tracks that hit hodoscope 1. The dashed vertical lines in the left plot shows the location of the centre of the target and front face of the beam dump. In the right hand plot the vertical dashed lines are drawn to show the end of the dump, the location of station 1 hodoscope and drift chamber.

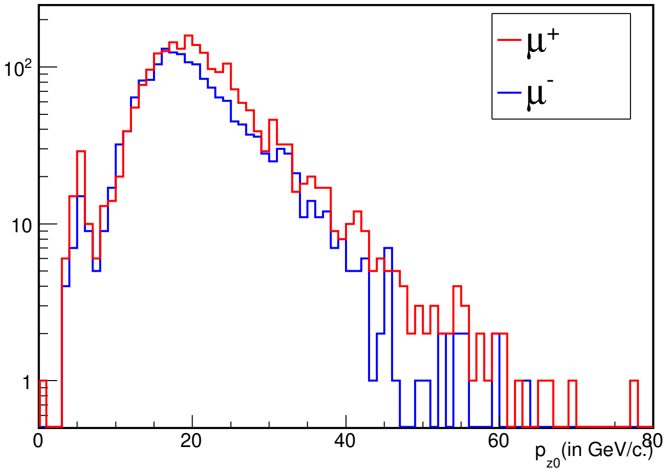

Figure 3.4: Initial z momentum of the muon tracks.

million protons. The target selection cuts were applied on the tracked data. Studies show that the cuts are effective in removing background tracks generated inside beam-dump (Figure 3.5). However, there are still some muon tracks coming from decay-in-flight pions that survive the cuts.

3.2 Dimuon event generator

There are three types of dimuon generator: Drell-Yan, J/ψ and ψ'.

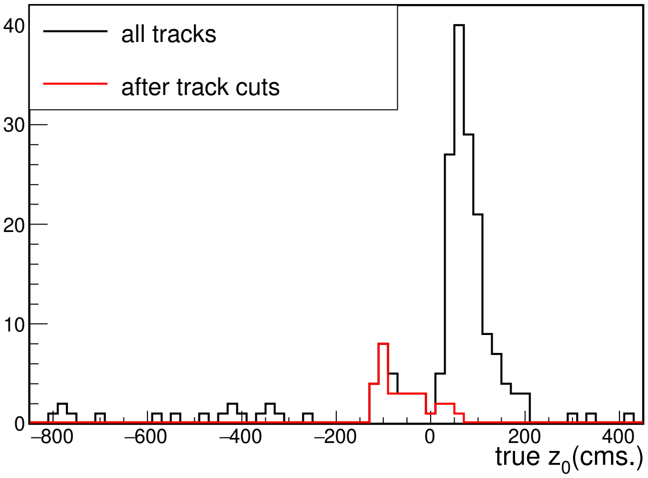

Figure 3.5: Origin(z0) of background tracks before and after target selection cuts

3.2.1 Drell-Yan event generator

Input distributions

The Drell-Yan dimuon generator generates two unlike sign muons with Drell-Yan kinematics. It samples dimuon mass (M) from a flat distribution ranging from 2 GeV to 10 GeV. Similarly, the Feynman-x (x_F) is also picked from a flat distribution in the range -0.95 to 0.95. The M and x_F of the dimuon are sampled from a uniform distribution to ensure equal statistics for the entire M and x_F range. Dimuon p_T distribution is sampled from the Kaplan functional form [34] given in equation 3.1.

$$f(p_T) = \frac{p_T}{(1 + (p_T/p_1)^2)^6}, \tag{3.1}$$

where parameter p_1 is a measure of the broadness of the p_T distribution. It is related to the mean of the p_T distribution as shown in the following equation,

$$< p_T >= \frac{35\pi p_1}{256}, \qquad < p_T^2 >= \frac{p_1^2}{4} \tag{3.2}$$

The default value of p_1 used in MC was 2.8 GeV/c. This value was inherited from the previous Drell-Yan experiment at Fermilab, known as E866/NuSea. E866 used 800 GeV proton beam which corresponds to $\sqrt{s}$ = 38.8 GeV [35]. However, the $\sqrt{s}$ for E906/SeaQuest is 15.01 GeV. Data from previous Drell-Yan experiments show that mean p_T of the dimuon increases with increasing $\sqrt{s}$ for a given $\sqrt{\tau}$ [24]. Hence, mean p_T for E906 should be smaller than E866. Additionally, early data from pion induced Drell-Yan show a clear dependence of $< p_T >$ on x_F of the dimuon[36]. Based on the above observations, the parameter p_1 was adjusted using the 'reweighting method' until the p_T distribution from GMC agree with the SeaQuest data. The Drell-Yan angular kinematics is considered in dimuon rest frame (Collins-Soper frame [37]). The polar angle of μ^- in the Collins-Soper frame follows a $1 + cos^2\theta$ distribution with a uniform azimuthal angular distribution in ϕ. Therefore, the angular kinematic variables, θ is chosen from $1 + cos^2\theta$ distribution and ϕ from flat distribution ranging from 0 to 2π.

Transformation from Collins-Soper frame to Laboratory frame

Due to the consideration of dimuon in Collins-Soper frame, the transformation of the kinematics to lab frame requires three lorentz transformations: one along the virtual photon's $-p_T$ direction to an intermediate frame (here, dimuon z-momentum is 0), second transformation is along negative z-direction from the intermediate frame to hadron-hadron centre of mass(CM) frame and final transformation is also along negative z-direction from hadron CM frame to lab frame.[38]

In Collins-Soper frame (Figure 3.6), the z-axis is chosen along the bisector of $\vec{P_1}$ and $-\vec{P_2}$, where $\vec{P_1}$ and $\vec{P_2}$ are the beam and target hadron vector momenta, respectively. The plane formed by $\vec{P_1}$ and $\vec{P_2}$ is called hadron plane and it makes an angle ϕ with the lepton plane.

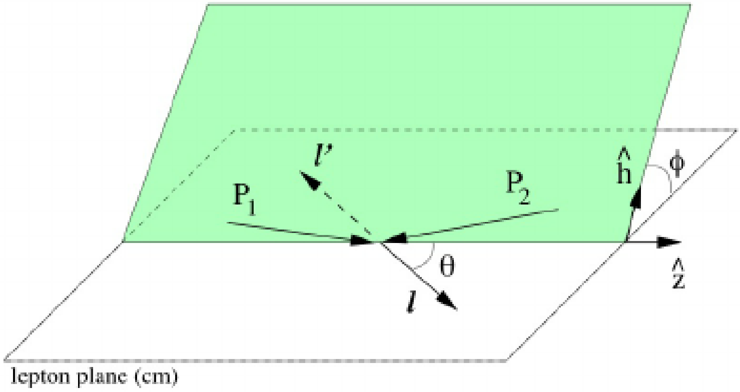

Figure 3.6: Illustration of angles θ and ϕ in Collins-Soper frame. Figure taken from [2]

The direction of x-axis in case of Collins-Soper frame is along the virtual photon p_T direction which makes this frame very useful. The energy-momentum vector for the muons in this frame is written as

$$p_{\mu^+} = (E_{\mu^+}, (p_{\mu^+})_x, (p_{\mu^+})_y, (p_{\mu^+})_z) \equiv (M/2, p_{\mu^+} sin\theta cos\phi, p_{\mu^+} sin\theta sin\phi, p_{\mu^+} cos\theta) \quad (3.3)$$

$$p_{\mu^-} = (E_{\mu^-}, (p_{\mu^-})_x, (p_{\mu^-})_y, (p_{\mu^-})_z) \equiv (M/2, -p_{\mu^+} sin\theta cos\phi, -p_{\mu^+} sin\theta sin\phi, -p_{\mu^+} cos\theta) \quad (3.4)$$

Lorentz transformation is applied to boost from CS frame along $-p_T$ direction, which is essentially the x axis in this frame. The γ_{CS} and β_{CS} for the boost are given as

$$\gamma_{CS} = \frac{\sqrt{p_T^2 + M^2}}{M} \tag{3.5}$$

$$\beta_{CS} = \frac{p_T}{\sqrt{p_T^2 + M^2}} \tag{3.6}$$

The resulting momentum vector in the intermediate frame (denoted by ') are given by

$$p'_{\mu^+} = (E'_{\mu^+}, (p'_{\mu^+})_x, (p'_{\mu^+})_y, (p'_{\mu^+})_z) \tag{3.7}$$

$$\equiv (\gamma_{CS}(E_{\mu^+} + \beta_{CS}(p_{\mu^+})_x), \gamma_{CS}((p_{\mu^+})_x + \beta_{CS}E_{\mu^+}), p_{\mu^+} sin\theta sin\phi, p_{\mu^+} cos\theta) \tag{3.8}$$

$$p'_{\mu^-} = (E'_{\mu^-}, (p'_{\mu^-})_x, (p'_{\mu^-})_y, (p'_{\mu^-})_z) \tag{3.9}$$

$$\equiv (\gamma_{CS}(E_{\mu^+} - \beta_{CS}(p_{\mu^+})_x), \gamma_{CS}(-(p_{\mu^+})_x + \beta_{CS}E_{\mu^+}), -p_{\mu^+} sin\theta sin\phi, -p_{\mu^+} cos\theta) \tag{3.10}$$

Before boosting to hadron-hadron CM frame along z-direction the x-y axis is rotated (ϕ_γ) to match the x-y axis in lab frame.

$$(p'_{\mu^+})_x|_{rotated} = cos\phi_\gamma (p'_{\mu^+})_x - sin\phi_\gamma (p'_{\mu^+})_y \tag{3.11}$$

$$(p'_{\mu^+})_y|_{rotated} = cos\phi_\gamma (p'_{\mu^+})_y + sin\phi_\gamma (p'_{\mu^+})_x \tag{3.12}$$

$$(p'_{\mu^-})_x|_{rotated} = cos\phi_\gamma (p'_{\mu^-})_x + sin\phi_\gamma (p'_{\mu^-})_y \tag{3.13}$$

$$(p'_{\mu^-})_y|_{rotated} = -cos\phi_\gamma (p'_{\mu^-})_y + sin\phi_\gamma (p'_{\mu^-})_x \tag{3.14}$$

Next the lorentz transformation is performed along z-axis to obtain the energy-momentum 4-vector in hadron CM frame using,

$$\gamma_{CM} = \frac{\sqrt{p_L^2 + M^2}}{\sqrt{M^2}} \tag{3.15}$$

$$\beta_{CM} = \frac{p_L}{\sqrt{p_L^2 + M^2}}, \tag{3.16}$$

where p_L is defined as

$$p_L = \frac{x_F\sqrt{s}}{2}(1 - \frac{M^2}{s}) \tag{3.17}$$

The x and y component of the momentum remains unchanged. The energy and z-momentum transform as,

$$(p_{\mu^+})_z|_{CM} = \gamma_{CM}((p'_{\mu^+})_z + \beta_{CM} E'_{\mu^+}) \tag{3.18}$$

$$E_{\mu^+}|_{CM} = \gamma_{CM}(E'_{\mu^+} + \beta_{CM}(p'_{\mu^+})_z) \tag{3.19}$$

Similarly, the final transformation to lab frame is performed using

$$\gamma_{lab} = \frac{E_{beam} + m_{proton}}{\sqrt{s}} \tag{3.20}$$

$$\beta_{lab} = \frac{p_{beam}}{E_{beam} + m_{proton}} \tag{3.21}$$

as,

$$(p_{\mu^+})_z|_{lab} = \gamma_{lab}((p_{\mu^+})_z|_{CM} + \beta_{lab} E_{\mu^+}|_{CM}) \tag{3.22}$$

$$E_{\mu^+}|_{lab} = \gamma_{lab}(E_{\mu^+}|_{CM} + \beta_{lab}(p_{\mu^+})_z|_{CM}) \tag{3.23}$$

Cross section weighted calculation

Each event is assigned a weight based on its cross-section which is proportional to the probability of that event happening. Based on the kinematics of the sampled dimuon, beam and target fractional momentum x_B(or x_1) and x_T(or x_2) are obtained using the following definition [39]

$$x_1 = \frac{P_2.Q}{P_2.P}, \qquad x_2 = \frac{P_1.Q}{P_1.P} \tag{3.24}$$

where, P_1 and P_2 are beam and target 4-momentum vector, P is the total momentum defined as $P = P_1 + P_2$ and Q is the 4-momentum of the lepton pair. The Monte Carlo computes Leading-order (LO) Drell-Yan cross section as,

$$\frac{d^2\sigma_{LO}}{dM dx_F} = \frac{8\pi\alpha^2}{9M^3}\frac{x_1 x_2}{x_2 + x_2}\left[\frac{4}{9}\left[u(x_1)\left(\frac{Z}{A}\bar{u}(x_2) + \frac{N}{A}\bar{d}(x_2)\right) + \bar{u}(x_1)\left(\frac{Z}{A}u(x_2) + \frac{N}{A}d(x_2)\right) + 2c(x_1)c(x_2)\right] + \right.$$
$$\left.\frac{1}{9}\left[d(x_1)\left(\frac{Z}{A}\bar{d}(x_2) + \frac{N}{A}\bar{u}(x_2)\right) + \bar{d}(x_1)\left(\frac{Z}{A}d(x_2) + \frac{N}{A}u(x_2)\right) + 2s(x_1)s(x_2)\right]\right] \tag{3.25}$$

where Z/A and N/A are fractions of protons and neutrons, respectively, in the target nucleus.

To get the next-to-leading-order (NLO) cross section for each dimuon, the LO cross section is multiplied by the K-factor based on its x_1 and x_2(described next).

$$\frac{d^2\sigma_{NLO}}{dMdx_F} = Kfactor(x_1, x_2)\frac{d^2\sigma_{LO}}{dMdx_F} \tag{3.26}$$

K-factor and NLO calculation

It has been known that LO calculation is inadequate in describing the data. Hence, Next-to-Leading-Order (NLO) cross section calculation is required to take into account QCD effects at order α_s. To obtain NLO result, each dimuon is assigned a factor, known as K-factor. The K-factor is defined as the ratio of cross section at NLO to cross section at LO. The K-factor values used in the code initially were based on E866. SeaQuest being a completely new experiment with different beam energy, required the K-factor calculations to be revised. The earlier K factor was not only 1-dimensional (dependent on dimuon mass), but also had incorrect shape for our case. A thorough study using NLO code from INFN group [40, 41, 42], to calculate a 2-dimensional K-factor (dependent on x_1, x_2 or M, x_F)[43]. Based on this study the MC was updated to utilize a 2-dimensional K-factor as a function x_1 and x_2 by Bryan Kerns. This study also improved the agreement between data and MC. The K-factor is calculated from a separate NLO code [3] as:

$$Kfactor(x_1, x_2) = \frac{d^2\sigma_{NLO}/dx_1dx_2}{d^2\sigma_{LO}/dx_1dx_2} \tag{3.27}$$

The K-factor can become significantly larger than 1 and can also modify the shape of the LO cross section (See figure 3.7). The K-factor is saved in 100 x 100 grid in x_1-x_2 phase space, with both x_1 and x_2 ranging from 0 to 1.

Additionally, to account for the luminosity, beam current (by default this value is set at 2e12 protons/second) and nucleon density of the target nucleus is included in the weight. Additionally, the weight includes the factor $1/((M_{max} - M_{min})(x_{Fmax} - x_{Fmin}))$ to account for the thrown event density in the phase space.

Thus, event rate (assuming 2e12 protons per second) in a particular kinematic range is calculated by summing up the weights of all events in that kinematic range and dividing by the number of events thrown.

3.2.2 J/ψ and ψ' dimuon generator

Unlike the Drell-Yan generator, the mass of dimuon from charmonium is set to their corresponding mass. The angular distribution ($cos\theta$ and ϕ) is thrown flat. The differential cross-section of J/ψ has a gaussian form in x_F obtained from a fit to the Color-Evaporation-Model calculation, and the normalization is obtained

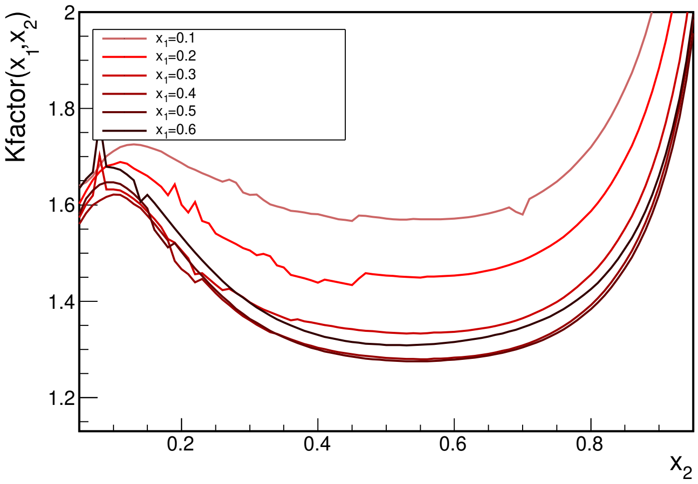

Figure 3.7: K factor as a function of x_2 for shown values of x_1. The calculation[3] is performed using CT14 LO and NLO PDFs

from a parametrization to the E789 paper taken from [44]

$$\frac{d\sigma_{J/\Psi}}{dx_F} = Ae^{-B\sqrt{\tau}} \left(\frac{e^{-x_F^2/2\sigma_{J/\Psi}^2}}{\sigma_{J/\Psi}\sqrt{2\pi}} \right) \tag{3.28}$$

where $A = 1464$ nb, $B = 16.66$, $\sigma_{J/\Psi} = 0.2398$. Additionally, branching ratio $B(J/\Psi \to \mu^-\mu^+) = 0.0594$ is also multiplied to the total cross section. For Ψ' cross section, the J/Ψ cross section is multiplied by a scale $\Psi'_{scale} = [B(\Psi' \to \mu^-\mu^+) \times \sigma_{\Psi'}]/[B(J/\Psi \to \mu^-\mu^+) \times \sigma_{J/\Psi}] = 0.019$. Just like Drell-Yan generator, the weight of each dimuon also includes luminosity (beam current and nucleon density) and phase space factor $1/(x_{Fmax} - x_{Fmin})$.

3.3 Geometry

The geometry is defined in two parts in the Monte Carlo.

a) First part consists of construction of the spectrometer and magnetic fields that need to be fed to GEANT for simulating particle passage through it.

b) Second part consists of information that digitizes and translates the output from GEANT simulation to a format that mimics the collected data format.

The former section of geometry requires construction of the following objects:

1) G4Material: This object contains information about material density, element composition and its percentage fraction in mass.

2) G4VSolid: This object contains the dimension and shape of each component of the spectrometer.

3) G4LogicalVolume: Connects each G4VSolid with a G4Material and contains information about whether a volume is a detector or not. Each logical volume is connected to one or more physical volume which contains information about the position and orientation of the spectrometer components.

The latter part of geometry contains detailed information about detector planes in each physical volume. It includes information such as centre of each plane, its orientation, number of wires and cell width of drift chambers, number of paddles and paddle overlap width of hodoscopes. These details are required for converting the hit information on a detector to the corresponding chamber wire and hodoscope paddle number. This part of geometry description also includes files that are required to link the hodoscope paddles or chamber wires to their associated DAQ electronic component, such as rocID, boardID and channelID.

3.4 Running GMC

In order to run GMC, a couple of pre and post helper programs need to be executed for the entire GMC production to be ready. A TableLoader program is run before running GMC. This program reads geometry and magnetic field files and saves them in the MC schema on MySQL database. These tables are used by GEANT during simulation. Once the geometry tables are ready, the GMC is ready to run. The GMC productions are run by submitting 350 sub-jobs parallely to the open science grid. More details on the exact procedure for submitting jobs on grid are found here [45]. Each sub-job (submitted with a different seed to avoid repetition) has 100,000 MC events, out of which approximately 3000 (for DY) dimuons pass the spectrometer acceptance cuts. Thus, combining all instances of GMC together, there are about 1 million dimuon events (DY) per GMC production. Since the GMC instances are run in parallel, it takes about 3 hours for the sample to be ready for post production steps. There are 2 post production steps. First, the TableMerger program is executed to combine the tables from all sub-jobs into 1 giant table. For example, mTrack_1, mTrack_2, ..., mTrack_350 are combined together into a single table called mTrack. The last step is to index the tables. This step is important to improve the querying time so that required MC data can be accessed quickly.

3.5 GMC Output

The output from GMC is stored in MySQL database. The GMC output table names have a prefix m, like mRun or mTrack. The mRun table lists the settings such as number of generated events, magnetic field strength, PDF, range of kinematic variables etc. The mTrack table contains the track information like particleID, its position and momentum at certain z-positions, parent particleID (for secondary and later generation of tracks) and generation method. The mDimuon table contains dimuon variables like M, x_F, x_B, x_T, $cos\theta_{CS}$ and ϕ_{CS}. It also includes information about dimuon momentum and positions. GMC also outputs mHit table. It contains information such as the momentum of particle when it hit different detectors. Such information is not available in the real data. These mTables are used to compare the reconstructed values with the "truth" (or thrown) values. In addition to the truth tables the MC also outputs Hit table. It is formatted such that its structure is same as data. This table is utilized by the tracking software (kTracker) for MC reconstruction.

Chapter 4

Data analysis

4.1 Data set

SeaQuest first received the proton beam in the beginning of 2012, which allowed the commissioning data to be taken. Soon after a short period of running, the Main Injector was shut down for upgrade. After the Main Injector restarted in late 2013, the collection of physics data started in 2014. A timeline of SeaQuest data taking is depicted in figure 4.1. This thesis includes data from run 2 and run 3. A brief summary of run 2 and run 3 data is tabulated below

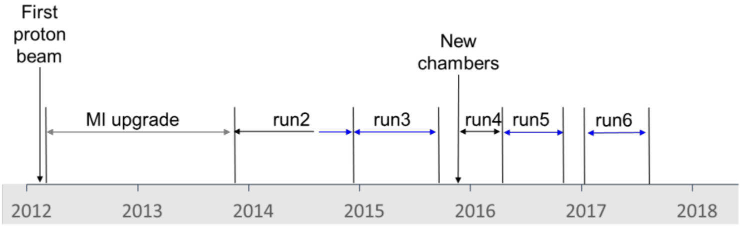

Figure 4.1: Timeline for SeaQuest data taking

Run period	Roadset	Run range	Beam offset (cm)	B orientation
2	57	8912-10420	0.4	+
2	59	10421-10912	0.4	+
3	62	11075-12435	1.6	+
3	67	12525-15789	1.6	-
3	70	15793-16076	1.6	-

Table 4.1: Summary of Run period 2 and Run period 3 data. A typical run is an hour long collection of data $\sim$ 1 GB in size. Roadset column refers to the version of trigger matrix used for that duration. Beam offset and B orientation column lists the offset of the beam (in y-direction) and the orientation of magnetic field, respectively.

4.2 Track reconstruction

The tracking software used in SeaQuest is called 'kTracker' where the prefix 'k' stands for Kalman filter method [46] which is used in the code to find tracks. The tracking software was developed by Kun Liu, one of SeaQuest collaborators. The code consists of three main parts, which are briefly described as follows:

4.2.1 Pre-tracking cuts

There are four types of hit removal criteria applied to each event before the tracker attempts to find tracks. This step is very important for several reasons. Getting rid of hits that are most likely not a part of muon tracks, makes it easier for the tracker to identify potential signal muon tracks. Furthermore it reduces the runtime of tracking software as there are less number of hit combinations that the tracker needs to go through.

In-time cut: All the chamber hits that fall within a time window around a triggered event pass this cut. Since the drift times for chambers are relatively long compared to the periodicity of beam buckets, the in-time window can be as large as 600 ns (corresponding to ±15 beam buckets).

After pulse cut: Due to electronic noise, the drift chamber wires tend to have multiple pulses after the first hit. In such a case, only the first pulse of each channel is accepted and the after pulses are discarded.

Cluster removal cut: The third category of hit removal cuts is called the cluster removal cut. This cut is further divided into three subcategories, namely, electronic noise, cell-edge hits and delta rays. Delta rays are electrons knocked off by primary ionizing particle when passing through wire chamber. The knocked off electron is capable of producing secondary ionization. Some of these electrons scatter at large angles and travel parallel to the X-Y plane and fire several wires. In this case, only the edge hits are retained as potential true hits caused by muon tracks and the central chunk of wire hits are dropped.

When a muon track passes a wire plane close to the cell edge, it will often cause two adjacent wires to fire. For this case, the wire with larger drift distance is removed.

The drift chambers are prone to electronic noise which leads to the third category of cluster hit removal criteria. It takes into account the hit clusters caused by electronic noise. If the hit clusters are recorded with similar TDC time (within 10 ns), then they are identified as electronic noise and thus removed. Figure 4.2 depicts the algorithm for cluster removal.

Trigger Hodoscope masking: The hodoscopes have a time resolution shorter that the RF bucket periodicity and hence are used for triggering. Only the chamber hits that fall behind the fired hodoscope paddles are retained and others are discarded. The in-time hodoscope hits on all 4 stations are combined to form all possible road combinations. These combinations are checked against the active trigger road setting

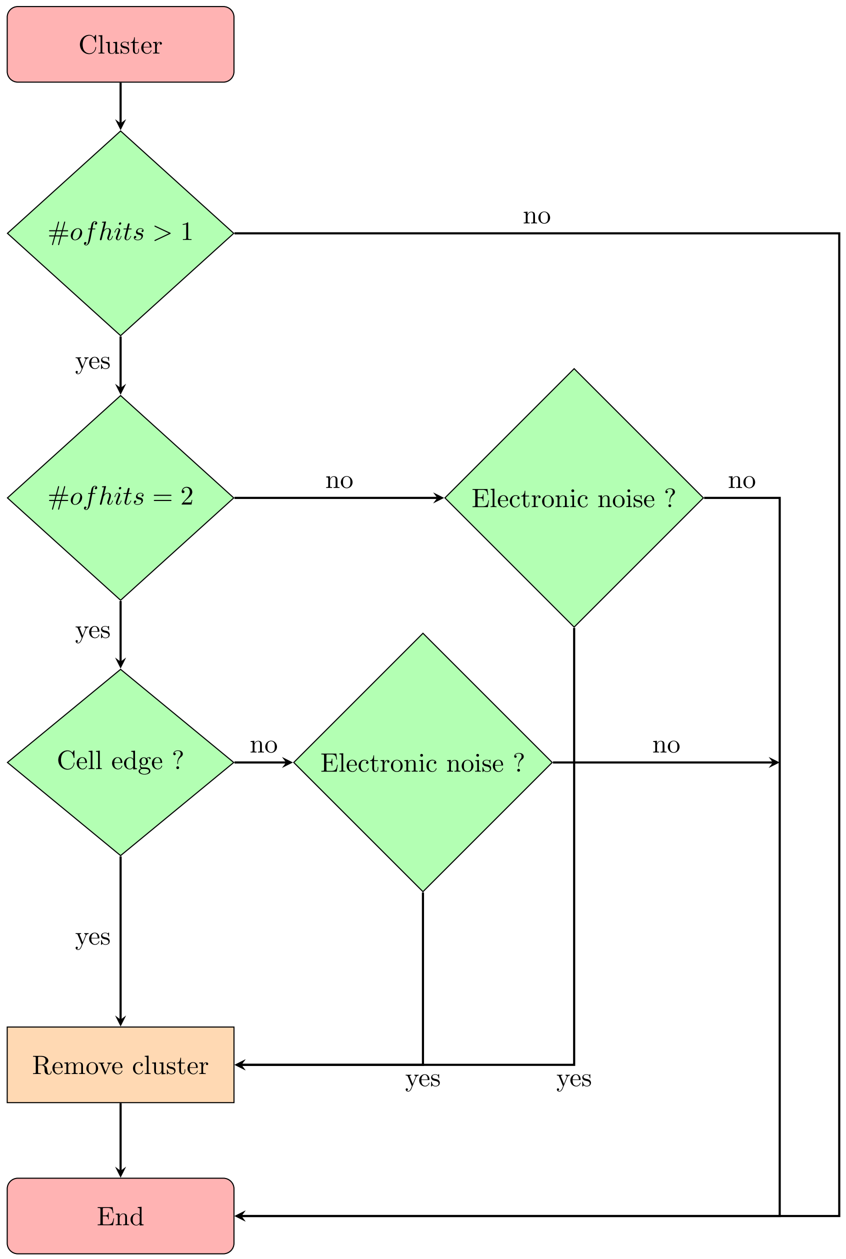

Figure 4.2: Flowchart depicting the cluster removal algorithm

during that data taking period. Using the trigger road setting information further reduces the random chamber hits by removing chamber hits that fall behind fired hodoscope paddle but are not a part of trigger roads.

4.2.2 Track finding

Track finding is the next step after dropping random hits. This step proceeds in four steps, namely, tracklet formation at each station, connecting tracklets from stations 2 and 3, projection to station 1 and global track construction.

Tracklet is a small segment of track formed by joining hits from each view in a chamber. The track finding stage starts from finding hit triplets in both station 2 and 3. The steps to find triplets are depicted in figure 4.3. First, the hits in both primed and unprimed X-plane are picked. Based on X plane hit pairs, overlapping U-plane hits are selected in a narrow window around the X-view. The X-U overlap hits are then used to select V-plane hits. The search window in each plane is determined by the cell width and the maximum allowed tracklet slope (The slope is determined such that the tracklet is pointing towards target). Thus, the X-U-V triplets are selected and joined to form tracklets by fitting a straight line through all the selected hits. Several tracklets can share the hits. A tracklet is discarded if,

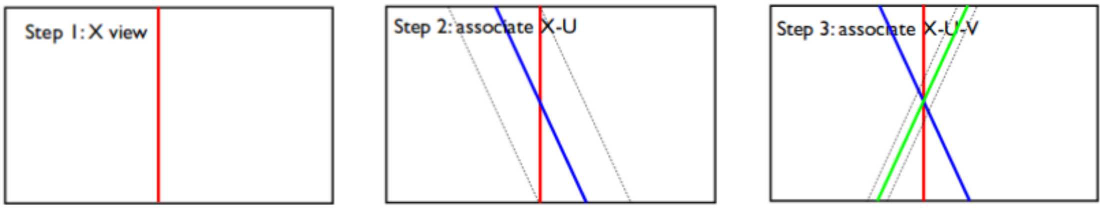

Figure 4.3: Schematic representation of triplet reconstruction

- the χ^2 is more than 40
- there are less than 4 hits
- the tracklet does not have at least 1 hit from each view
- the tracklet does not point to target (i.e., x and y slope of tracklet is greater than (0.15,0.1))
- the tracklet points toward a hodoscope paddle that did not fire
- the absolute value of x, y position is greater than (150 cm, 50 cm)

The tracking fails if no tracklets were found in either station. If tracker was successful in finding tracklets, it proceeds as follows. All combinations of stations 2 and 3 tracklets are then picked and attempt is made to connect them to form partial tracks. Loose cuts on the slope of the partial track and χ^2 of the fit are applied to select potentially good partial tracks. If two partial tracks share more than 34% of hits, the partial track with worse χ^2 is removed. An additional muon identification cut is applied to find corresponding hits on the proportional tubes (station 4). The multiple scattering of track due to the iron wall placed before station 4 is taken into account.

The next step involves connecting the DC2-DC3 partial track to the appropriate tracklet at station 1. This step is quite complex as station 1 being the most upstream station usually contains many hits. Furthermore, the KMAG is situated between station 1 and 2. Hence appropriate magnetic kick due to KMAG needs to be taken into account. The search window at station 1 is determined using the sagitta ratio method. As shown in figure 4.4, sagitta is defined as the distance between track and the line connecting station 3 triplet to dump or target location. s1 and s2 are the sagitta at station 1 and 2 location, respectively. The idea behind this method is that the ratio of sagitta s1 and s2 should be a constant as the z locations of station 1 and 2 as well as the transverse momentum kick due to magnetic field is fixed. The sagitta ratio is calculated from MC simulations and set as $r_d = 1.5$ and $r_t = 1.85$ if track vertex is dump and target, respectively. The search window is determined as a percentage of s2 (sagitta at station 2).

$$\Delta y_{1t} = |s_{2t}.w_t|, \tag{4.1}$$

where Δy_{1t} is the window width perpendicular to the expected location of tracklet at any station 1 plane (y_{1t}) for interaction happening inside target. In the above equation $w_t = 0.25$ The search window, Δy_{1d} is also calculated assuming the interaction happens in the dump with the expected tracklet position being y_{1d}. In this case the $w_d = 0.3$. Station 1 hits that fall in the window around the projected centre are used to form tracklets and paired with partial track to form global track candidates.

In the global track construction step, bad hits are iteratively removed if their residual is 3 times larger than the resolution, refitting the track after each iteration. Once convergence is reached, the track has to go through the following selection criteria,

- It should point to fired hodoscope paddle at each station.
- The momentum should be in between 5 GeV and 100 GeV.
- It should have at least 4 hits on each wire chamber with 1 hit at each view.

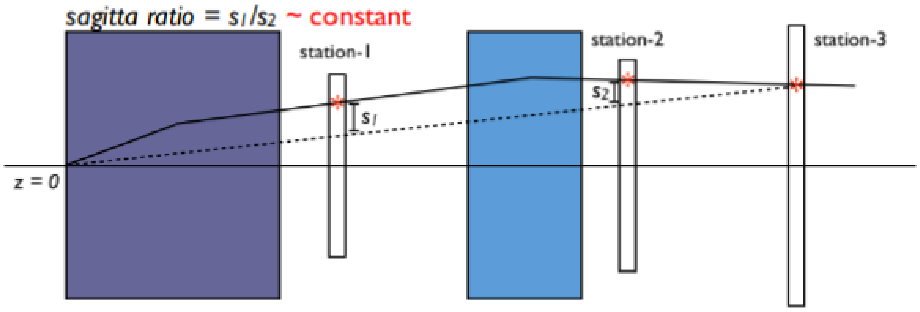

Figure 4.4: Schematic of sagitta method used for track finding. The plot is showing the X (or bend plane) view. The ratio of sagitta is a constant. The value of the constant is determined from Monte Carlo study and is determined to be 1.85 for target and 1.5 for dump.

4.2.3 Track fitting

The tracks that pass all the conditions are passed on to Kalman Filter. The Kalman Filter method is used for fine-tuning and smoothing of the muon tracks. Kalman filter is a recursive method that uses series of measurements over time to find the optimum solution [46]. Figure 4.5 shows the flowchart of the algorithm for track finding. In case of SeaQuest these series of measurements are the recorded hits at each plane. The Kalman filter method starts with an initial estimate of state vector (to describe the tracklet) and covariance matrix (to describe the uncertainty) at DC3. The Kalman filter algorithm propagates the initial estimate to predict the state variable at DC2. The propagation steps require the knowledge of specified physics model. kTracker uses GEANT to simulate the physics process and propagation of muon tracks through the spectrometer. The prediction is combined with the measurement using weighted average with more weight given to the one with lower uncertainty. Similarly, the updated state variable at DC2 is used to make prediction for DC1 and target location.

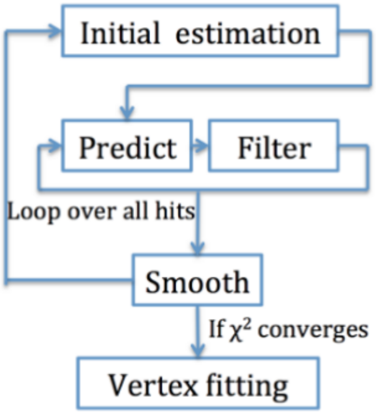

Figure 4.5: Flow chart of Kalman filter algorithm for track fitting

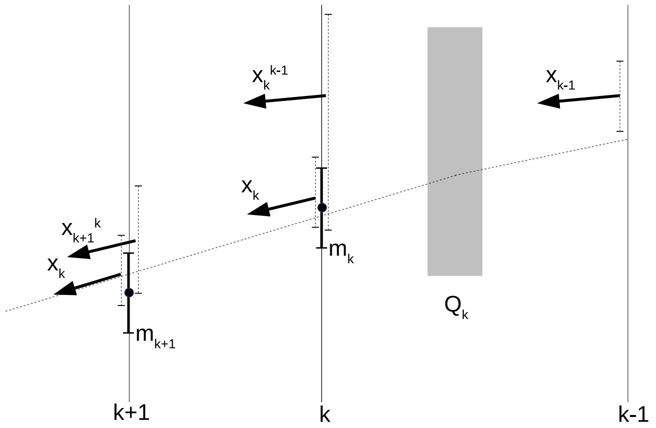

Figure 4.6: Schematic representation of Kalman filter workflow. The estimate and measurement are denoted as $\tilde{x}_j^i$ and m_j respectively. The subscript j represents the j-th detector plane and superscript i represents the detector (j-1) whose state variable was used as input to make prediction for j-th detector. The combined estimate of state variable by taking into account the measurement m_j and prediction $\tilde{x}_j^i$ is represented by $\tilde{x}_j$

4.2.4 Vertexing

After the μ^- and μ^+ tracks are found by the tracker, they are combined to form dimuon pairs. The vertexing process also involves Kalman Filter method for dimuon vertex extraction from the dimuon pairs. Before the vertex can be extracted, each muon track needs to be traversed upstream towards the target area. This is achieved by slicing the FMAG into segments. For each FMAG segment the transverse (p_T) kick and energy loss is applied to the tracks. After traversing through the FMAG, the tracks are extended to the target region along a straight line and the location of track's closest approach to the beamline is obtained. The initial dimuon vertex is estimated as the average of both muon's distance-of-closest-approach location. The dimuon vertex estimate is fed into Kalman filter and the track's state variables at Station 1 are readjusted to get an updated vertex location. This process is iterated until convergence is reached.

4.3 Drell-Yan dimuon selection

Several quality and analysis cuts are applied to the reconstructed dimuons to filter out the signal dimuon events. These cuts are categorized into different levels: Spill level, event level, track level and dimuon level applied in that order.

4.3.1 DataQuality/Spill Cut

At the spill level, Data quality cut is applied. It is actually a bunch of cuts clustered together into a single quantity termed as DataQuality which is zero when all the listed cuts are satisfied. The cuts are tabulated in table 4.2

Quantity \ Roadset	57, 59	62, 67, 70
TargetPos	[1,7]	[1,7]
TargetPos2	TargetPos	TargetPos
TSGo	[1e3,8e3]	[100,6000]
AcceptedFPGA1	[1e3,8e3]	[100,6000]
AfterInhFPGA1	[1e3,30e3]	[100,10000]
AcceptedFPGA1/AfterInhFPGA1	[0.2,0.9]	[0.2,1.05]
FMAG (in Amps)	[1950,2050]	[1950,2050]
KMAG (in Amps)	[1550,1650]	[1550,1650]
G2SEM	[2e12,1e13]	[2e12,1e13]
QIESum	[4e10,1e12]	[4e10,1e12]
Inhibit	[4e9,1e11]	[4e9,1e11]
Busy	[4e9,1e11]	[4e9,1e11]
DutyFactor	[15,60]	[10,60]
N of tracks/spill	> 0	> 0

Table 4.2: DataQuality cuts for run 2 and run 3 data

A brief description of each of the variables is as follows: TargetPos is the identification number of the target which is in the beam path. TSGo is the number of triggers (irrespective of the trigger type) collected by the trigger supervisor. AcceptedFPGA1 and AfterInhFPGA1 is the number of accepted and inhibited FPGA1 triggers, respectively. KMAG and FMAG is the current setting (in Amps.) of the magnets. G2SEM is the total beam intensity measured by the SEM located at the NM3 area. QIESum is the sum of beam intensity (in QIE units) measured by the BIM. Inhibit and Busy are the sum of inhibited protons and sum of protons when trigger was busy. Duty factor defined as $< I >^2 / < I^2 >$ is a measure of beam quality.

4.3.2 Event level cut

The only cut that is applied at this stage is the $MATRIX1 = 1$ which is essentially selecting the dimuons that triggered the FPGA1 trigger (dimuon physics trigger)

4.3.3 Track level cuts

The track level cuts that are applied to both μ^- and μ^+ tracks are listed in table 4.3

Variable	Variable description	Good range
z_0	z position of track's closest approach to beam line	(-320 cm,-5 cm)
$x_T^2 + (y_T - \text{beamOffset})^2$	radial distance of track from beam line at z=-129 cm	< 320 cm^2
$x_D^2 + (y_D - \text{beamOffset})^2$	radial distance of track from beam line at z=42 cm	(16 cm^2,1100 cm^2)
$abs(abs(px_1 - px_3) - 0.416)$	difference in x momemtum at st.1 and st.3 (offset by KMAG kick)	< 0.008 GeV
$abs(py_1 - py_3)$	difference in y momemtum at st.1 and st.3	< 0.008 GeV
$abs(pz_1 - pz_3)$	difference in z momemtum at st.1 and st.3	< 0.08 GeV
$\chi^2_{target} < 1.5\chi^2_{upstream}$ $\chi^2_{target} < 1.5\chi^2_{dump}$	χ^2 when the track is forced to pass through z=-490(upstream), z=-129(target), z= 42(dump)	N/A
χ^2_{target}	χ^2 when track is forced to pass through z =-129	< 15
$abs(\chi^2_{target}(\mu^-) + \chi^2_{target}(\mu^+) - \chi^2_{dimuon})$		< 2
numHits	total number of hits on wire chamber by each muon track	> 13
$\chi^2/(nHits - 5)$	χ^2/NDF	> 12
pz_1	z momentum at station 1	(9 GeV,75 GeV)
y_1/y_3	y position of track at St.1 and St.3	< 1
$y_1 \times y_3$		> 0
$abs(py_1)$	absolute value of track y momentum at St. 1	> 0.02 GeV

Table 4.3: Track level cuts

4.3.4 Dimuon level cuts

The cuts applied to the reconstructed dimuons are listed in table 4.4 In addition to the above selection cuts there are also cuts applied to reject very high occupancy and high intensity events listed in table 4.5.

Variable	Variable description	Good range
dz	z position of dimuon vertex	(-280 cm,-5 cm)
dx	x position of dimuon vertex	(-0.25 cm,0.25 cm)
dy- beamOffset	y position of dimuon vertex	(-0.22 cm,0.22 cm)
$dx^2 + (dy - \text{beamOffset})^2$	radial distance of dimuon vertex	< 0.06 cm^2
$abs(dpx)$	absolute value of dimuon x momentum	< 1.8 GeV
$abs(dpy)$	absolute value of dimuon y momentum	< 2 GeV
dpz	absolute value of dimuon z momentum	(38,116)
$dpx^2 + dpy^2$	dimuon transverse momentum squared	< 5 (GeV)^2
mass	dimuon mass	(4.2 GeV,8.8 GeV)
x_F	Feynman x	(-0.1,0.95)
x_T	Bjorken x of target	(0.1,0.58)
$cos(\theta)$	polar angle in Collins-Soper frame	(-0.5,0.5)
abs(trackSeparation)	distance (in z)between points of closest approach between μ^- and μ^+	< 270 cm
numHits(μ^-)+numHits(μ^+)	sum of total number of hits by μ^- and μ^+ track	> 29
numHits1(μ^-)+numHits1(μ^+)	sum of number of hits by μ^- and μ^+ track on DC1.1	> 8
$y_3(\mu^-) \times y_3(\mu^+)$		< 0
χ^2_{dimuon}	χ^2 when both μ^- and μ^+ tracks are forced to pass through dimuon vertex	< 18
$abs(x_1(\mu^-) + x_1(\mu^+))$	sum of x position of tracks at St. 1	> 42 cm
$abs(\chi^2_{target}(\mu^-) + \chi^2_{target}(\mu^+) - \chi^2_{dimuon})$		< 2

Table 4.4: Dimuon level cuts

Variable	Variable description	Good range
D1	Total intime hits on DC1.1	< 400
D2	Total intime hits on DC 2	< 400
D3	Total intime hits on DC 3	< 400
D1+D2+D3	Total intime hits on all chambers	< 1000
Trigger intensity	Number of protons in the triggering bucket	(0,80000)

Table 4.5: Cuts on occupancy and intensity

4.4 Drell-Yan Monte Carlo analysis

The cuts described in the above section are applied on LD_2 and LH_2 Drell-Yan Monte Carlo. The kinematic distribution, residual and differential acceptance for x_F, x_B, x_T, mass and p_T are shown in this section.

4.4.1 Kinematic distribution from Drell-Yan Monte Carlo

The plots in 4.7 show the kinematic distributions of LD_2 messy Monte Carlo after applying all the standard cuts except mass cut.

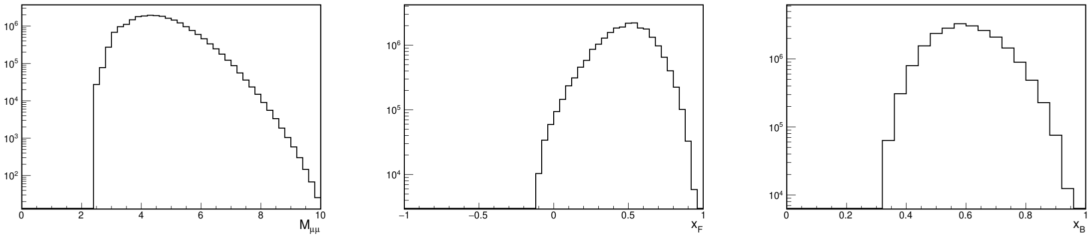

(a) mass (b) x_F (c) x_B

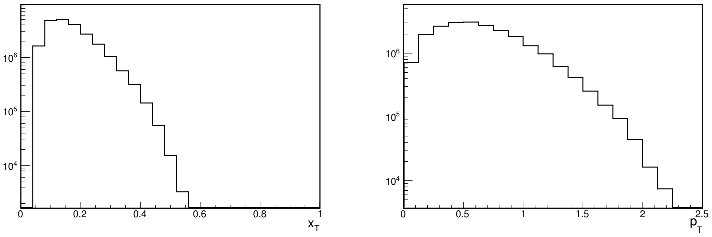

(d) x_T (e) p_T

Figure 4.7: Kinematic distribution from MC analysis

4.4.2 Spectrometer acceptance

The plots in figure 4.8 show the spectrometer acceptance as a function of various dimuon kinematic variables. The acceptance here is calculated as

$$\text{acceptance} = \frac{\text{Messy MC (Standard analysis cuts)}}{4\pi\text{MC (xF cut)}} \tag{4.2}$$

This definition of acceptance takes into account the inefficiency of the tracker in high occupancy events. The messy MC has embedded NIM3 hits. The Addition of NIM3 hits to true MC signal hits makes it difficult for the tracker to find signal tracks leading to the inefficiency.

4.4.3 Spectrometer resolution

The plots in figure 4.9 show the spectrometer resolution as a function of the dimuon kinematic variables. The resolution for each variable is also listed in table 4.6

Variable	Resolution
$M_{\mu^-\mu^+}$	0.27 GeV
x_F	0.03
x_B	0.02
x_T	0.02
p_T	0.2 GeV

Table 4.6: Spectrometer resolution for different kinematic variables

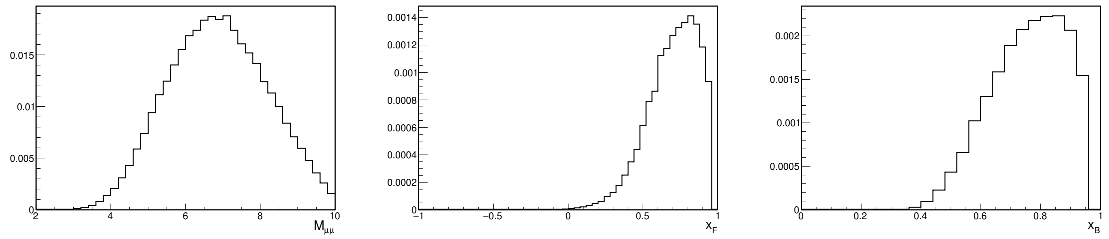

(a) mass acceptance (b) x_F acceptance (c) x_B acceptance

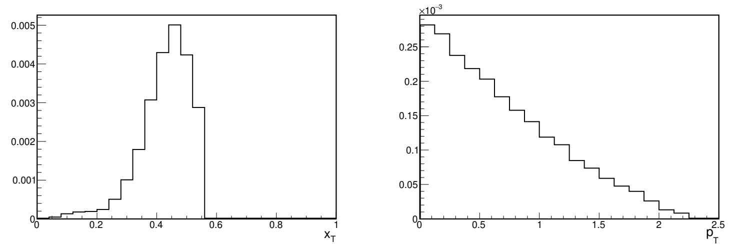

(d) x_T acceptance (e) p_T acceptance

Figure 4.8: Spectrometer acceptance

4.5 Drell-Yan kinematic distributions from data

In order to obtain the final Drell-Yan events from the data, the mass-fit method has been used. The mass-fit method uses the component (J/Ψ, Ψ' and DY) mass distribution generated from the MC simulation, background shape generated by mixing the single muon trigger (FPGA4) data, and empty flask data. Before proceeding with the mass fit, the Drell-Yan Monte Carlo shapes need to be revisited as described in section 3.2.1.

4.5.1 p_T re-weighting in DY Monte Carlo

The input p_T distribution shape in DY Monte Carlo uses the Kaplan functional form

$$f(p_T) \propto \frac{p_T}{(1+\frac{p_T^2}{p_1^2})^6} \tag{4.3}$$

where, $p_1 = 2.8$ GeV. The parameter p_1 is related to the broadness of the p_T distribution. The SeaQuest data indicate that the p_1 value used in MC is broader than what it is. Additionally, the value of p_1 is dependent on x_F. The dependence of p_1 on x_F has also been reported in pion induced Drell-Yan experiment E615 [36]. Hence, the tuning of p_T distribution is required to achieve appropriate kinematic distributions (which are integrated over p_T). Getting the correct p_T shape from the data is challenging as an iterative procedure needs to be followed, ideally. The empty flask, charmoniums ($J/\Psi, \Psi'$) and accidental background

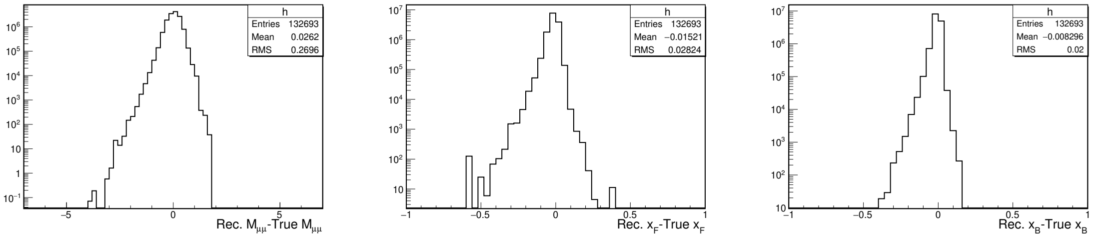

(a) mass resolution (b) x_F resolution (c) x_B resolution

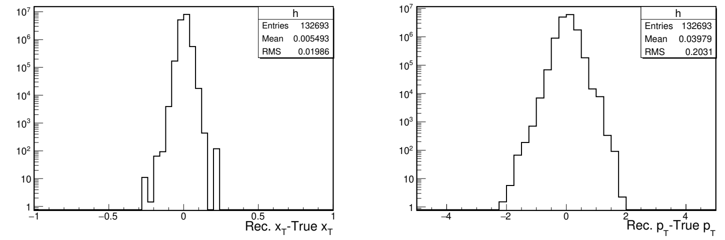

(d) x_T resolution (e) p_T resolution

Figure 4.9: Spectrometer resolution for different kinematic variables. For each MC event the difference of the reconstructed and the true value for any given variable is plotted as histogram. The RMS of this distribution is the resolution.

contribution needs to be subtracted from the data to arrive at the Drell-Yan contribution. However, the normalization of each contribution (except empty flask) is obtained from mass-fit method. The mass-fit method itself relies on the shape of each component including the Drell-Yan, the shape of which is not precisely known due to the unknown p_T distribution at $\sqrt{s} = 15.01$ GeV/c. Additionally, the uncertainty in the PDF shape also adds to the shape uncertainty of the Drell-Yan component.

First order p_T reweighting was performed using SeaQuest data. Standard analysis cuts are applied on the data (LD_2 and flask). Normalized flask yield is subtracted from LD_2 data in three x_F bins. The yields are corrected for acceptance in each p_T bin for all three x_F bins. It should be noted that the incorrect p_T shape in the MC should not affect the acceptance calculation as a function of p_T. The quantities which are integrated over p_T are affected by the incorrect p_T shape. The acceptance corrected p_T distribution is fit with Kaplan functional form (equation 4.2) and the parameter p_1 obtained for all three x_F bins (4.10) are used to get p_1 as a function of x_F (figure 4.11)

The p_1 parameter is plotted against the mean x_F value for each x_F bin. A linear fit through these data points are used to get p_1 value as a function of x_F (figure 4.11), which is used for 'reweighting' the MC events: The MCs are 'reweighted' as follows.

$$\mathrm{p_T\ reweight}(x_F) = \frac{(1+\frac{p_T^2}{2.8^2})^6}{(1+\frac{p_T^2}{(p_1(x_F))^2})^6}\frac{2.8^2}{(p_1(x_F))^2}, \tag{4.4}$$

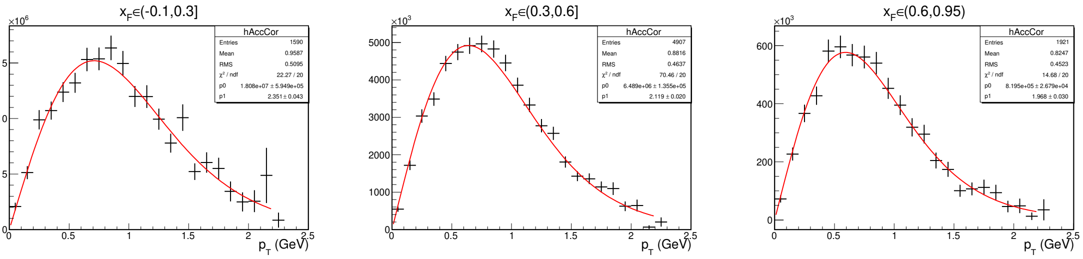

Figure 4.10: Kaplan functional form fit to SeaQuest data to obtain x_F-dependent p_T distribution at SeaQuest's beam energy.

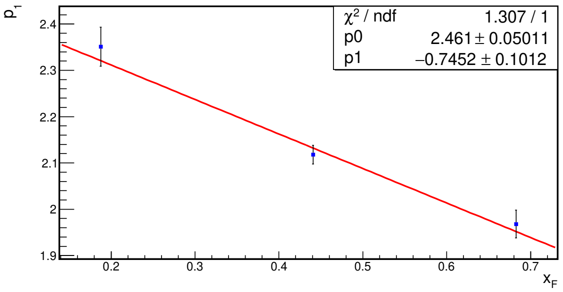

Figure 4.11: The data points are the p_1 plotted versus mean x_F. The line is a fit through the data points to get the dependence of p_1 on x_F.

where $p_1(x_F) = 2.46 - 0.745x_F$.

4.5.2 Mass spectrum fitting

Mass spectrum fitting method is used to extract the contribution of different components to the reconstructed dimuon sample. Broadly the dimuons come from three different types of components: a) physics sources (charmonium (J/Ψ and Ψ') decay and Drell-Yan process) b) accidental background (two single muons from two different interactions can conspire to look like a dimuon produced from a single interaction of beam and target) c) Contribution from empty flask data (which includes contribution from flask walls, upstream and dump interactions).

Physics sources

The shape of J/Ψ, Ψ' and Drell-Yan are determined from Monte Carlo simulation (as described in chapter 3). In order to make the simulation data resemble as closely as possible the real data, the Monte Carlo events are embedded with NIM3 (random) trigger data. The random hits are sampled from NIM3 data such that the detector occupancy distribution of the Monte Carlo is close to FPGA1 data (after analysis cuts). The addition of random hits on top of true hits generated in the simulation is helpful in extracting the

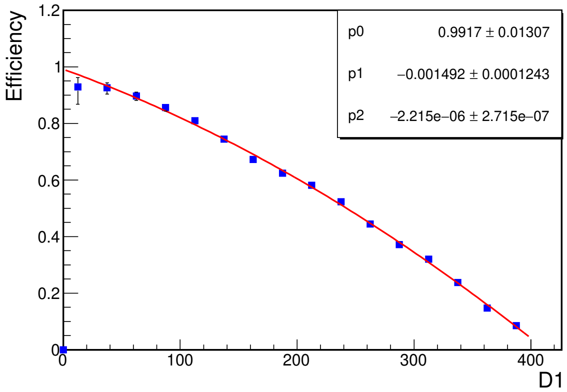

Figure 4.12: The reconstruction efficiency plotted as a function of station 1 occupancy. The efficiency is calculated by taking the ratio of messy MC events over clean MC events in each occupancy bin. Standard cuts were applied to both numerator and denominator (except the occupancy cut on clean MC). The data is fitted with a quadratic functional form.

performance of kTracker with increasing number of hodoscope and chamber hits. The NIM3 hits embedded Monte Carlo are referred to as 'messy' MC. Since the reconstructed data suffer from similar reconstruction inefficiency caused by random hits, messy MCs are used for fitting the data. Figure 4.12 shows reconstruction efficiency as a function of Station 1 chamber occupancy (D1).

Empty flask subtraction

The empty flask data is collected by placing just the empty flask in the path of beam. It is used for subtracting contribution from interaction of beam with flask walls, or upstream instrumentation, or dump. The normalization of empty flask contribution is obtained from the ratio of live protons for the liquid target (LH_2 or LD_2) and empty flask. The empty flask normalization thus obtained is kept fixed in the fit to mass spectrum. Other components (DY, J/Ψ, Ψ' and mix background (explained next)) are allowed to float.

Accidental/Mixed background correction

The origin of the accidental background is random combination of single muon tracks to look like a true dimuon. Such a sample was generated by a SeaQuest collaborator, Jason Dove, by using single muon trigger data (FPGA4). These single muon tracks were divided into 3 occupancy bins before mixing. This was done to ensure that similar occupancy single tracks are mixed together. One of the many challenges of this experiment is low statistics of background data (FPGA4/single muon trigger). To partly solve this problem the single tracks have been reused during mixing. However, same combination of 2 tracks are removed to avoid repetition. The mixed background sample still suffers from low statistics problem. Hence, to enhance

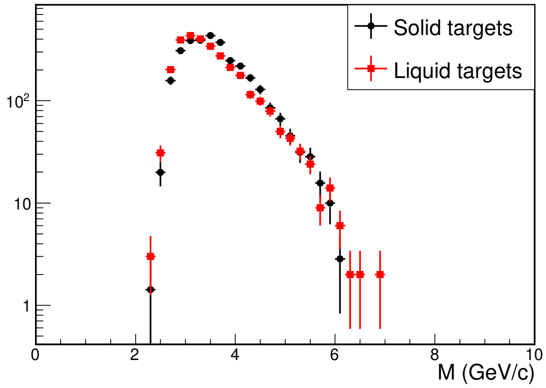

Figure 4.13: Mass distribution of mix background sample for solid targets (black solid circles) and liquid targets (red solid squares).

the statistics, mixed background sample generated from all targets are used in mass fit method. Figure 4.13 shows mass distribution of accidental background sample for solid and liquid targets.

Figure 4.14 shows the fit to the mass spectrum for LH_2(top) and LD_2(bottom) data from run 2 and run 3. The normalization of each component is allowed to float and the fitter utilizes maximum log-likelihood estimator to determine them. Only the flask normalization is provided to the fitter as the ratio of live protons on LD_2 or LH_2 target and empty flask target. The number events for each component and its statistical uncertainty is shown in the figure.

4.6 Comparison of Data and messy MC

Several improvement were made to MC simulations before getting a reasonable comparison with data. In this section, ratio of data and MC as a function of several dimuon kinematic variable are shown. For this analysis, I have chosen roadset 67 deuterium data and M026_S002 messy LD_2 MC. Using messy MCs already takes care of acceptance and rate dependent effects caused tracker inefficiency at high occupancy. Thus, the data need not be corrected for kTracker's efficiency and acceptance effects. As described in previous section, mass fit method is used to get normalization of each component. The normalization of each component is used to project its contribution for other kinematic variables. The Drell-Yan yield from data is calculated by subtracting away all the non Drell-Yan component (J/Psi, Ψ', empty flask and mixed background) from data.

The yield from messy MC is then obtained by applying all the standard cuts that were applied to the data.

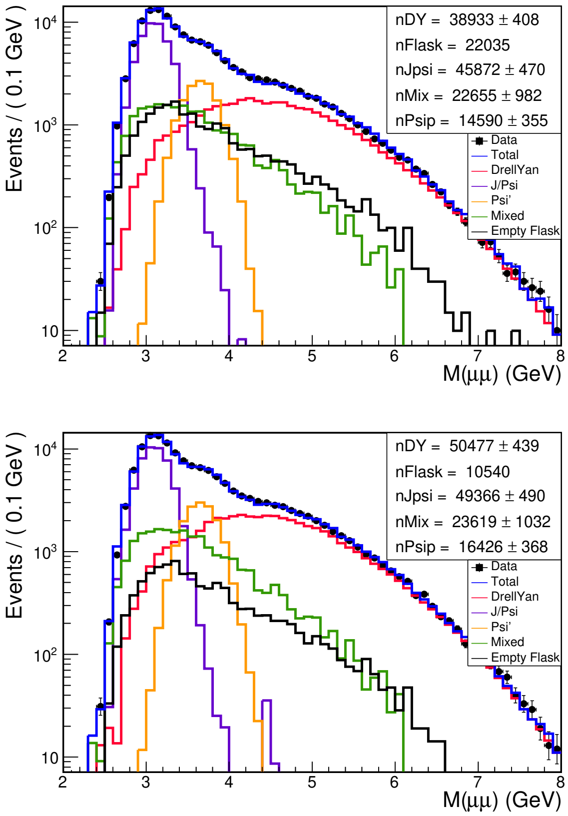

Figure 4.14: Fit to the dimuon mass spectrum from LH_2(top) and LD_2(bottom) data.The shape of each component is obtained as described in section 4.5.2. A mass cut at 4.2 GeV is sufficient to eliminate the contribution of charmonium. However, the mix-background contribution(green) extends all the way up to 6 GeV. Hence, mix background subtraction is important.

The yield in each bin is normalized as follows to match the live protons on LD_2 target.

$$\text{GMC normalization} = \frac{\text{live protons on target}}{\text{sum(eventsThrownPhysical)} \times \text{beamCurrent}}, \tag{4.5}$$

where live protons on LD_2 target for roadset 67 is $7.70196e16$, sum(eventsThrownPhysical) for LD2_M026_S002 MC is $2.8297342e7$ and the beam current is $2e12$.

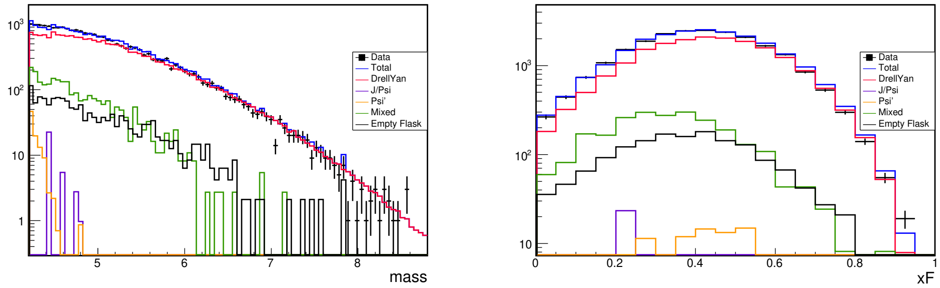

(a) mass (b) x_F

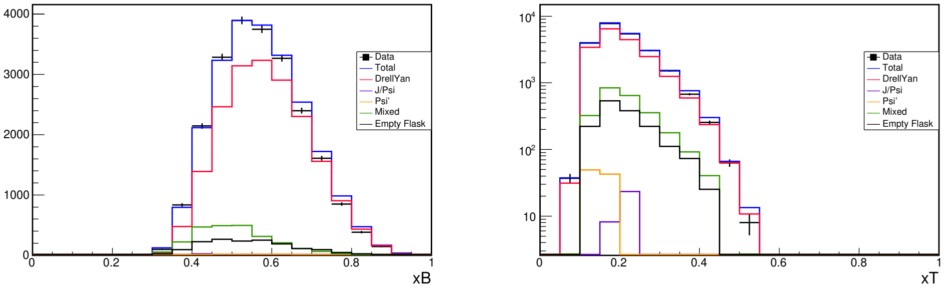

(c) x_B (d) x_T

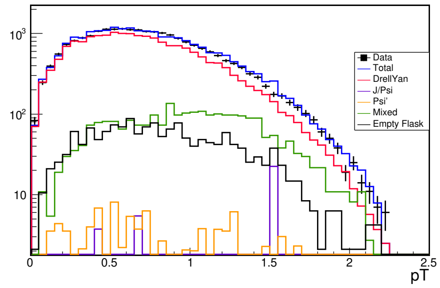

(e) p_T

Figure 4.15: Projection of Drell-Yan, J/Psi, Ψ', mix-background on different kinematic variable. The normalization for each component is obtained from mass-fit.

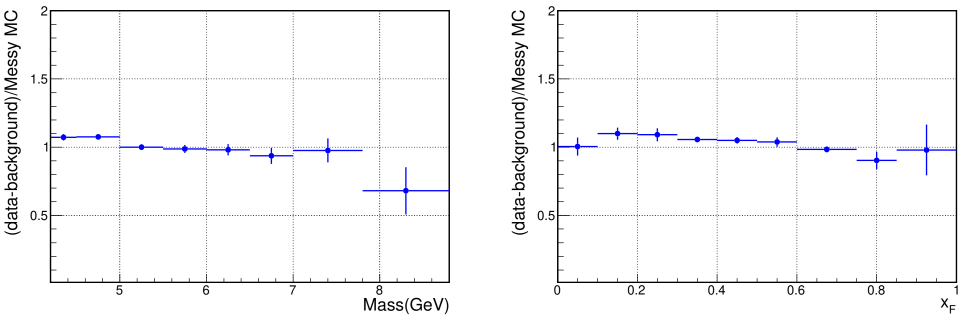

(a) mass

(b) x_F

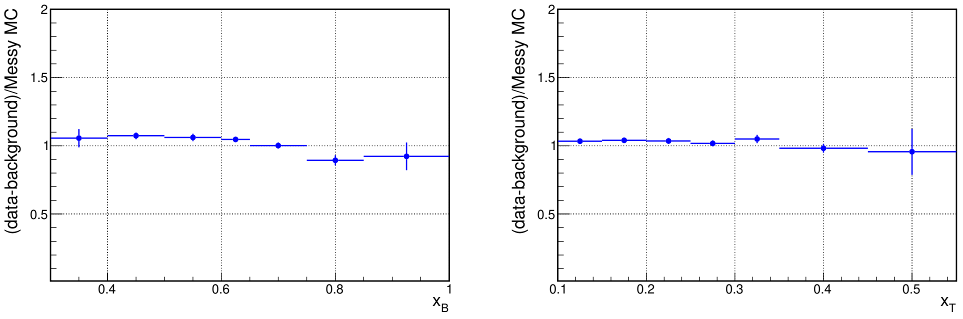

(c) x_B

(d) x_T

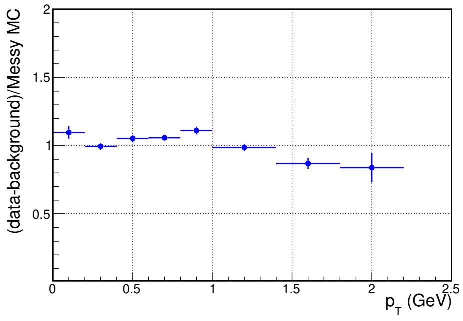

(e) p_T

Figure 4.16: (Data-background)/MC ratio shown for various kinematic variables. The ratio shows an overall good agreement between data and Monte Carlo. The error bars are statistical only.

4.7 Differential cross section calculation

The differential cross section for any process is defined as the number of measured signal events, N_{events}, in kinematic bin Ω and $\Omega + \Delta\Omega$ per number of incident particles per areal density of target particles.

$$\frac{d\sigma}{d\Omega} = \frac{N_{events}}{\Delta\Omega(N_{incident} N_{target})} \tag{4.6}$$

Here, $N_{incident}$ is the total number of of incident protons, N_{target} is the number of target nucleus per unit area after taking into account the beam attenuation factor. N_{target} can be calculated as

$$N_{target} = \frac{\rho l N_A}{A} \tag{4.7}$$

where ρ is the density of target (g/cm^3), A is the atomic mass (g/mol), N_A is Avogadro's number and l is the attenuated target length derived as $\lambda(1 - e^{-L/\lambda})$, λ and L being the nuclear interaction length (cm) and target length, respectively. Hence, the scaling form of the cross section can be written as

$$M^3 \frac{d^2\sigma}{dM dx_F} = M^3 \frac{N_{events}}{\Delta M \Delta x_F \mathcal{L}} \tag{4.8}$$

where, several quantities are combined together and expressed as $\mathcal{L}$, known as total integrated luminosity

$$\mathcal{L} = \frac{N_A \rho \lambda (1 - e^{-L/\lambda}) N_{incident}}{A} \tag{4.9}$$

In equation 4.8, N_{events} is the total number of Drell-Yan dimuons coming from deuterium or hydrogen target in a certain M and x_F bin. In ideal case where there is no background and a detector with 4π steradian coverage, N_{events} would be the recorded number of events in each bin. However, we do know that the dimuon event sample is contaminated with muon pairs coming from flask walls (flask that contains the liquid target) and other sources of accidental background which needs to be subtracted. Additionally, the spectrometer coverage and inefficiency introduced during reconstruction of muon pairs should be taken into account and equation 4.8 would be modified as

$$M^3 \frac{d^2\sigma}{dM dx_F} = M^3 \frac{N_{DY}}{\Delta M \Delta x_F \mathcal{L} \epsilon}, \tag{4.10}$$

where N_{DY} is the number of Drell-Yan events obtained by subtracting away the background muon pair coming from empty flask, mixed background and charmonium decays ($N_{DY} = N_{events} - N_{Bkg.}$). The ϵ

represents the acceptance and reconstruction inefficiency corrections.

$$\epsilon = \epsilon_{acc.}(M, x_F) \times \epsilon_{recon.eff.} \tag{4.11}$$

4.7.1 Raw Drell-Yan Yield

The standard analysis cuts listed in section 4.3 is applied to the dimuon data. These cuts are designed to select target Drell-Yan dimuon events. However, there are events coming from charmonium decay, empty flask and mixed background that survive these cuts. To eliminate the contribution from such events, a fit to mass distribution is performed (described in section 4.5.2)

$$n_{DY}(M, x_F) = n_{Data}(M, x_F) - n_{J/\Psi}(M, x_F) - n_{\Psi'}(M, x_F) - n_{mixBkg.}(M, x_F) - n_{emptyflask}(M, x_F) \tag{4.12}$$

In each mass and x_F bin the Drell-Yan yield is computed by taking the difference between raw data and sum of all other components except DY.

4.7.2 Acceptance correction/Bin migration

The acceptance in this analysis is defined as follows:

$$\epsilon_{acc.}(M, x_F) = \text{Acceptance}(M, x_F) = \frac{N_{accpt.}(M, x_F)}{N_{4\pi}(M, x_F)}, \tag{4.13}$$

where $N_{accpt.}(M, x_F)$ is the number of Monte Carlo events obtained in a given M and x_F bin, by analysing the Monte Carlo data through the same analysis code applied to the real data, while $N_{4\pi}(M, x_F)$ is the total number of thrown/generated Monte Carlo events in that particular M and x_F bin. The 4π MC did not go through the analysis procedure.

The accepted MC histogram in the numerator is filled using the reconstructed value of mass. The 4π MC histogram in denominator is filled using the 'true' value of mass. It is important to use the reconstructed value in the numerator instead of 'true' values especially for the edge bin (4.2-4.5 GeV in this case) because of the strict mass cut applied at 4.2 GeV. This cut is applied on the reconstructed mass. Hence, using the true MC in numerator will result in artificial drop in the number of events in the first mass bin since it misses the contribution from $M < 4.2$ GeV.

Using reconstructed mass histogram in the numerator makes sense because, firstly, the real data always contains reconstructed values and secondly, effects of bin migration are included in this definition. An important but subtle point is that by using the definition of acceptance as reconstructed/true, the final cross section is now obtained as a function of true mass.

The effect of using either true mass or reconstructed mass was studied using MC data. The Drell-Yan cross section in the 4π MC was compared with cross section obtained by correcting the accepted MC using both options (true and reconstructed mass values) in the definition. Figure 4.17a shows that when true value of mass is used in the numerator of acceptance, the bin migration effects are not taken care of. The edge bins is showing enhancement in the calculated cross section from accepted MC analysis. However, if reconstructed values are used in the numerator, figure 4.17b, the agreement between the cross section from 4π MC and analysed accepted MC is very good.

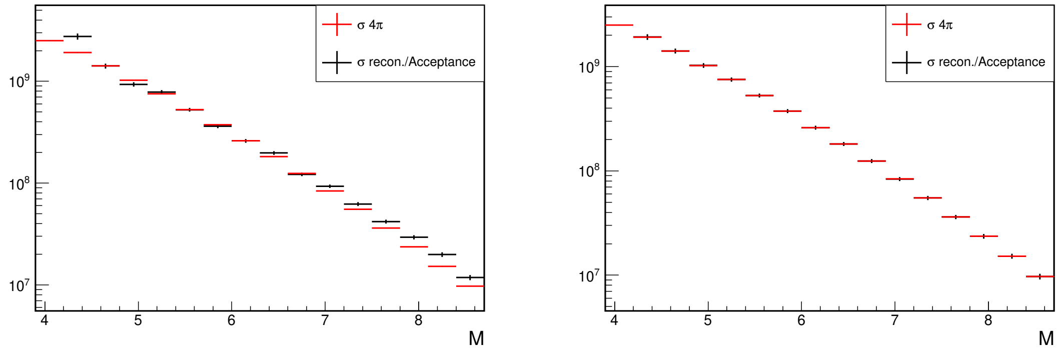

(a) Acceptance = true mass (accepted MC)/ true mass (4πMC)

(b) Acceptance = reconstructed mass (accepted MC)/ true mass (4πMC)

Figure 4.17

Additionally, the above definition of acceptance takes into account the average chamber efficiency and selection cut efficiency. The accepted MC in the numerator goes through the same analysis chain in the tracking software as real data. However, for Monte Carlo analysis the tracking software artificially introduces wire chamber inefficiency by randomly dropping 6% of hits and introducing a gaussian smearing of the hits with a width of 400 μm[47]. The GMC itself does not have the chamber efficiency or resolution included.

4.7.3 Tracker Efficiency

The tracker finds it difficult to reconstruct tracks as the number of hits on wire chambers increases. The efficiency is calculated by taking the ratio of reconstructed messy to clean events present in the Monte Carlo as a function of Station 1 chamber occupancy. Figure 4.12 shows the reconstruction efficiency. The data are fit to a quadratic functional form resulting in the following dependence of reconstruction efficiency on D1. D1 is defined as the occupancy (number of hits) of Station 1 wire chamber after the removal of out-of-time hits.

$$\mathrm{k}_{\mathrm{Eff.}} = 0.9917 - 0.001492 \times D1 - 0.000002215 \times D1^2 \tag{4.14}$$

The rationale behind not using messy Monte Carlo in the acceptance correction (described earlier) is that although the messy Monte Carlo has been embedded with random hits to simulate the 'messiness' in the real data, it does not accurately represent the occupancy distribution of the data. Hence, using messy Monte Carlo in the acceptance correction would result in incorrect rate dependence correction. Instead we use the tracker efficiency equation 4.14 to plot the inverse of kTracker efficiency $1/kEff$ for real data (Figure 4.19). The average efficiency from the occupancy distribution of LD_2 and LH_2 data is used as the reconstruction efficiency correction ($\epsilon_{recon.Eff.}$). The average tracker efficiency is different for both targets because the occupancy distribution of LD_2 is slightly higher than LH_2 (Figure 4.18) owing to the higher target density of deuterium.

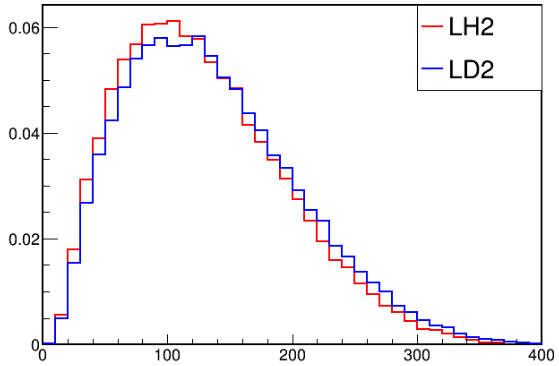

Figure 4.18: Station 1 Occupancy distribution of LD_2 (blue) and LH_2 (red) target for roadset 57-70 after applying the selection cuts. Both histograms are normalized to by their respective area under the curve.

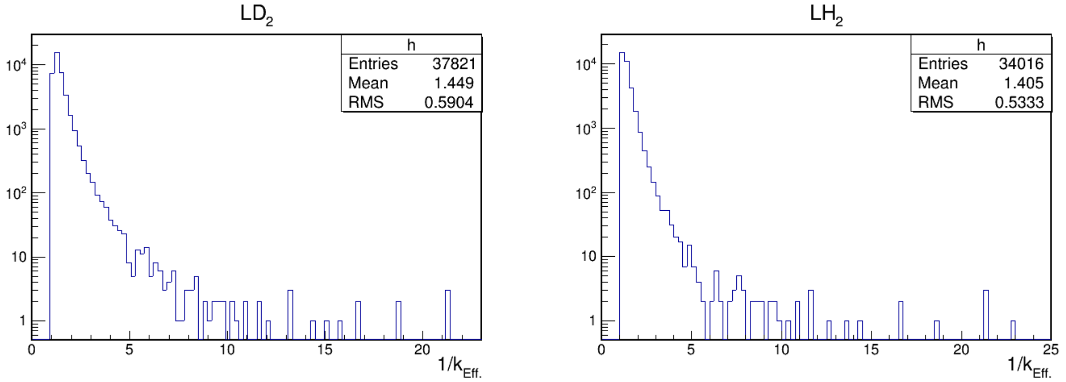

Figure 4.19: $1/kEff$ is calculated using equation 4.14 based on the D1 for each dimuon after applying standard analysis cuts. The LD_2 target average occupancy is slightly higher than LH_2, hence the tracker efficiency is lower for LD_2. Alternatively, the average $1/kEff$ ($\epsilon_{recon.Eff.}$) is higher for LD_2 as compared to LH_2.

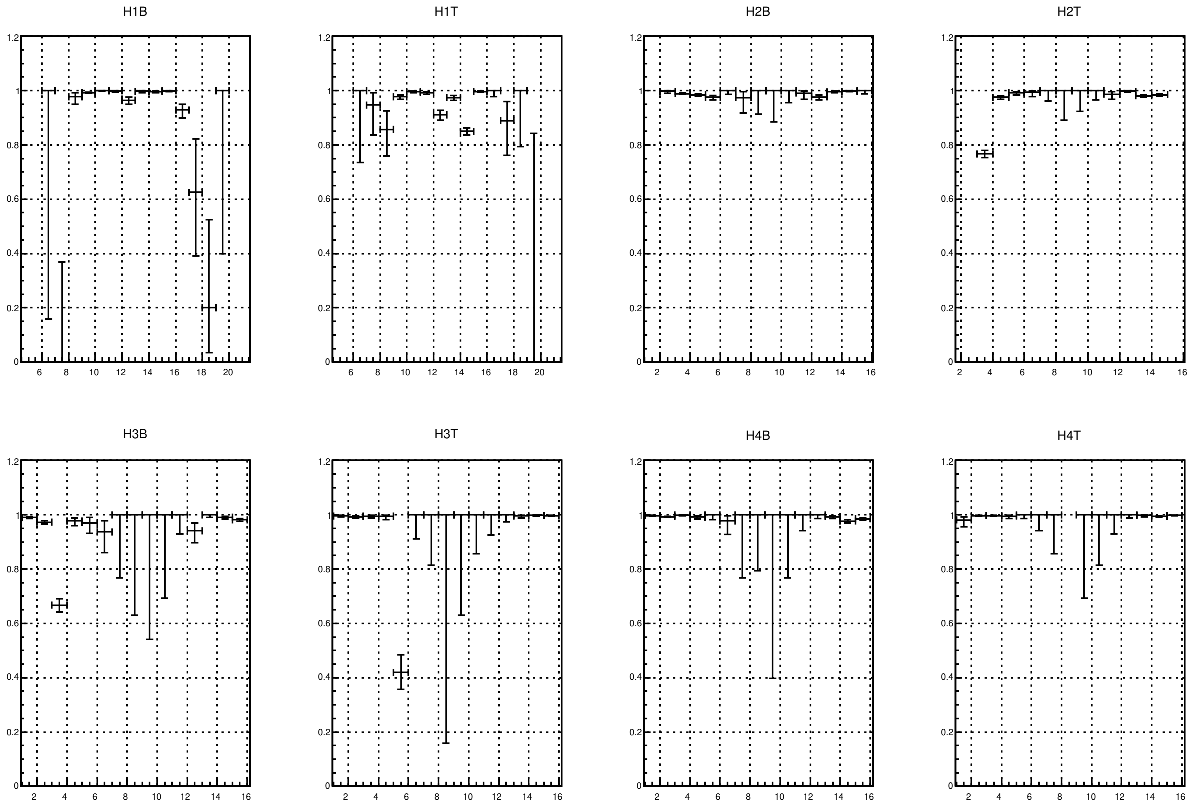

Figure 4.20: The efficiency of each hodoscope paddle from analysis of special run (with NIM1 trigger). Each station has 2 x-measuring hodoscope (top and bottom). The hodoscope name is labeled on top of sub-plots.

4.7.4 Hodoscope Efficiency

Independent measurement of bend plane (x-measuring) efficiency was obtained by using special trigger (NIM1) which requires coincidence of y-hodoscope hits on all 4 stations. Reconstruction of tracks from NIM1 trigger was utilized to get the expected position of hit on X–hodoscopes. The efficiency of each paddle was calculated as the ratio of total hits recorded on the paddle to the total number of expected hits. For this analysis, the hits whose expected position lied in the overlap region between two x-measuring paddles or the overlap region between top and bottom hodoscopes were removed. This was done to eliminate events where the expected hit position lied on the overlap region but the actual hit was on one of the two adjacent paddles, which would result in underestimating the efficiency of the paddle which did not have the true recorded hit. The details of the analysis can be found in [48]. Unlike chamber efficiency, the hodoscope efficiency was not included in the tracking software. Hence, the acceptance calculation does not include this correction. Studies are underway to include the inefficiency of hodoscopes in the Monte Carlo.

4.7.5 Integrated luminosity

The target density and the attenuation factor depends on the composition of the target. The hydrogen target at SeaQuest was a pure sample hence it is straightforward to calculate these quantities for hydrogen target. The luminosity for hydrogen target can be written down as

$$\mathcal{L} = \frac{N_A(\rho_H L)\frac{\lambda_H}{L}(1 - e^{-L/\lambda_H})N_{incident(H)}}{A_H} = \frac{N_A T_H X_H N_H}{A_H}, \tag{4.15}$$

Using $\rho_H = 0.0708 g/cm^3$, $\lambda_H = 734.5 cm$ and $L = 50.8 cm$, T_H (thickness of H)=3.5966g/cm^2 and X_H(beam attenuation factor)=0.966. However, the deuterium target was contaminated by HD molecules for part of the data.(See table 4.7).

Target Contamination

Sample no.	D2 bottle no.		Sample date	description
1	Fermilab	53	4/12/18	95.6% D;4.4 %H, 92%D2; 8%HD
2	Fermilab	113	4/12/18	96% D;4 %H, 93%D2; 7%HD
3	Fermilab	53	4/12/18	just air; gas must have leaked
4	Matheson	127	4/12/18	about half air; remaining 99.7% D;0.3 %H
5	Matheson	2	4/12/18	sample for test purposes; not analyzed
6	Matheson		7/28/16	more than half air; remaining 99.3% D;0.7 %H
7	Matheson		5/28/17	99.8% D;0.2 %H; 99.6% D2;0.4%HD

Table 4.7: Summary of LD2 contamination

The proposed value to be used for roadset 57, 59, 62 and part of 67 is 91.8% D_2 and 8.2% HD. Remaining data (part of 67 and 70) is from pure LD_2 sample. Hence weighted average is used to calculate effective contamination fraction based on the number of protons with and without contaminated sample.

$$\mathcal{C} = \frac{\mathcal{C}_{contam.} \times \text{raw protons } LD_2(contam.)}{\text{total raw proton } LD_2} = 0.0595 \tag{4.16}$$

The volume of contaminated LD_2 relative to pure LD_2 is modified as $V_{LD_2}(contam.) = f \times V_{LD_2}(pure)$, where

$$\begin{aligned} f &= \text{fraction of } D_2 \times 1.0 + \text{fraction of } HD \times 1.094 \\ &= (1 - \mathcal{C}) + 1.094\mathcal{C}. \end{aligned} \tag{4.17}$$

The factor 1.094 in the above equation accounts for HD being 9.4% larger than D_2 molecule [49] Therefore the thickness of D in contaminated sample with HD contamination fraction $\mathcal{C}$ is

$$T_D^D = L\frac{\rho_D}{f}((1-\mathcal{C}) + \mathcal{C}/2) = L\frac{\rho_D}{f}(1-\mathcal{C}/2) \tag{4.18}$$

and the thickness of H in the sample is,

$$T_H^D = L\frac{\rho_D}{f}\mathcal{C}/2 = L\frac{\rho_D}{f}(\mathcal{C}/2) \tag{4.19}$$

Using $\rho_D = 0.1634 g/cm^3$, $\mathcal{C} = 0.0595$, T_D^D and T_H^D are calculated as $8.0092 g/cm^2$ and $0.24538 g/cm^2$. The attenuation factor X_D in contaminated deuterium is modified as

$$X_D = \frac{\lambda_{contam.}}{L}\left(1 - exp(-\frac{L}{\lambda_{contam.}})\right) = 0.943, \tag{4.20}$$

where $\lambda_{contam.}$ is derived as

$$\frac{1}{\lambda_{contam.}} = \frac{\text{% of H}}{\lambda_H} + \frac{\text{% of D}}{\lambda_D} = 432.4 cm. \tag{4.21}$$

The hydrogen and deuterium Drell-Yan yield can therefore be written as

$$\begin{aligned} Y_{LH_2} &= T_H^H N_A P_H X_H \sigma_{pp} \epsilon_H / A_H \\ Y_{LD_2} &= T_D^D N_A P_D X_D \sigma_{pd} \epsilon_D / A_D + T_D^H N_A P_D X_D \sigma_{pp} \epsilon_D / A_H \end{aligned} \tag{4.22}$$

The second term in Y_{LD_2} is the contribution coming from the H contamination inside the target. Therefore,

$$\begin{aligned} \sigma_{pp} &= \frac{Y_{LH_2}}{T_H^H N_A P_H X_H \epsilon_H / A_H} \\ \sigma_{pd} &= \frac{Y_{LD_2}}{T_D^D N_A P_D X_D \epsilon_D / A_D} - \frac{T_D^H}{T_D^D}\frac{A_D}{A_H}\sigma_{pp} \end{aligned} \tag{4.23}$$

N_A is the Avogadro's number (6.023e23), A_H and A_D are the atomic mass of hydrogen and deuterium, P_H and P_D are the number of incident proton(live) on hydrogen and deuterium target, and ϵ_H and ϵ_D includes acceptance and reconstruction efficiencies for hydrogen and deuterium. Therefore, the differential cross-section in scaling form is given by

$$
\begin{aligned}
M^3\frac{d^2\sigma_{pp}}{dMdx_F} &= M^3\frac{Y_{LH_2}(\Delta M,\Delta x_F)}{T_H^H N_A P_H X_H \epsilon_H/A_H}\frac{1}{\Delta M\Delta x_F} \\
M^3\frac{d^2\sigma_{pd}}{dMdx_F} &= M^3\frac{Y_{LD_2}(\Delta M,\Delta x_F)}{T_D^D N_A P_D X_D \epsilon_D/A_D}\frac{1}{\Delta M\Delta x_F} - \frac{T_D^H}{T_D^D}\frac{A_D}{A_H}M^3\frac{d^2\sigma_{pp}}{dMdx_F}
\end{aligned}
\tag{4.24}
$$

4.7.6 Systematic uncertainties

The sources of systematic uncertainty include

- Mixed background normalization

  Low statistics of mixed background sample possibly results in the mass-fit algorithm (using RooFit) to under estimate the amount of mixed background. An uncertainty of ±20% has been assigned to the normalization of mixed background. This uncertainty affects the mass bin up to 6 GeV. A study performed by Ching-Him Leung [50] used a different fitting algorithm (TFractionFitter) which resulted in 20% more mixed background.

- Proton beam normalization

  As described in section 2.1.2, the QIE module attached to the beam intensity monitor (BIM) measures the intensity of the beam. The QIE measurement is converted to the live proton using the calibrated SEM monitor (G2SEM). The SEM response was calibrated by studying the rate of 1368 keV γs emitted by the produced ^{24}Na using Cu foil activation method. The estimated random uncertainty ($\sim$ 1-2 %) in the calibration takes into account the uncertainty arising from the counting statistics and the extraction of 1368 keV ^{24}Na ground state decay to 4^+ excited state of ^{24}Mg. Additionally an ±8% systematic uncertainty is estimated to arise from the uncertainty in the production cross section of ^{24}Na from the irradiation of copper foil by 120 GeV proton beam. [51, 52].

The systematic uncertainty contributions are added in quadrature. For example, the lower bound estimate of mix background and beam normalization would contribute to upper (+) systematic uncertainty.

$$
\begin{aligned}
(\Delta\sigma_{syst.(+)})^2 &= (\Delta\sigma_{mixbkg.(-)})^2 + (\Delta\sigma_{beamnorm.(-)})^2 \\
(\Delta\sigma_{syst.(-)})^2 &= (\Delta\sigma_{mixbkg.(+)})^2 + (\Delta\sigma_{beamnorm.(+)})^2
\end{aligned}
\tag{4.25}
$$

4.8 NLO theory calculation

The NLO theory calculation is performed using the parton level Monte Carlo code developed by INFN group [40, 41]. This program is originally written to compute cross-section for vector boson production from

$p + p$ and $p + \bar{p}$ collisions. It was modified by Wen-Chen Chang, Ching-Him Leung and Shivangi Prasad to perform $p + n$ calculation therefore one can obtain $p + d$ cross-section by summing up $p + p$ and $p + n$ results. Additionally, the definition of x_F was modified to be consistent with SeaQuest's definition of x_F.

$$x'_F = \frac{x_F}{1 - \frac{M^2}{s}} \tag{4.26}$$

The calculations were performed upto next-to-leading order (NLO). For NLO corrections, two kinds of diagrams contribute, (i) gluons emission of a parton, (ii) loop diagram contributions in interference term. Both these contributions are separately IR divergent, but the divergences cancel out in the sum[40, 41]. The program requires $\sqrt{s}$, Order (LO, NLO etc.), PDF name, mass range, process ID, beam and target particle ID as input. The program outputs 1-D histograms in several kinematic quantities. For the purpose of comparison with scaling-form cross-section, $d\sigma/dM$ is required. For each x_F bin, the $d\sigma_{pp}/dM$ and $d\sigma_{pn}/dM$ histogram is calculated. For the case of deuterium, p+p and p+n histograms are added in each mass bin and there corresponding errors are added in quadrature. To get the scaling form of cross-section, each bin is multiplied by M^3 where M is the bin centre and also divided by Δx_F i.e., the x_F bin-width (which is equal to 0.05 for the calculations shown in this thesis). Additionally, a factor of 1e-6 is multiplied to convert the cross-section from femtobarn (fb) to nanobarn(nb). The error band calculation was performed by Ching-Hum Leung. NLO code was run for each member of the chosen PDF in each x_F bin. In case of CT14NLO[53] and NNPDF30 NLO[29] there are 57 and 107 members, respectively. The error band in each mass bin is the maximum (upper bound) and minimum (lower bound) of the cross-section obtained from all the PDF members.

variable	setting
sroot	15.01
ih1, ih2	1,1(for p+p);1,2(p+n)
nproc	3 ($Z/\gamma* \rightarrow \mu^-\mu^+$)
mur, muf	6.0,6.0 (factorization and renormalization scale)
order	1 (NLO)
part	'tota' (for complete calcultion, real+virtual)
mwmin,mwmax	4.0,9.0
itmx1, ncall1	15,1000000
itmx2, ncall2	30,1000000
rseed	30
set, member	CT14nlo, 0(for central value) member no. (for error band)
xFcut	.true.
xFmin	xF bin low
xFmax	xF bin high

Table 4.8: List of variables and their settings for NLO calculation

Chapter 5

SeaQuest Results

5.1 Absolute cross section results

This section consists of tables and plots showing absolute Drell-Yan cross section (scaling form $M^3d^2/\sigma/dMdx_F$) for Deuterium and Hydrogen data from SeaQuest/E906. The results are presented as a function of mass in range 4.2 GeV to 8.7 GeV in x_F bins ranging from 0 to 0.8.

5.1.1 Deuterium absolute cross section

Mass bin (GeV)	$M^3d^2\sigma/dMdx_F(\times10^{-1})$	Stat. error$(\times10^{-1})$	Syst. err(-)$(\times10^{-1})$	Syst. err(+)$(\times10^{-1})$
4.50-4.80	6.981630	21.029500	5.645100	6.479820
4.80-5.10	8.469470	4.128100	1.881600	0.967758
5.10-5.40	3.796700	2.412110	0.919370	0.713182
5.40-5.70	2.979740	1.094640	0.564971	0.326210
5.70-6.00	2.172180	0.637578	0.321968	0.165598
6.00-6.30	1.878820	0.577268	0.300901	0.169372
6.30-6.60	1.743900	0.362662	0.241713	0.128480
6.60-6.90	0.669427	0.207319	0.114798	0.045106
6.90-7.20	0.832782	0.254222	0.124520	0.058104
7.20-7.50	0.750034	0.274599	0.097649	0.058388
7.50-7.80	0.117855	0.126358	0.023396	0.008710
7.80-8.10	-0.006599	0.006625	0.009332	0.009332
8.10-8.40	0.000000	0.000000	0.000000	0.000000
8.40-8.70	0.000000	0.000000	0.000000	0.000000

Table 5.1: Deuterium Drell-Yan scaling form cross section $M^3d^2\sigma/dMdx_F$ (GeV^2nb) for $0.0 < x_F < 0.05$ bin. Statistical and systematic error are also shown in the respective columns.

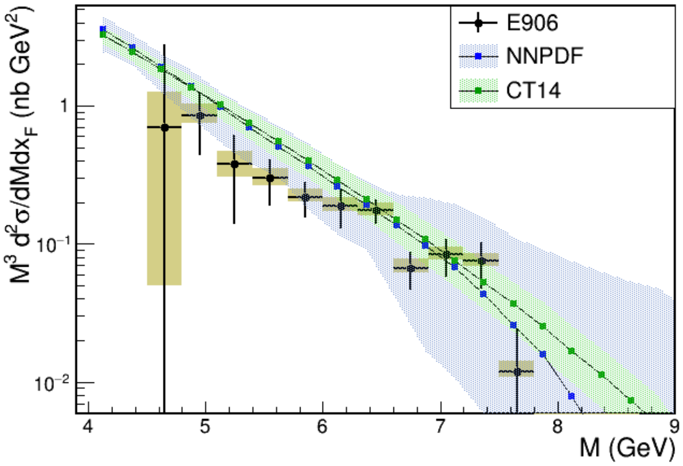

Figure 5.1: p+d absolute Drell-Yan cross section measurement in $x_F = [0.0, 0.05)$

Mass bin (GeV)	$M^3d^2\sigma/dMdx_F(\times 10^{-1})$	Stat. error$(\times 10^{-1})$	Syst. err(-)$(\times 10^{-1})$	Syst. err(+)$(\times 10^{-1})$
4.50-4.80	3.443820	10.813400	3.972070	3.589540
4.80-5.10	7.500030	2.386270	1.818010	0.978490
5.10-5.40	6.530890	1.253780	1.064250	0.456672
5.40-5.70	5.396090	0.839860	0.788197	0.374682
5.70-6.00	3.408610	0.661027	0.469841	0.270061
6.00-6.30	1.706820	0.367789	0.282820	0.099183
6.30-6.60	1.864610	0.311974	0.250431	0.141118
6.60-6.90	1.114220	0.233166	0.143045	0.087882
6.90-7.20	0.333038	0.276485	0.064875	0.046357
7.20-7.50	0.325292	0.150757	0.046568	0.023367
7.50-7.80	0.381444	0.201633	0.064572	0.025667
7.80-8.10	0.217261	0.166724	0.046110	0.017452
8.10-8.40	0.000000	0.000000	0.000000	0.000000
8.40-8.70	0.000000	0.000000	0.000000	0.000000

Table 5.2: Deuterium Drell-Yan scaling form cross section $M^3d^2\sigma/dMdx_F$ (GeV^2nb) for $0.05 < x_F < 0.1$ bin. Statistical and systematic error are also shown in the respective columns.

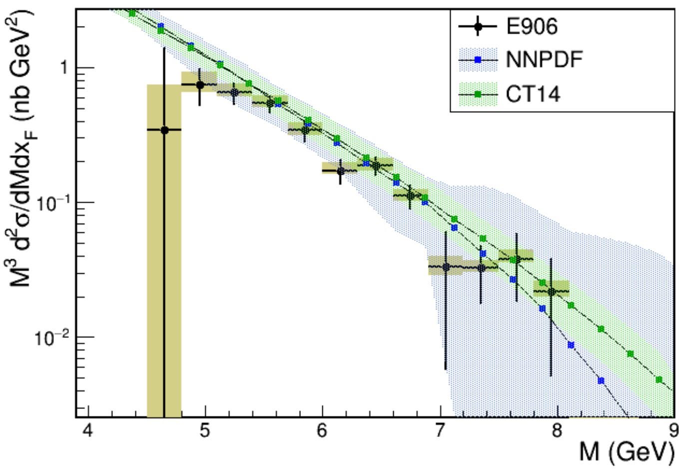

Figure 5.2: p+d absolute Drell-Yan cross section measurement in $x_F = [0.05, 0.1)$

Mass bin (GeV)	$M^3d^2\sigma/dMdx_F(\times 10^{-1})$	Stat. error$(\times 10^{-1})$	Syst. err(-)$(\times 10^{-1})$	Syst. err(+)$(\times 10^{-1})$
4.50-4.80	8.148940	4.118380	2.947340	2.352450
4.80-5.10	9.401260	1.977410	1.782850	1.054710
5.10-5.40	7.410540	1.105090	1.178680	0.581015
5.40-5.70	3.729020	0.711054	0.616052	0.352300
5.70-6.00	2.359510	0.530481	0.410399	0.186288
6.00-6.30	2.512210	0.342960	0.388923	0.162203
6.30-6.60	1.223720	0.281131	0.182256	0.082056
6.60-6.90	1.688640	0.272056	0.226370	0.128013
6.90-7.20	0.775320	0.190602	0.106397	0.057597
7.20-7.50	0.414149	0.151742	0.058246	0.030156
7.50-7.80	-0.008720	0.004389	0.012332	0.012332
7.80-8.10	0.079242	0.085332	0.016350	0.006130
8.10-8.40	0.283884	0.208679	0.042447	0.019807
8.40-8.70	0.000000	0.000000	0.000000	0.000000

Table 5.3: Deuterium Drell-Yan scaling form cross section $M^3d^2\sigma/dMdx_F$ (GeV^2nb) for $0.1 < x_F < 0.15$ bin. Statistical and systematic error are also shown in the respective columns.

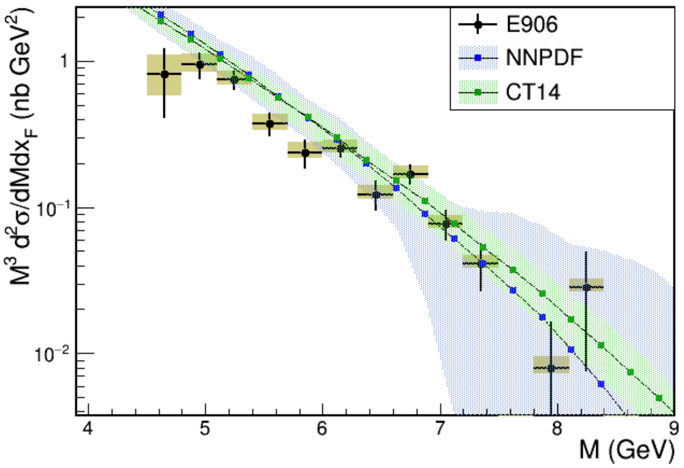

Figure 5.3: p+d absolute Drell-Yan cross section measurement in $x_F = [0.1, 0.15)$

Mass bin (GeV)	$M^3d^2\sigma/dMdx_F(\times10^{-1})$	Stat. error$(\times10^{-1})$	Syst. err(-)$(\times10^{-1})$	Syst. err(+)$(\times10^{-1})$
4.50-4.80	14.256800	2.548230	2.601890	1.290640
4.80-5.10	10.803100	1.262550	1.745920	0.666489
5.10-5.40	7.895290	0.861893	1.243790	0.499019
5.40-5.70	4.885780	0.615830	0.730210	0.345509
5.70-6.00	3.150490	0.432706	0.497097	0.201732
6.00-6.30	2.066170	0.346122	0.303426	0.140223
6.30-6.60	1.795420	0.266748	0.251647	0.131087
6.60-6.90	1.143970	0.203887	0.155552	0.085652
6.90-7.20	0.551947	0.181500	0.090457	0.037186
7.20-7.50	0.202207	0.169812	0.030842	0.013954
7.50-7.80	0.451037	0.163141	0.056857	0.036198
7.80-8.10	0.078792	0.081407	0.011720	0.005515
8.10-8.40	0.104492	0.104701	0.011610	0.009499
8.40-8.70	0.000000	0.000000	0.000000	0.000000

Table 5.4: Deuterium Drell-Yan scaling form cross section $M^3d^2\sigma/dMdx_F$ (GeV^2nb) for $0.15 < x_F < 0.2$ bin. Statistical and systematic error are also shown in the respective columns.

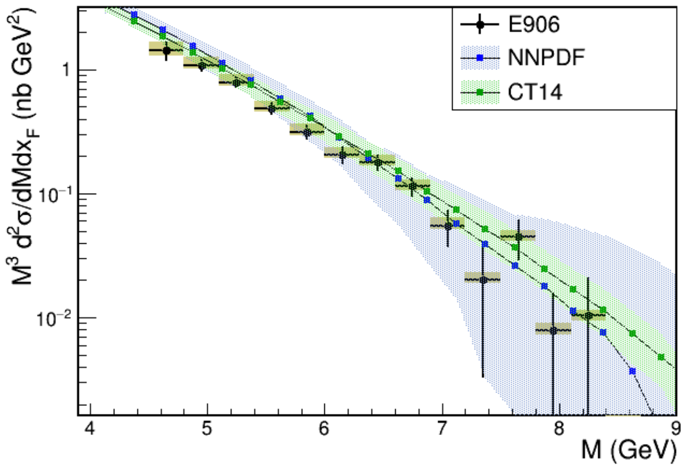

Figure 5.4: p+d absolute Drell-Yan cross section measurement in $x_F = [0.15, 0.2)$

Mass bin (GeV)	$M^3d^2\sigma/dMdx_F(\times10^{-1})$	Stat. error$(\times10^{-1})$	Syst. err(-)$(\times10^{-1})$	Syst. err(+)$(\times10^{-1})$
4.50-4.80	14.613000	2.040810	2.336120	1.506720
4.80-5.10	9.928910	1.149570	1.618620	0.789370
5.10-5.40	7.453230	0.760436	1.107360	0.536569
5.40-5.70	5.027120	0.516373	0.735864	0.345279
5.70-6.00	3.057280	0.409108	0.461974	0.215135
6.00-6.30	2.616430	0.303814	0.352523	0.197466
6.30-6.60	1.548610	0.216608	0.231501	0.108063
6.60-6.90	0.596618	0.144817	0.090971	0.041178
6.90-7.20	0.622141	0.141942	0.089412	0.044563
7.20-7.50	0.338635	0.155707	0.038128	0.030380
7.50-7.80	0.180351	0.097171	0.036607	0.013671
7.80-8.10	0.139775	0.100467	0.017640	0.011205
8.10-8.40	0.000000	0.000000	0.000000	0.000000
8.40-8.70	-0.004113	0.004123	0.005817	0.005817

Table 5.5: Deuterium Drell-Yan scaling form cross section $M^3d^2\sigma/dMdx_F$ (GeV^2nb) for $0.2 < x_F < 0.25$ bin. Statistical and systematic error are also shown in the respective columns.

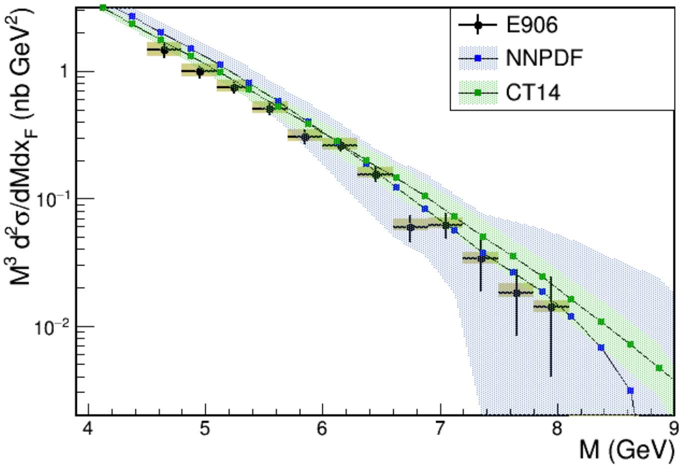

Figure 5.5: p+d absolute Drell-Yan cross section measurement in $x_F = [0.2, 0.25)$

Mass bin (GeV)	$M^3d^2\sigma/dMdx_F(\times10^{-1})$	Stat. error$(\times10^{-1})$	Syst. err(-)$(\times10^{-1})$	Syst. err(+)$(\times10^{-1})$
4.50-4.80	12.833900	1.424580	2.230010	1.049460
4.80-5.10	9.069020	0.860092	1.380850	0.649653
5.10-5.40	6.380560	0.576810	0.961338	0.425091
5.40-5.70	4.601670	0.438541	0.671629	0.313771
5.70-6.00	3.337990	0.289372	0.496995	0.233488
6.00-6.30	2.302090	0.258824	0.333007	0.159940
6.30-6.60	1.418580	0.203797	0.198848	0.103565
6.60-6.90	0.674957	0.199071	0.109121	0.041675
6.90-7.20	0.755658	0.146970	0.107505	0.054536
7.20-7.50	0.585872	0.138340	0.074548	0.046601
7.50-7.80	0.238431	0.099016	0.029485	0.019493
7.80-8.10	0.056041	0.056105	0.006227	0.005095
8.10-8.40	0.000000	0.000000	0.000000	0.000000
8.40-8.70	0.000000	0.000000	0.000000	0.000000

Table 5.6: Deuterium Drell-Yan scaling form cross section $M^3d^2\sigma/dMdx_F$ (GeV^2nb) for $0.25 < x_F < 0.3$ bin. Statistical and systematic error are also shown in the respective columns.

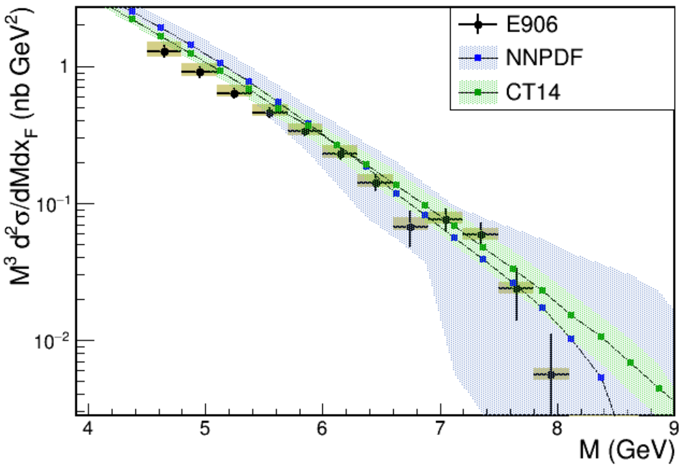

Figure 5.6: p+d absolute Drell-Yan cross section measurement in $x_F = [0.25, 0.3)$

Mass bin (GeV)	$M^3d^2\sigma/dMdx_F(\times10^{-1})$	Stat. error$(\times10^{-1})$	Syst. err(-)$(\times10^{-1})$	Syst. err(+)$(\times10^{-1})$
4.50-4.80	13.109200	1.149120	1.973460	0.929509
4.80-5.10	9.353010	0.758214	1.421380	0.641271
5.10-5.40	5.786790	0.471191	0.877552	0.376938
5.40-5.70	4.024580	0.382738	0.608252	0.263445
5.70-6.00	3.268790	0.314715	0.453884	0.237468
6.00-6.30	2.153780	0.234741	0.313102	0.148997
6.30-6.60	1.593330	0.202644	0.225343	0.115513
6.60-6.90	1.059040	0.161117	0.158719	0.073789
6.90-7.20	0.473227	0.133559	0.066389	0.034526
7.20-7.50	0.317486	0.132835	0.037267	0.027324
7.50-7.80	0.275755	0.149961	0.034674	0.022184
7.80-8.10	0.125477	0.076587	0.022342	0.008542
8.10-8.40	0.182039	0.109284	0.028058	0.012498
8.40-8.70	0.097122	0.097291	0.010791	0.008829

Table 5.7: Deuterium Drell-Yan scaling form cross section $M^3d^2\sigma/dMdx_F$ (GeV^2nb) for $0.3 < x_F < 0.35$ bin. Statistical and systematic error are also shown in the respective columns.

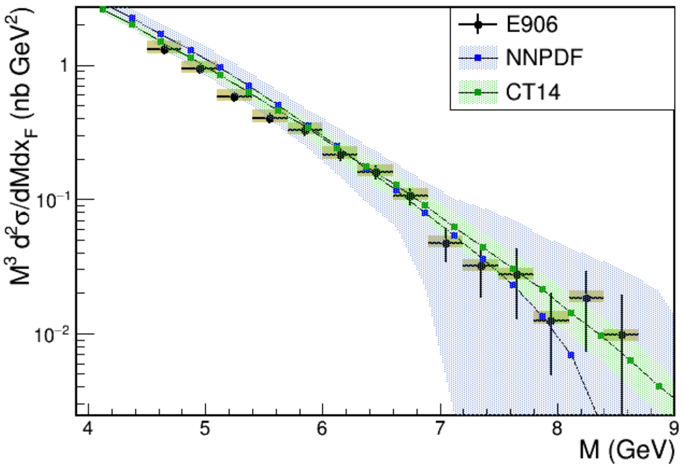

Figure 5.7: p+d absolute Drell-Yan cross section measurement in $x_F = [0.3, 0.35)$

Mass bin (GeV)	$M^3d^2\sigma/dMdx_F(\times 10^{-1})$	Stat. error$(\times 10^{-1})$	Syst. err(-)$(\times 10^{-1})$	Syst. err(+)$(\times 10^{-1})$
4.50-4.80	11.222300	0.888990	1.757090	0.773069
4.80-5.10	9.554130	0.676913	1.363180	0.673738
5.10-5.40	6.461790	0.445358	0.949548	0.443987
5.40-5.70	3.587320	0.314927	0.499415	0.258065
5.70-6.00	2.736480	0.254792	0.400135	0.189523
6.00-6.30	1.846420	0.200720	0.263223	0.133052
6.30-6.60	1.259450	0.184697	0.179919	0.090613
6.60-6.90	0.968037	0.141874	0.137057	0.070122
6.90-7.20	0.461695	0.100452	0.067696	0.032612
7.20-7.50	0.513777	0.121965	0.070488	0.038176
7.50-7.80	0.368536	0.111049	0.056487	0.025370
7.80-8.10	0.087097	0.064399	0.014359	0.005864
8.10-8.40	0.113105	0.081454	0.014686	0.008827
8.40-8.70	-0.002512	0.002515	0.003552	0.003552

Table 5.8: Deuterium Drell-Yan scaling form cross section $M^3d^2\sigma/dMdx_F$ (GeV^2nb) for $0.35 < x_F < 0.4$ bin. Statistical and systematic error are also shown in the respective columns.

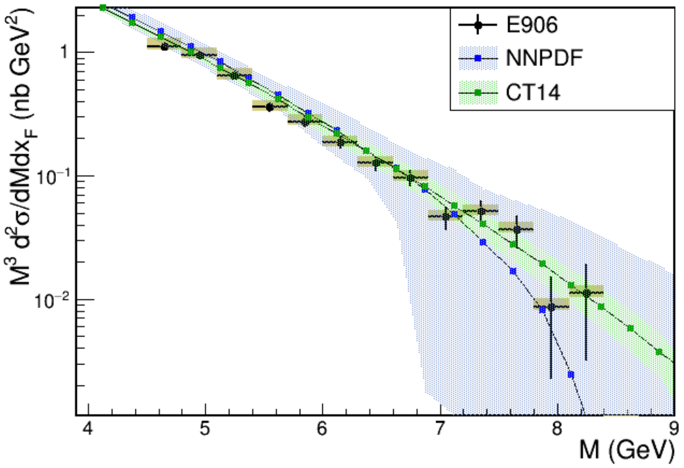

Figure 5.8: p+d absolute Drell-Yan cross section measurement in $x_F = [0.35, 0.4)$

Mass bin (GeV)	$M^3 d^2\sigma/dMdx_F(\times 10^{-1})$	Stat. error$(\times 10^{-1})$	Syst. err(-)$(\times 10^{-1})$	Syst. err(+)$(\times 10^{-1})$
4.50-4.80	10.638900	0.704015	1.609040	0.695027
4.80-5.10	7.983320	0.547969	1.206930	0.521560
5.10-5.40	5.246620	0.372582	0.755911	0.366467
5.40-5.70	3.814650	0.312167	0.552637	0.263393
5.70-6.00	2.774400	0.264613	0.377381	0.204742
6.00-6.30	1.817150	0.208020	0.278669	0.119891
6.30-6.60	1.377800	0.165198	0.201448	0.097507
6.60-6.90	0.754537	0.141176	0.104935	0.055437
6.90-7.20	0.353849	0.123757	0.045349	0.027955
7.20-7.50	0.359050	0.120580	0.047786	0.027395
7.50-7.80	0.115598	0.059850	0.017312	0.008058
7.80-8.10	0.031045	0.114122	0.002441	0.005360
8.10-8.40	-0.003027	0.002144	0.004281	0.004281
8.40-8.70	0.070176	0.070262	0.007797	0.006380

Table 5.9: Deuterium Drell-Yan scaling form cross section $M^3 d^2\sigma/dMdx_F$ $(GeV^2 nb)$ for $0.4 < x_F < 0.45$ bin. Statistical and systematic error are also shown in the respective columns.

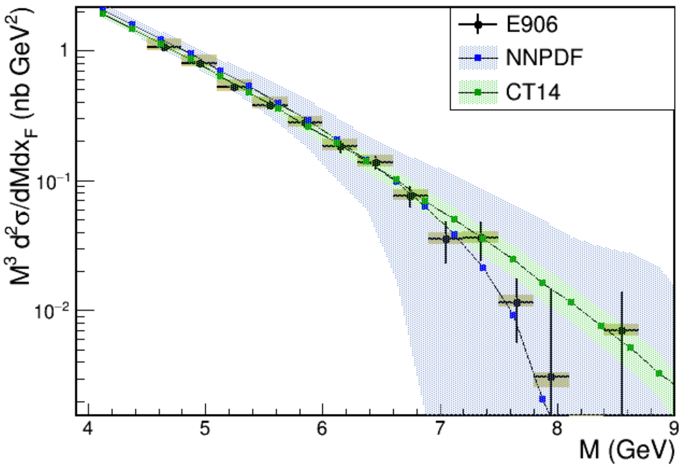

Figure 5.9: p+d absolute Drell-Yan cross section measurement in $x_F = [0.4, 0.45)$

Mass bin (GeV)	$M^3d^2\sigma/dMdx_F(\times10^{-1})$	Stat. error($\times10^{-1}$)	Syst. err(-)($\times10^{-1}$)	Syst. err(+)($\times10^{-1}$)
4.50-4.80	9.653780	0.648818	1.441630	0.649382
4.80-5.10	6.547850	0.415911	0.967275	0.442238
5.10-5.40	4.799760	0.343633	0.662839	0.348554
5.40-5.70	2.963270	0.261030	0.431269	0.202562
5.70-6.00	2.345380	0.201434	0.330750	0.170415
6.00-6.30	1.640920	0.176018	0.221838	0.123477
6.30-6.60	1.188460	0.146243	0.168498	0.085996
6.60-6.90	0.547846	0.111213	0.073965	0.041273
6.90-7.20	0.575059	0.108145	0.084583	0.040536
7.20-7.50	0.307998	0.086352	0.049329	0.020848
7.50-7.80	0.143668	0.067031	0.022894	0.009739
7.80-8.10	0.136669	0.070267	0.019165	0.009975
8.10-8.40	0.139864	0.082652	0.018886	0.010536
8.40-8.70	0.000000	0.000000	0.000000	0.000000

Table 5.10: Deuterium Drell-Yan scaling form cross section $M^3d^2\sigma/dMdx_F$ (GeV^2nb) for $0.45 < x_F < 0.5$ bin. Statistical and systematic error are also shown in the respective columns.

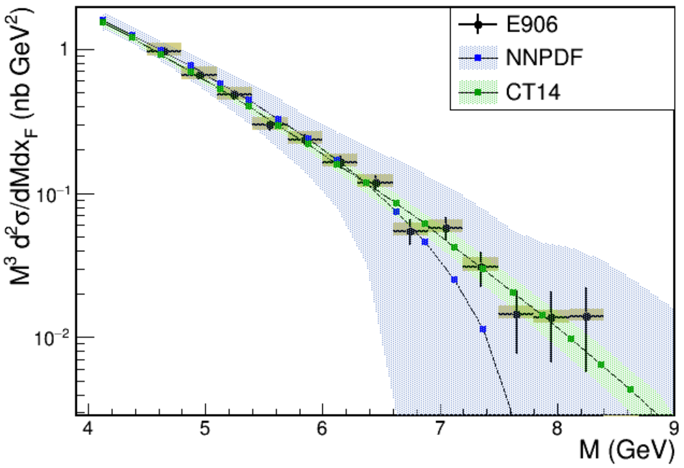

Figure 5.10: p+d absolute Drell-Yan cross section measurement in $x_F = [0.45, 0.5)$

Mass bin (GeV)	$M^3d^2\sigma/dMdx_F(\times 10^{-1})$	Stat. error$(\times 10^{-1})$	Syst. err(-)$(\times 10^{-1})$	Syst. err(+)$(\times 10^{-1})$
4.50-4.80	8.061030	0.529713	1.124740	0.580037
4.80-5.10	5.132000	0.331645	0.730985	0.365221
5.10-5.40	3.516390	0.268716	0.523406	0.235650
5.40-5.70	2.375990	0.215388	0.348266	0.162761
5.70-6.00	1.670830	0.183768	0.232404	0.120767
6.00-6.30	1.395110	0.157982	0.188091	0.105231
6.30-6.60	0.718617	0.114704	0.107841	0.050032
6.60-6.90	0.767950	0.116245	0.097774	0.061049
6.90-7.20	0.433715	0.093191	0.057164	0.033384
7.20-7.50	0.337953	0.089629	0.044600	0.025983
7.50-7.80	0.124972	0.059034	0.022142	0.008491
7.80-8.10	0.172587	0.078953	0.022949	0.013179
8.10-8.40	0.039928	0.042496	0.007630	0.002843
8.40-8.70	0.111459	0.080350	0.014637	0.008608

Table 5.11: Deuterium Drell-Yan scaling form cross section $M^3d^2\sigma/dMdx_F$ (GeV^2nb) for $0.5 < x_F < 0.55$ bin. Statistical and systematic error are also shown in the respective columns.

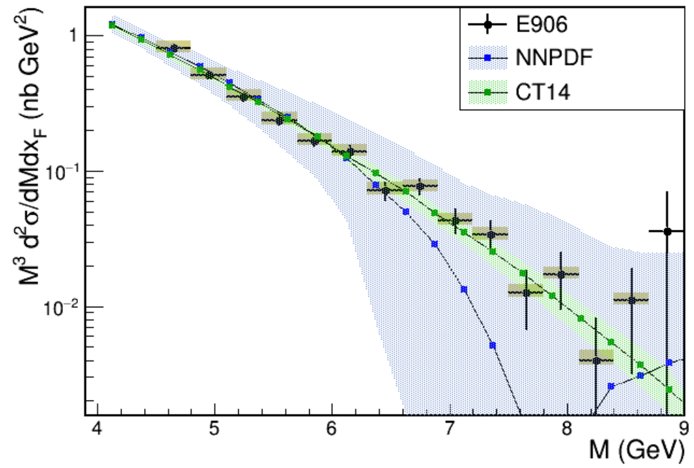

Figure 5.11: p+d absolute Drell-Yan cross section measurement in $x_F = [0.5, 0.55)$

Mass bin (GeV)	$M^3d^2\sigma/dMdx_F(\times10^{-1})$	Stat. error$(\times10^{-1})$	Syst. err(-)$(\times10^{-1})$	Syst. err(+)$(\times10^{-1})$
4.50-4.80	5.102610	0.375346	0.799865	0.318574
4.80-5.10	4.468730	0.303053	0.616293	0.325795
5.10-5.40	2.564620	0.220668	0.389129	0.167328
5.40-5.70	2.075650	0.171809	0.292195	0.151026
5.70-6.00	1.102600	0.156854	0.158541	0.076590
6.00-6.30	0.922566	0.143240	0.124812	0.069378
6.30-6.60	0.598144	0.101774	0.085581	0.042985
6.60-6.90	0.483784	0.092035	0.068780	0.034933
6.90-7.20	0.350973	0.081189	0.048919	0.025740
7.20-7.50	0.148791	0.058872	0.024190	0.010037
7.50-7.80	0.169350	0.065182	0.021479	0.013511
7.80-8.10	0.061771	0.044406	0.007953	0.004859
8.10-8.40	0.036234	0.037559	0.005590	0.002487
8.40-8.70	-0.003250	0.002303	0.004596	0.004596

Table 5.12: Deuterium Drell-Yan scaling form cross section $M^3d^2\sigma/dMdx_F$ (GeV^2nb) for $0.55 < x_F < 0.6$ bin. Statistical and systematic error are also shown in the respective columns.

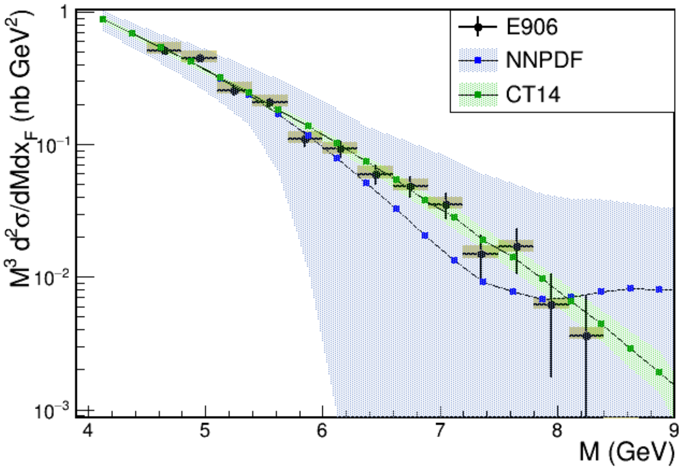

Figure 5.12: p+d absolute Drell-Yan cross section measurement in $x_F = [0.55, 0.6)$

Mass bin (GeV)	$M^3d^2\sigma/dMdx_F(\times10^{-1})$	Stat. error$(\times10^{-1})$	Syst. err(-)$(\times10^{-1})$	Syst. err(+)$(\times10^{-1})$
4.50-4.80	4.745350	0.327720	0.664606	0.339056
4.80-5.10	2.587740	0.204594	0.380556	0.177361
5.10-5.40	2.025360	0.169657	0.286132	0.146958
5.40-5.70	1.330700	0.132961	0.190636	0.095539
5.70-6.00	0.940483	0.122042	0.135802	0.067137
6.00-6.30	0.775924	0.114262	0.107003	0.057406
6.30-6.60	0.511816	0.085808	0.073361	0.036732
6.60-6.90	0.362222	0.087886	0.051803	0.026039
6.90-7.20	0.132603	0.048958	0.021151	0.008986
7.20-7.50	0.124017	0.052139	0.017546	0.008988
7.50-7.80	0.046598	0.035172	0.009080	0.003378
7.80-8.10	0.057957	0.041671	0.007474	0.004552
8.10-8.40	0.108811	0.062976	0.012090	0.009892
8.40-8.70	0.050495	0.052314	0.007745	0.003475

Table 5.13: Deuterium Drell-Yan scaling form cross section $M^3d^2\sigma/dMdx_F$ (GeV^2nb) for $0.6 < x_F < 0.65$ bin. Statistical and systematic error are also shown in the respective columns.

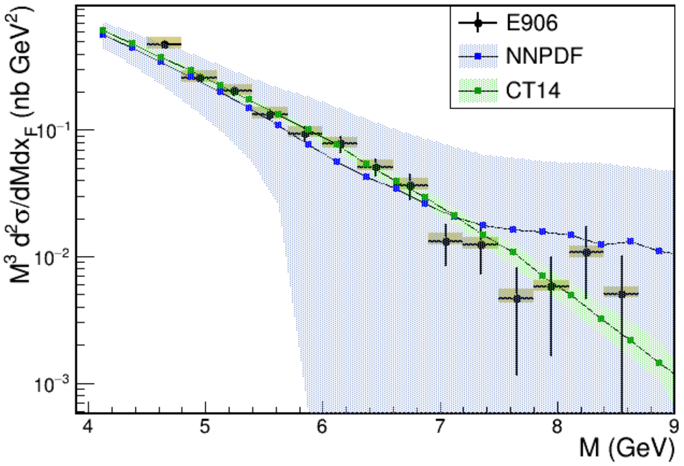

Figure 5.13: p+d absolute Drell-Yan cross section measurement in $x_F = [0.6, 0.65)$

Mass bin (GeV)	$M^3d^2\sigma/dMdx_F(\times10^{-1})$	Stat. error($\times10^{-1}$)	Syst. err(-)($\times10^{-1}$)	Syst. err(+)($\times10^{-1}$)
4.50-4.80	2.633900	0.214143	0.389845	0.177071
4.80-5.10	1.913380	0.176877	0.268825	0.136434
5.10-5.40	1.188750	0.126864	0.185984	0.081094
5.40-5.70	1.051250	0.112181	0.156003	0.073683
5.70-6.00	0.678980	0.099614	0.092745	0.050639
6.00-6.30	0.371705	0.083415	0.057021	0.025578
6.30-6.60	0.229882	0.071712	0.035420	0.015786
6.60-6.90	0.198536	0.057036	0.028795	0.014129
6.90-7.20	0.058161	0.033387	0.017759	0.008613
7.20-7.50	0.081935	0.042332	0.012099	0.005761
7.50-7.80	0.138990	0.058498	0.019885	0.009989
7.80-8.10	0.031426	0.031445	0.003492	0.002857
8.10-8.40	0.049122	0.049163	0.005458	0.004466
8.40-8.70	0.000000	0.000000	0.000000	0.000000

Table 5.14: Deuterium Drell-Yan scaling form cross section $M^3d^2\sigma/dMdx_F$ (GeV^2nb) for $0.65 < x_F < 0.7$ bin. Statistical and systematic error are also shown in the respective columns.

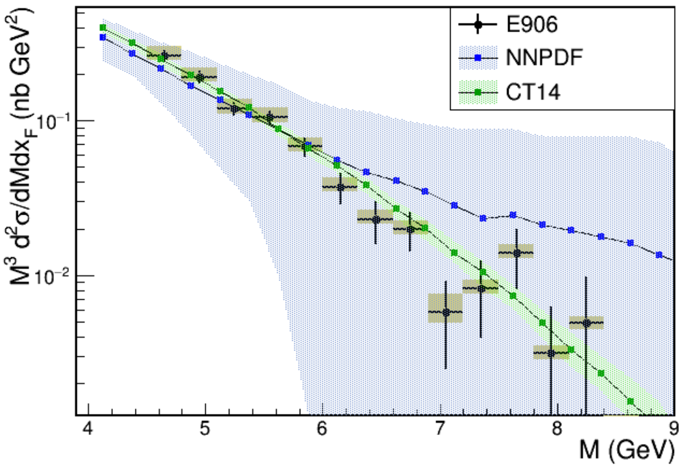

Figure 5.14: p+d absolute Drell-Yan cross section measurement in $x_F = [0.65, 0.7)$

Mass bin (GeV)	$M^3d^2\sigma/dMdx_F(\times10^{-1})$	Stat. error$(\times10^{-1})$	Syst. err(-)$(\times10^{-1})$	Syst. err(+)$(\times10^{-1})$
4.50-4.80	1.637320	0.170258	0.248101	0.106626
4.80-5.10	1.190920	0.134728	0.172774	0.082625
5.10-5.40	0.799661	0.093516	0.112390	0.058258
5.40-5.70	0.607620	0.084819	0.085535	0.044211
5.70-6.00	0.436197	0.072154	0.061328	0.031769
6.00-6.30	0.212258	0.052910	0.035930	0.014282
6.30-6.60	0.111894	0.054338	0.022534	0.008403
6.60-6.90	0.072894	0.054740	0.010138	0.005355
6.90-7.20	0.049863	0.029177	0.006165	0.004077
7.20-7.50	0.068319	0.040261	0.009099	0.005209
7.50-7.80	0.028912	0.029960	0.004452	0.001986
7.80-8.10	0.063265	0.044849	0.007029	0.005751
8.10-8.40	-0.000354	0.000355	0.000500	0.000500
8.40-8.70	0.000000	0.000000	0.000000	0.000000

Table 5.15: Deuterium Drell-Yan scaling form cross section $M^3d^2\sigma/dMdx_F$ (GeV^2nb) for $0.7 < x_F < 0.75$ bin. Statistical and systematic error are also shown in the respective columns.

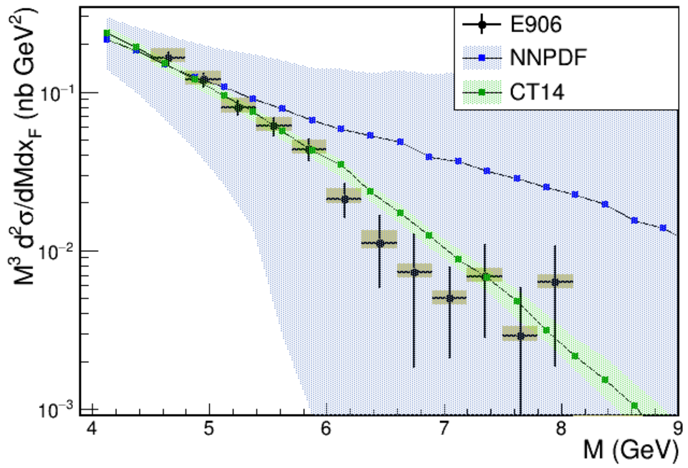

Figure 5.15: p+d absolute Drell-Yan cross section measurement in $x_F = [0.7, 0.75)$

Mass bin (GeV)	$M^3d^2\sigma/dMdx_F(\times 10^{-1})$	Stat. error$(\times 10^{-1})$	Syst. err(-)$(\times 10^{-1})$	Syst. err(+)$(\times 10^{-1})$
4.50-4.80	0.810564	0.121057	0.110761	0.059513
4.80-5.10	0.642336	0.097489	0.088905	0.046501
5.10-5.40	0.595968	0.081022	0.081301	0.044497
5.40-5.70	0.378078	0.070492	0.050674	0.028666
5.70-6.00	0.234967	0.052291	0.034916	0.016455
6.00-6.30	0.167463	0.046776	0.026090	0.011443
6.30-6.60	0.139475	0.045053	0.017992	0.010951
6.60-6.90	0.111844	0.046802	0.015186	0.008385
6.90-7.20	0.035692	0.026669	0.006407	0.002438
7.20-7.50	-0.000886	0.000629	0.001253	0.001253
7.50-7.80	0.002265	0.001173	0.000252	0.000206
7.80-8.10	0.000000	0.000000	0.000000	0.000000
8.10-8.40	0.000000	0.000000	0.000000	0.000000
8.40-8.70	0.000000	0.000000	0.000000	0.000000

Table 5.16: Deuterium Drell-Yan scaling form cross section $M^3d^2\sigma/dMdx_F$ (GeV^2nb) for $0.75 < x_F < 0.8$ bin. Statistical and systematic error are also shown in the respective columns.

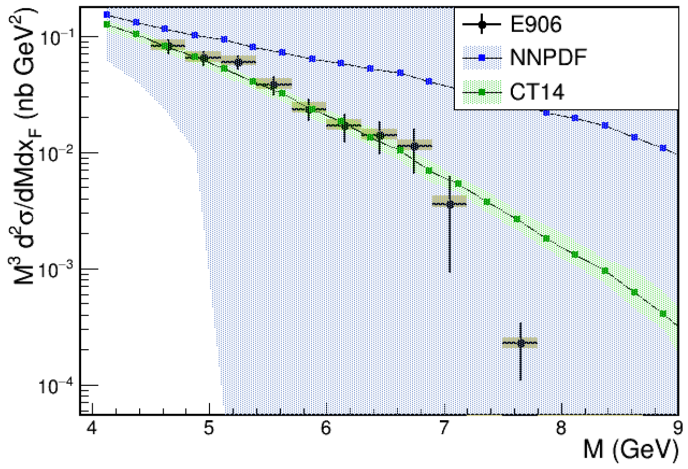

Figure 5.16: p+d absolute Drell-Yan cross section measurement in $x_F = [0.75, 0.8)$

5.1.2 Hydrogen absolute cross section

Mass bin (GeV)	$M^3d^2\sigma/dMdx_F(\times 10^{-1})$	Stat. error$(\times 10^{-1})$	Syst. err(-)$(\times 10^{-1})$	Syst. err(+)$(\times 10^{-1})$
4.50-4.80	-6.290930	20.735400	19.083400	11.224700
4.80-5.10	4.690440	3.335370	6.794290	4.498380
5.10-5.40	1.019910	1.113430	4.146170	3.295380
5.40-5.70	1.135140	0.716161	2.300470	1.709100
5.70-6.00	0.719076	0.449569	1.336830	1.044610
6.00-6.30	0.585446	0.334332	0.495076	0.274477
6.30-6.60	0.655616	0.218294	0.280498	0.166632
6.60-6.90	0.526382	0.135237	0.056848	0.049232
6.90-7.20	0.429114	0.126509	0.046343	0.040135
7.20-7.50	0.199181	0.100493	0.021511	0.018629
7.50-7.80	0.130714	0.092974	0.014117	0.012226
7.80-8.10	0.107804	0.108230	0.011643	0.010083
8.10-8.40	0.000000	0.000000	0.000000	0.000000
8.40-8.70	0.000000	0.000000	0.000000	0.000000

Table 5.17: Hydrogen Drell-Yan scaling form cross section $M^3d^2\sigma/dMdx_F$ (GeV^2nb) for $0.0 < x_F < 0.05$ bin. Statistical and systematic error are also shown in the respective columns.

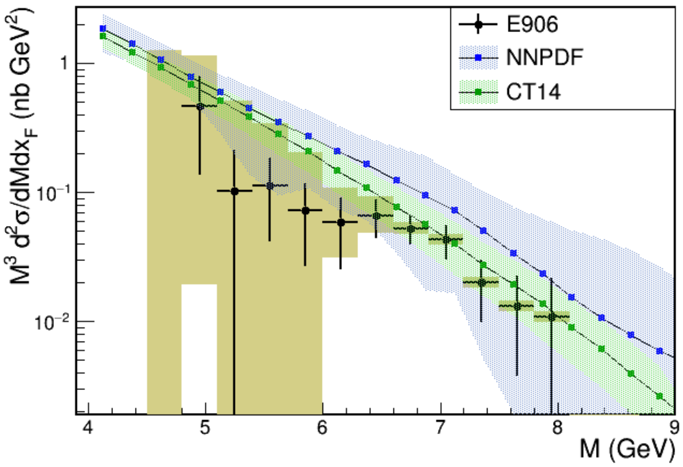

Figure 5.17: p+p absolute Drell-Yan cross section measurement in $x_F = [0.0, 0.05)$

Mass bin (GeV)	$M^3d^2\sigma/dMdx_F(\times10^{-1})$	Stat. error$(\times10^{-1})$	Syst. err(-)$(\times10^{-1})$	Syst. err(+)$(\times10^{-1})$
4.50-4.80	2.811960	5.274590	12.649100	9.195900
4.80-5.10	4.438710	1.673600	3.027440	1.148070
5.10-5.40	2.969780	0.811371	2.507150	1.616390
5.40-5.70	2.085680	0.401952	0.887770	0.446039
5.70-6.00	0.862470	0.365548	1.141810	0.843397
6.00-6.30	1.078270	0.214765	0.257033	0.080762
6.30-6.60	0.596568	0.160449	0.206103	0.108628
6.60-6.90	0.268941	0.078907	0.029045	0.025154
6.90-7.20	0.083524	0.141331	0.025120	0.025162
7.20-7.50	0.141341	0.071147	0.015265	0.013220
7.50-7.80	0.289726	0.119696	0.031290	0.027098
7.80-8.10	0.275896	0.139406	0.029796	0.025805
8.10-8.40	0.000000	0.000000	0.000000	0.000000
8.40-8.70	0.000000	0.000000	0.000000	0.000000

Table 5.18: Hydrogen Drell-Yan scaling form cross section $M^3d^2\sigma/dMdx_F$ (GeV^2nb) for $0.05 < x_F < 0.1$ bin. Statistical and systematic error are also shown in the respective columns.

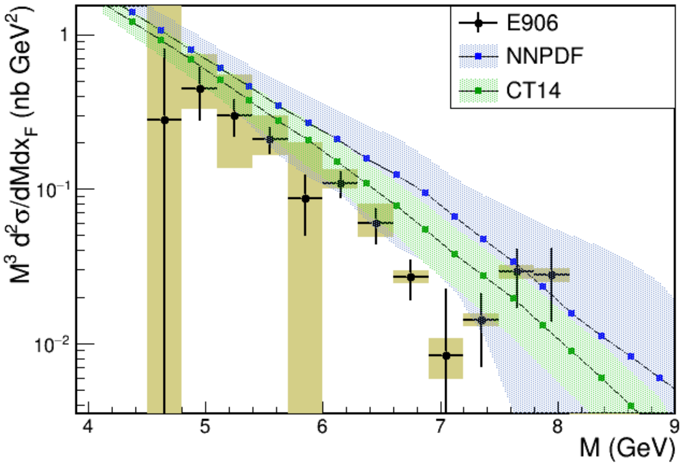

Figure 5.18: p+p absolute Drell-Yan cross section measurement in $x_F = [0.05, 0.1)$

Mass bin (GeV)	$M^3d^2\sigma/dMdx_F(\times10^{-1})$	Stat. error$(\times10^{-1})$	Syst. err(-)$(\times10^{-1})$	Syst. err(+)$(\times10^{-1})$
4.50-4.80	3.498670	3.035200	8.910630	5.436070
4.80-5.10	3.445380	1.119520	3.741310	2.198850
5.10-5.40	2.785450	0.573746	1.665050	0.851111
5.40-5.70	1.181950	0.410870	1.240130	0.760458
5.70-6.00	1.079110	0.346520	0.918764	0.559739
6.00-6.30	1.374750	0.178560	0.148733	0.129703
6.30-6.60	0.525741	0.156032	0.177336	0.072330
6.60-6.90	0.534661	0.103935	0.057742	0.050007
6.90-7.20	0.277647	0.081330	0.029985	0.025968
7.20-7.50	0.166579	0.068589	0.017990	0.015580
7.50-7.80	0.142452	0.071699	0.015385	0.013323
7.80-8.10	0.095162	0.067572	0.010277	0.008900
8.10-8.40	0.146279	0.103979	0.015798	0.013681
8.40-8.70	0.000000	0.000000	0.000000	0.000000

Table 5.19: Hydrogen Drell-Yan scaling form cross section $M^3d^2\sigma/dMdx_F$ (GeV^2nb) for $0.1 < x_F < 0.15$ bin. Statistical and systematic error are also shown in the respective columns.

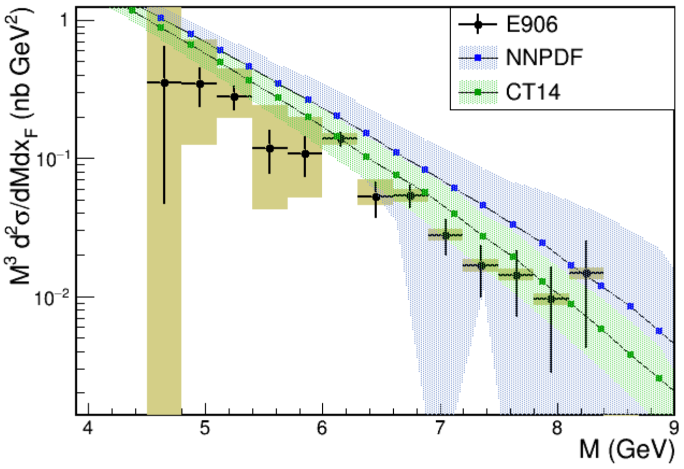

Figure 5.19: p+p absolute Drell-Yan cross section measurement in $x_F = [0.1, 0.15)$

Mass bin (GeV)	$M^3d^2\sigma/dMdx_F(\times 10^{-1})$	Stat. error$(\times 10^{-1})$	Syst. err(-)$(\times 10^{-1})$	Syst. err(+)$(\times 10^{-1})$
4.50-4.80	6.297040	1.492780	4.312100	2.096110
4.80-5.10	5.684980	0.812426	3.048490	1.695330
5.10-5.40	3.931100	0.556727	1.986840	1.075470
5.40-5.70	1.870650	0.312897	0.816748	0.378268
5.70-6.00	1.531080	0.252272	0.467369	0.146571
6.00-6.30	0.926347	0.229763	0.694052	0.486857
6.30-6.60	0.711057	0.159254	0.284466	0.163289
6.60-6.90	0.390969	0.078341	0.042224	0.036567
6.90-7.20	0.382864	0.136616	0.174904	0.107160
7.20-7.50	0.111817	0.142127	0.189430	0.156090
7.50-7.80	0.094758	0.054944	0.010234	0.008863
7.80-8.10	0.039825	0.039892	0.004301	0.003725
8.10-8.40	0.000000	0.000000	0.000000	0.000000
8.40-8.70	0.000000	0.000000	0.000000	0.000000

Table 5.20: Hydrogen Drell-Yan scaling form cross section $M^3d^2\sigma/dMdx_F$ (GeV^2nb) for $0.15 < x_F < 0.2$ bin. Statistical and systematic error are also shown in the respective columns.

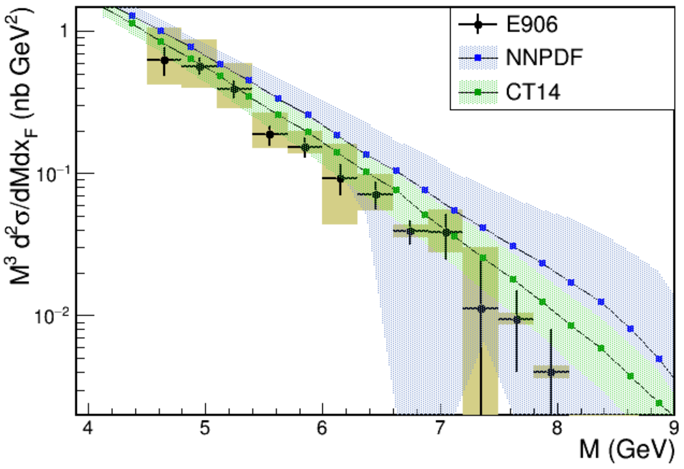

Figure 5.20: p+p absolute Drell-Yan cross section measurement in $x_F = [0.15, 0.2)$

Mass bin (GeV)	$M^3d^2\sigma/dMdx_F(\times10^{-1})$	Stat. error$(\times10^{-1})$	Syst. err(-)$(\times10^{-1})$	Syst. err(+)$(\times10^{-1})$
4.50-4.80	3.464560	0.871899	4.592560	2.998970
4.80-5.10	3.886950	0.577529	2.149810	1.018070
5.10-5.40	2.736380	0.398322	1.633820	0.926951
5.40-5.70	2.008290	0.269159	0.766770	0.350476
5.70-6.00	1.202520	0.232731	0.556635	0.260933
6.00-6.30	0.851740	0.179344	0.507146	0.344035
6.30-6.60	0.797307	0.135624	0.237552	0.113196
6.60-6.90	0.329557	0.103312	0.131173	0.075091
6.90-7.20	0.274774	0.067591	0.029675	0.025700
7.20-7.50	0.007338	0.098748	0.132692	0.118967
7.50-7.80	0.209491	0.074782	0.022625	0.019594
7.80-8.10	0.029645	0.029682	0.003202	0.002773
8.10-8.40	0.000000	0.000000	0.000000	0.000000
8.40-8.70	0.067199	0.067348	0.007257	0.006285

Table 5.21: Hydrogen Drell-Yan scaling form cross section $M^3d^2\sigma/dMdx_F$ (GeV^2nb) for $0.2 < x_F < 0.25$ bin. Statistical and systematic error are also shown in the respective columns.

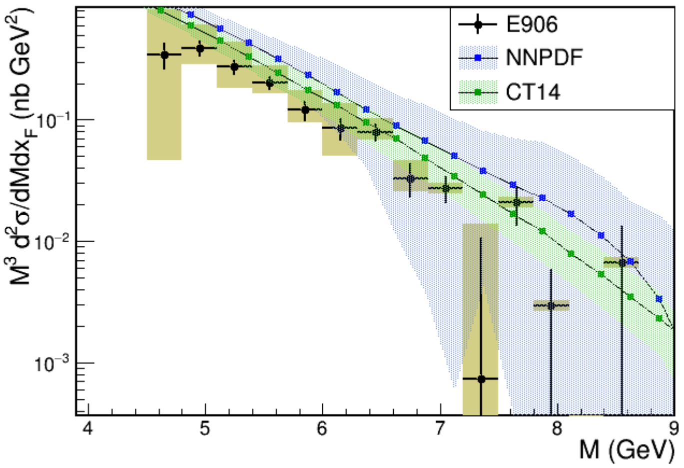

Figure 5.21: p+p absolute Drell-Yan cross section measurement in $x_F = [0.2, 0.25)$

Mass bin (GeV)	$M^3d^2\sigma/dMdx_F(\times10^{-1})$	Stat. error$(\times10^{-1})$	Syst. err(-)$(\times10^{-1})$	Syst. err(+)$(\times10^{-1})$
4.50-4.80	5.643890	0.777430	3.815100	2.022190
4.80-5.10	3.515390	0.442803	2.147660	1.223600
5.10-5.40	2.784590	0.314925	1.137370	0.542337
5.40-5.70	1.916880	0.246659	0.919370	0.521894
5.70-6.00	1.693390	0.159707	0.241170	0.122113
6.00-6.30	0.999085	0.144879	0.248137	0.091512
6.30-6.60	0.562066	0.117463	0.209215	0.115368
6.60-6.90	0.354759	0.112532	0.125615	0.051652
6.90-7.20	0.319723	0.066386	0.034530	0.029904
7.20-7.50	0.132453	0.047152	0.014305	0.012388
7.50-7.80	0.042326	0.029992	0.004571	0.003959
7.80-8.10	0.000000	0.000000	0.000000	0.000000
8.10-8.40	0.000000	0.000000	0.000000	0.000000
8.40-8.70	0.000000	0.000000	0.000000	0.000000

Table 5.22: Hydrogen Drell-Yan scaling form cross section $M^3d^2\sigma/dMdx_F$ (GeV^2nb) for $0.25 < x_F < 0.3$ bin. Statistical and systematic error are also shown in the respective columns.

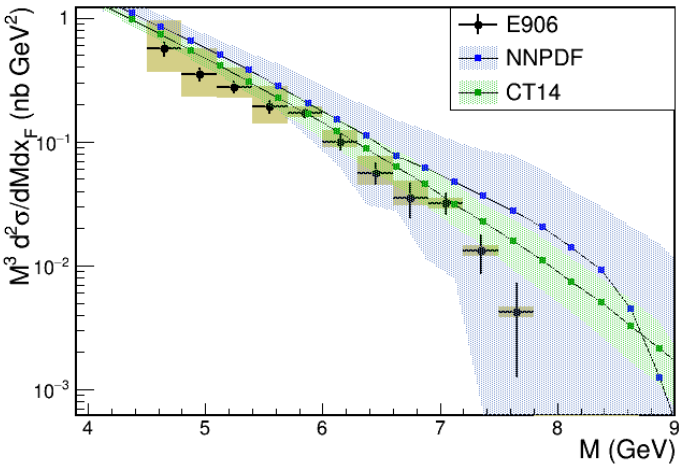

Figure 5.22: p+p absolute Drell-Yan cross section measurement in $x_F = [0.25, 0.3)$

Mass bin (GeV)	$M^3d^2\sigma/dMdx_F(\times10^{-1})$	Stat. error$(\times10^{-1})$	Syst. err(-)$(\times10^{-1})$	Syst. err(+)$(\times10^{-1})$
4.50-4.80	5.058590	0.552202	3.085130	1.802670
4.80-5.10	3.877920	0.408254	1.925170	0.991644
5.10-5.40	2.727350	0.269051	0.983165	0.445275
5.40-5.70	1.965290	0.227154	0.856052	0.473253
5.70-6.00	1.203910	0.174505	0.558761	0.334760
6.00-6.30	0.954828	0.119025	0.160092	0.059584
6.30-6.60	0.657022	0.114161	0.207631	0.103159
6.60-6.90	0.550340	0.081807	0.059436	0.051473
6.90-7.20	0.188201	0.081793	0.104449	0.069186
7.20-7.50	0.028662	0.085624	0.115166	0.100227
7.50-7.80	0.056757	0.116644	0.156491	0.133775
7.80-8.10	0.108613	0.054572	0.011730	0.010159
8.10-8.40	0.104311	0.060450	0.011265	0.009756
8.40-8.70	0.000000	0.000000	0.000000	0.000000

Table 5.23: Hydrogen Drell-Yan scaling form cross section $M^3d^2\sigma/dMdx_F$ (GeV^2nb) for $0.3 < x_F < 0.35$ bin. Statistical and systematic error are also shown in the respective columns.

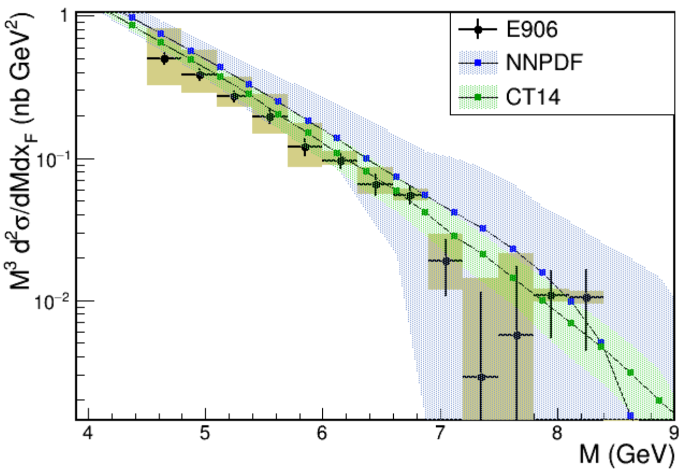

Figure 5.23: p+p absolute Drell-Yan cross section measurement in $x_F = [0.3, 0.35)$

Mass bin (GeV)	$M^3d^2\sigma/dMdx_F(\times10^{-1})$	Stat. error$(\times10^{-1})$	Syst. err(-)$(\times10^{-1})$	Syst. err(+)$(\times10^{-1})$
4.50-4.80	4.840350	0.507323	2.436710	1.205960
4.80-5.10	3.505610	0.315395	1.489140	0.758094
5.10-5.40	3.009380	0.238777	0.774243	0.303942
5.40-5.70	1.281830	0.189480	0.785818	0.511516
5.70-6.00	1.258300	0.150961	0.404421	0.193438
6.00-6.30	0.788144	0.114113	0.247806	0.122686
6.30-6.60	0.542380	0.127992	0.327343	0.223030
6.60-6.90	0.401094	0.065627	0.043317	0.037514
6.90-7.20	0.221000	0.052672	0.023868	0.020670
7.20-7.50	0.183755	0.051413	0.019845	0.017187
7.50-7.80	0.207243	0.060361	0.022382	0.019383
7.80-8.10	0.061457	0.035579	0.006637	0.005748
8.10-8.40	0.029509	0.029538	0.003187	0.002760
8.40-8.70	0.041030	0.041089	0.004431	0.003838

Table 5.24: Hydrogen Drell-Yan scaling form cross section $M^3d^2\sigma/dMdx_F$ (GeV^2nb) for $0.35 < x_F < 0.4$ bin. Statistical and systematic error are also shown in the respective columns.

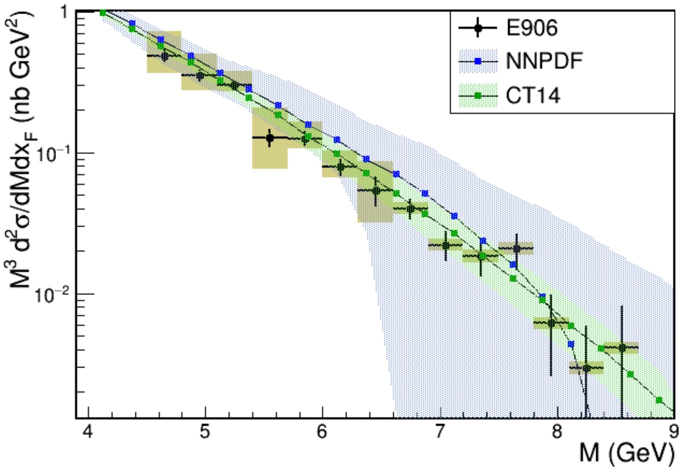

Figure 5.24: p+p absolute Drell-Yan cross section measurement in $x_F = [0.35, 0.4)$

Mass bin (GeV)	$M^3d^2\sigma/dMdx_F(\times10^{-1})$	Stat. error$(\times10^{-1})$	Syst. err(-)$(\times10^{-1})$	Syst. err(+)$(\times10^{-1})$
4.50-4.80	4.988340	0.385753	1.732670	0.755823
4.80-5.10	3.756110	0.303385	1.225840	0.509989
5.10-5.40	2.248770	0.205181	0.839666	0.440209
5.40-5.70	1.640590	0.162738	0.504026	0.222606
5.70-6.00	0.889305	0.136461	0.394759	0.221808
6.00-6.30	0.982255	0.115374	0.204517	0.069667
6.30-6.60	0.652238	0.087618	0.119810	0.045104
6.60-6.90	0.288220	0.092951	0.169592	0.114602
6.90-7.20	0.084356	0.093742	0.177184	0.148739
7.20-7.50	0.109131	0.077655	0.101847	0.077312
7.50-7.80	0.059917	0.030045	0.006471	0.005604
7.80-8.10	-0.036725	0.100668	0.138298	0.130020
8.10-8.40	0.049451	0.035030	0.005341	0.004625
8.40-8.70	0.000000	0.000000	0.000000	0.000000

Table 5.25: Hydrogen Drell-Yan scaling form cross section $M^3d^2\sigma/dMdx_F$ (GeV^2nb) for $0.4 < x_F < 0.45$ bin. Statistical and systematic error are also shown in the respective columns.

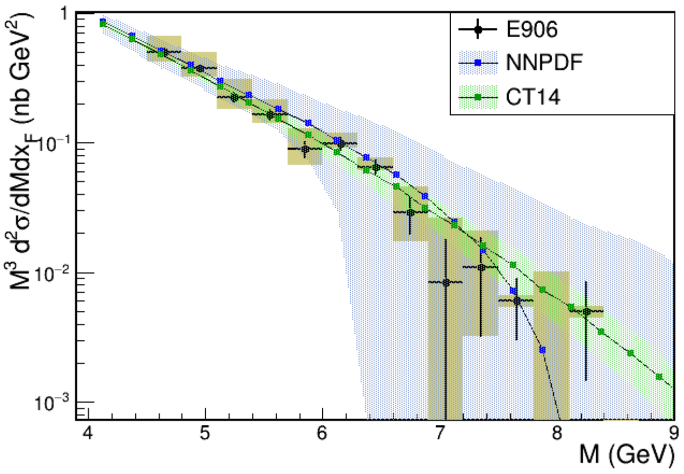

Figure 5.25: p+p absolute Drell-Yan cross section measurement in $x_F = [0.4, 0.45)$

Mass bin (GeV)	$M^3d^2\sigma/dMdx_F(\times10^{-1})$	Stat. error$(\times10^{-1})$	Syst. err(-)$(\times10^{-1})$	Syst. err(+)$(\times10^{-1})$
4.50-4.80	4.101260	0.315042	1.332600	0.510792
4.80-5.10	3.020220	0.221938	0.765845	0.275733
5.10-5.40	1.667550	0.162527	0.641103	0.334043
5.40-5.70	1.251270	0.135544	0.350282	0.131642
5.70-6.00	0.954889	0.097209	0.183709	0.068394
6.00-6.30	0.543989	0.094975	0.207592	0.116117
6.30-6.60	0.495423	0.063855	0.053505	0.046337
6.60-6.90	0.180322	0.062465	0.080559	0.048855
6.90-7.20	0.278613	0.055415	0.030090	0.026059
7.20-7.50	0.199531	0.048881	0.021549	0.018662
7.50-7.80	0.091639	0.037557	0.009897	0.008571
7.80-8.10	0.054247	0.031397	0.005859	0.005074
8.10-8.40	0.046071	0.032665	0.004976	0.004309
8.40-8.70	0.000000	0.000000	0.000000	0.000000

Table 5.26: Hydrogen Drell-Yan scaling form cross section $M^3d^2\sigma/dMdx_F$ (GeV^2nb) for $0.45 < x_F < 0.5$ bin. Statistical and systematic error are also shown in the respective columns.

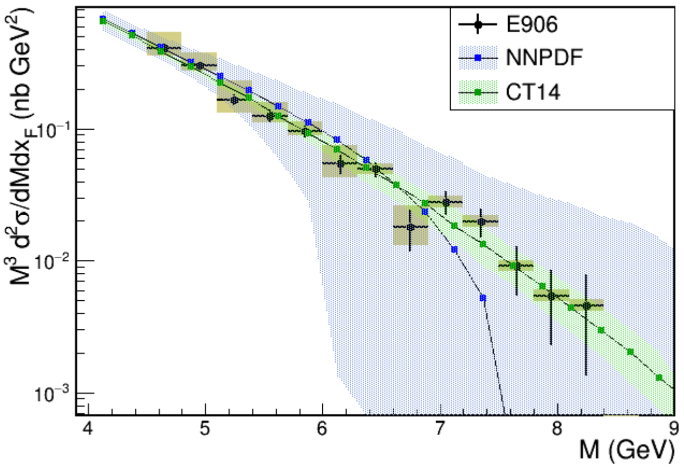

Figure 5.26: p+p absolute Drell-Yan cross section measurement in $x_F = [0.45, 0.5)$

Mass bin (GeV)	$M^3d^2\sigma/dMdx_F(\times10^{-1})$	Stat. error$(\times10^{-1})$	Syst. err(-)$(\times10^{-1})$	Syst. err(+)$(\times10^{-1})$
4.50-4.80	2.769150	0.262616	1.516140	0.912246
4.80-5.10	2.135930	0.171938	0.715045	0.357006
5.10-5.40	1.669340	0.146670	0.463388	0.184411
5.40-5.70	1.083130	0.130991	0.442784	0.243919
5.70-6.00	0.612465	0.111372	0.333739	0.211986
6.00-6.30	0.455751	0.079467	0.143936	0.071481
6.30-6.60	0.375217	0.067762	0.088719	0.035652
6.60-6.90	0.174402	0.037587	0.018835	0.016312
6.90-7.20	0.124435	0.033493	0.013439	0.011638
7.20-7.50	0.097719	0.034729	0.010554	0.009140
7.50-7.80	0.106860	0.037971	0.011541	0.009995
7.80-8.10	0.052178	0.030200	0.005635	0.004880
8.10-8.40	0.040775	0.028879	0.004404	0.003814
8.40-8.70	0.031270	0.031303	0.003377	0.002925

Table 5.27: Hydrogen Drell-Yan scaling form cross section $M^3d^2\sigma/dMdx_F$ (GeV^2nb) for $0.5 < x_F < 0.55$ bin. Statistical and systematic error are also shown in the respective columns.

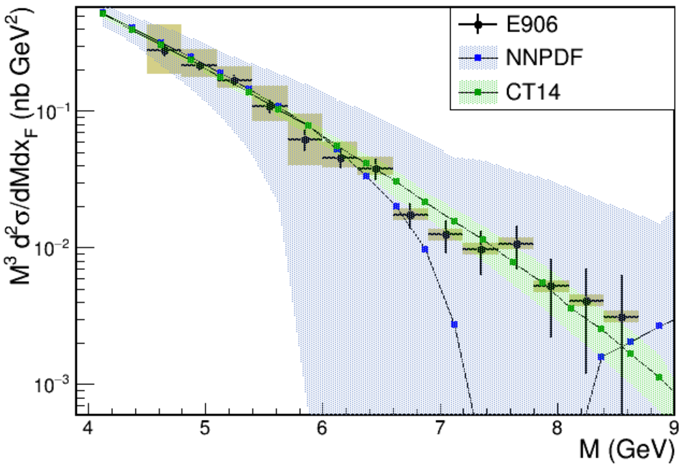

Figure 5.27: p+p absolute Drell-Yan cross section measurement in $x_F = [0.5, 0.55)$

Mass bin (GeV)	$M^3 d^2\sigma/dMdx_F(\times 10^{-1})$	Stat. error$(\times 10^{-1})$	Syst. err(-)$(\times 10^{-1})$	Syst. err(+)$(\times 10^{-1})$
4.50-4.80	2.751080	0.229680	0.952538	0.430516
4.80-5.10	1.572170	0.140382	0.496973	0.228917
5.10-5.40	1.277130	0.123414	0.286651	0.088597
5.40-5.70	0.838409	0.092648	0.204170	0.083741
5.70-6.00	0.455350	0.090843	0.220762	0.131297
6.00-6.30	0.307018	0.092166	0.267190	0.200048
6.30-6.60	0.259297	0.060220	0.077584	0.037084
6.60-6.90	0.204107	0.041329	0.022043	0.019090
6.90-7.20	0.135473	0.036477	0.014631	0.012671
7.20-7.50	0.100824	0.033786	0.010889	0.009430
7.50-7.80	0.037355	0.021605	0.004034	0.003494
7.80-8.10	0.015220	0.015230	0.001644	0.001424
8.10-8.40	0.020827	0.020842	0.002249	0.001948
8.40-8.70	0.053087	0.037624	0.005733	0.004965

Table 5.28: Hydrogen Drell-Yan scaling form cross section $M^3 d^2\sigma/dMdx_F$ $(GeV^2 nb)$ for $0.55 < x_F < 0.6$ bin. Statistical and systematic error are also shown in the respective columns.

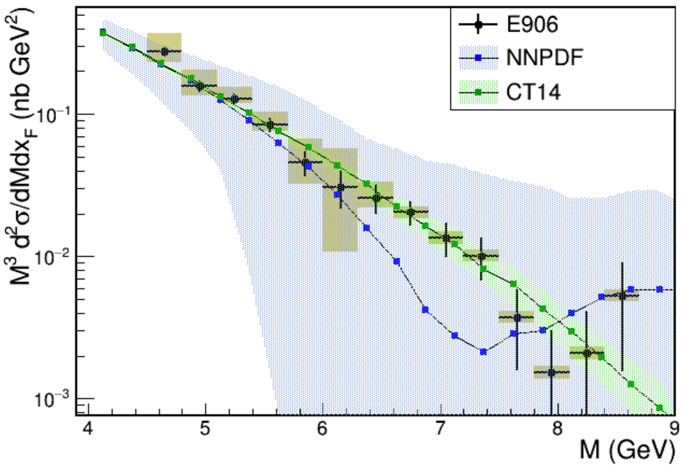

Figure 5.28: p+p absolute Drell-Yan cross section measurement in $x_F = [0.55, 0.6)$

Mass bin (GeV)	$M^3d^2\sigma/dMdx_F(\times 10^{-1})$	Stat. error$(\times 10^{-1})$	Syst. err(-)$(\times 10^{-1})$	Syst. err(+)$(\times 10^{-1})$
4.50-4.80	1.735690	0.155351	0.624841	0.304760
4.80-5.10	1.204530	0.121035	0.368827	0.166371
5.10-5.40	0.831167	0.093282	0.256152	0.125051
5.40-5.70	0.579958	0.069146	0.127104	0.048808
5.70-6.00	0.423531	0.078712	0.173689	0.101005
6.00-6.30	0.284658	0.063598	0.114249	0.065693
6.30-6.60	0.223554	0.040128	0.024143	0.020909
6.60-6.90	0.156728	0.056638	0.073184	0.045278
6.90-7.20	0.084829	0.028421	0.009161	0.007934
7.20-7.50	0.051228	0.022988	0.005533	0.004791
7.50-7.80	0.049673	0.024893	0.005365	0.004646
7.80-8.10	0.014438	0.014447	0.001559	0.001350
8.10-8.40	0.000000	0.000000	0.000000	0.000000
8.40-8.70	0.028466	0.028491	0.003074	0.002662

Table 5.29: Hydrogen Drell-Yan scaling form cross section $M^3d^2\sigma/dMdx_F$ (GeV^2nb) for $0.6 < x_F < 0.65$ bin. Statistical and systematic error are also shown in the respective columns.

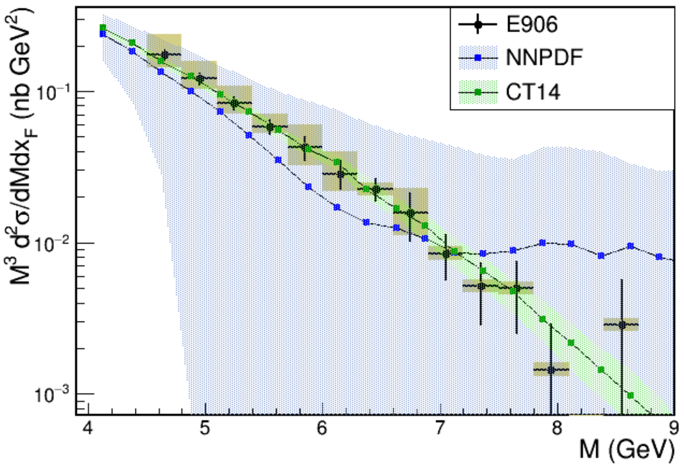

Figure 5.29: p+p absolute Drell-Yan cross section measurement in $x_F = [0.6, 0.65)$

Mass bin (GeV)	$M^3d^2\sigma/dMdx_F(\times10^{-1})$	Stat. error$(\times10^{-1})$	Syst. err(-)$(\times10^{-1})$	Syst. err(+)$(\times10^{-1})$
4.50-4.80	1.211530	0.117751	0.319263	0.117000
4.80-5.10	0.721451	0.090208	0.235313	0.108109
5.10-5.40	0.715561	0.086937	0.217106	0.104817
5.40-5.70	0.526777	0.056596	0.056891	0.049269
5.70-6.00	0.237531	0.054257	0.096930	0.056223
6.00-6.30	0.209621	0.062189	0.113110	0.074168
6.30-6.60	0.131584	0.048047	0.061427	0.037999
6.60-6.90	0.091021	0.026434	0.009830	0.008513
6.90-7.20	0.135744	0.035338	0.014660	0.012696
7.20-7.50	0.040303	0.020212	0.004353	0.003770
7.50-7.80	0.060232	0.027014	0.006505	0.005633
7.80-8.10	0.000000	0.000000	0.000000	0.000000
8.10-8.40	0.000000	0.000000	0.000000	0.000000
8.40-8.70	0.000000	0.000000	0.000000	0.000000

Table 5.30: Hydrogen Drell-Yan scaling form cross section $M^3d^2\sigma/dMdx_F$ (GeV^2nb) for $0.65 < x_F < 0.7$ bin. Statistical and systematic error are also shown in the respective columns.

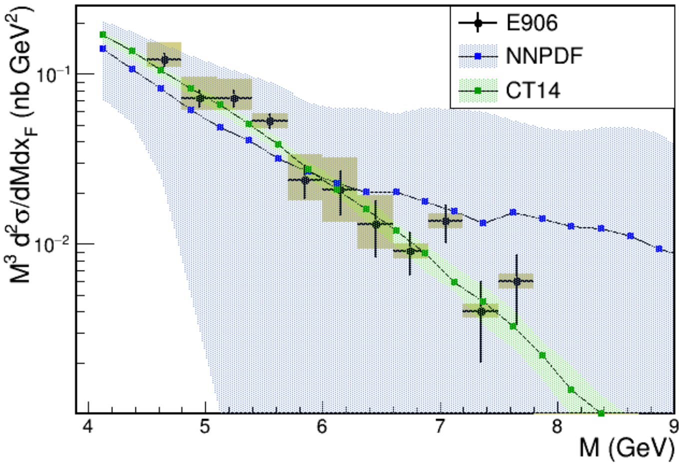

Figure 5.30: p+p absolute Drell-Yan cross section measurement in $x_F = [0.65, 0.7)$

Mass bin (GeV)	$M^3d^2\sigma/dMdx_F(\times 10^{-1})$	Stat. error$(\times 10^{-1})$	Syst. err(-)$(\times 10^{-1})$	Syst. err(+)$(\times 10^{-1})$
4.50-4.80	0.780247	0.091080	0.179521	0.051308
4.80-5.10	0.524857	0.073890	0.176245	0.086100
5.10-5.40	0.320676	0.049324	0.065883	0.024671
5.40-5.70	0.245414	0.044618	0.057152	0.022737
5.70-6.00	0.175208	0.031508	0.018922	0.016387
6.00-6.30	0.161202	0.032029	0.017410	0.015077
6.30-6.60	0.127879	0.044683	0.056206	0.033827
6.60-6.90	0.027857	0.043041	0.056456	0.047260
6.90-7.20	0.008836	0.008840	0.000954	0.000826
7.20-7.50	0.020848	0.014758	0.002252	0.001950
7.50-7.80	0.016511	0.016523	0.001783	0.001544
7.80-8.10	0.000000	0.000000	0.000000	0.000000
8.10-8.40	0.005778	0.005795	0.000624	0.000540
8.40-8.70	0.000000	0.000000	0.000000	0.000000

Table 5.31: Hydrogen Drell-Yan scaling form cross section $M^3d^2\sigma/dMdx_F$ (GeV^2nb) for $0.7 < x_F < 0.75$ bin. Statistical and systematic error are also shown in the respective columns.

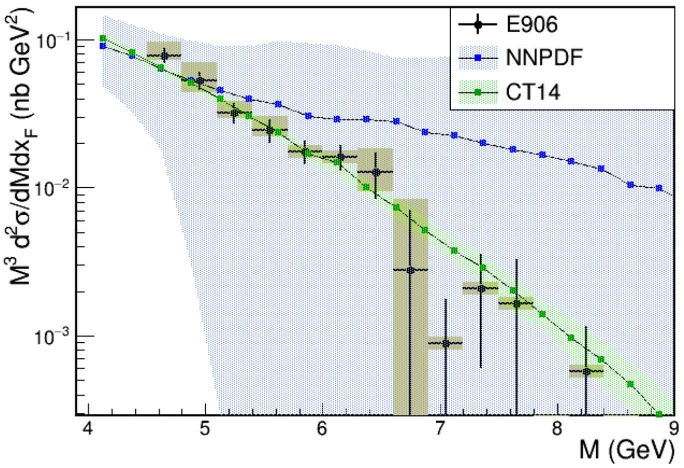

Figure 5.31: p+p absolute Drell-Yan cross section measurement in $x_F = [0.7, 0.75)$

Mass bin (GeV)	$M^3d^2\sigma/dMdx_F(\times10^{-1})$	Stat. error($\times10^{-1}$)	Syst. err(-)($\times10^{-1}$)	Syst. err(+)($\times10^{-1}$)
4.50-4.80	0.263829	0.072385	0.199215	0.139059
4.80-5.10	0.220230	0.053483	0.089214	0.046241
5.10-5.40	0.207120	0.032812	0.022368	0.019372
5.40-5.70	0.119593	0.038440	0.049952	0.029322
5.70-6.00	0.118332	0.025541	0.012780	0.011068
6.00-6.30	0.099435	0.025085	0.010739	0.009300
6.30-6.60	0.034818	0.015612	0.003760	0.003256
6.60-6.90	0.037931	0.019019	0.004096	0.003548
6.90-7.20	0.031516	0.018244	0.003404	0.002948
7.20-7.50	0.014474	0.010268	0.001563	0.001354
7.50-7.80	0.000000	0.000000	0.000000	0.000000
7.80-8.10	0.000000	0.000000	0.000000	0.000000
8.10-8.40	0.000000	0.000000	0.000000	0.000000
8.40-8.70	0.000000	0.000000	0.000000	0.000000

Table 5.32: Hydrogen Drell-Yan scaling form cross section $M^3d^2\sigma/dMdx_F$ (GeV^2nb) for $0.75 < x_F < 0.8$ bin. Statistical and systematic error are also shown in the respective columns.

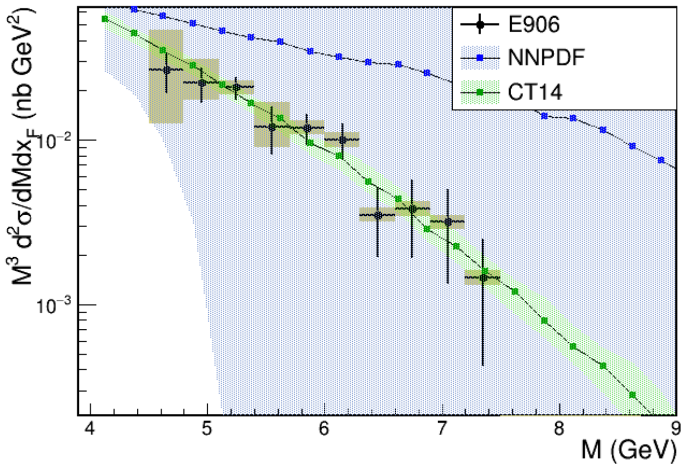

Figure 5.32: p+p absolute Drell-Yan cross section measurement in $x_F = [0.75, 0.8)$

Chapter 6

Features of kinematic dependence of $< p_T >$ from analysis of existing Drell-Yan data

6.1 Introduction

In parton model, quarks carry a fraction of the total longitudinal momentum of the hadron in the infinite momentum frame. Uncertainty principle implies non-zero intrinsic transverse momentum of quarks arising from the confinement of quark inside hadron. The size of the hadron is of the order of $\sim$ 1 fm. This leads to a mean momentum in transverse direction $< p_T > \sim 0.2$ GeV/c. A virtual photon produced from annihilation of two such partons in the Drell-Yan process is expected to have a $< p_T > \sim 0.3$ GeV/c. However, it was observed in Drell-Yan experiments that the dimuon mean p_T ($\sim$ 1 GeV/c) is significantly larger than 0.3 GeV/c. This observation provided a strong evidence for the important role of QCD in the Drell-Yan process.

With the emission of gluons, the quarks acquire a transverse kick, thus providing additional transverse momentum to the dileptons produced in the Drell-Yan process. The focus of this chapter is to provide a systematic study of the transverse momentum data from existing Drell-Yan experiments and to search for universal behaviour pertaining to the transverse momentum distributions such as,

- Dependence of p_T distribution on $\sqrt{s}$
- Dependence of p_T distribution on Feynman-x (x_F) and dimuon mass (M)
- Dependence of p_T distribution on the type of quarks (valence or sea)
- Dependence of p_T distribution on the type of beam hadron (baryon or meson)

6.2 Existing fixed target Drell-Yan experiments

This section presents the analysis details and results from available fixed-target Drell-Yan p_T data. Table 6.1 lists the experiments, their beam energies and the corresponding beam and target types. The data for all the listed experiments have been taken from [54] except for E866 and NA10, which have been taken from respective thesis referenced in the table below.

Experiment	P_{beam} (GeV)	$\sqrt{s}$ (GeV)	Beam	Target	Reference
E866	800	38.7	p	H_2,D_2	[4]
E772	800	38.7	p	D_2	[7, 8]
E288	200,300,400	19.4, 23.7, 27.4	p	Pt	[6]
E605	800	38.7	p	Cu	[30]
E537	125	15.3	$\bar{p}$	W	[55]
E615	252	21.7	π^-	W	[36]
E537	125	15.3	π^-	W	[55]
NA10	194,284	19.1, 23.1	π^-	W	[56]

Table 6.1: Summary of analysed p_T data

6.2.1 Method

Typically, the Drell-Yan p_T distribution is fit either with gaussian functional form or Kaplan functional form. The gaussian functional form is

$$\frac{d\sigma}{dp_T^2}(x_F, M) = p_0'\exp(-\frac{p_T^2}{p_1'^2}) \tag{6.1}$$

where parameter p_1' is related to the mean of the distribution.

Similarly, the Kaplan functional form is

$$\frac{d\sigma}{dp_T^2}(x_F, M) = p_0\left(1 + \frac{p_T^2}{p_1^2}\right)^{-6} \tag{6.2}$$

In the case of Kaplan distribution parameter p_1 is related to the mean of the distribution. Figure 6.1 shows a shape comparison of both functional form. They have very similar shape for low p_T. At low p_T, the equations 6.1 and 6.2 can be taylor expanded and $p_1$and p_1' are related as $p_1^2 = 6p_1'^2$. At high p_T gaussian has a sharper fall-off while Kaplan functional form has a high p_T tail.

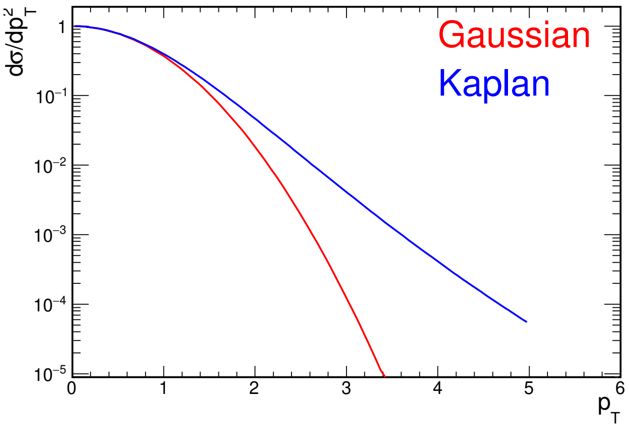

Figure 6.1: A comparison of shape for Kaplan and Gaussian function. At low p_T, shape of both the functions are very similar. However for large p_T, the shape differs. The gaussian function has a sharper fall-off, while, Kaplan has a high p_T tail.

For the purpose of this analysis, the Kaplan functional form is chosen to fit the available data. The parameter p_1 in Kaplan form, equation 6.2, is related to the mean p_T and mean p_T^2 as follows,

$$< p_T >= \frac{\int p_T \frac{d\sigma}{dp_T} dp_T}{\int \frac{d\sigma}{dp_T} dp_T} \qquad < p_T^2 >= \frac{\int p_T^2 \frac{d\sigma}{dp_T} dp_T}{\int \frac{d\sigma}{dp_T} dp_T} \tag{6.3}$$

Using analytical expressions,

$$\int_0^\infty \frac{x}{(1+\frac{x^2}{a})^6} dx = \frac{a}{10}, \qquad \int_0^\infty \frac{x^2}{(1+\frac{x^2}{a})^6} dx = \frac{7\pi a^{3/2}}{512}, \quad \text{and} \quad \int_0^\infty \frac{x^3}{(1+\frac{x^2}{a})^6} dx = \frac{a^2}{40} \tag{6.4}$$

We obtain from equations 6.3 and 6.4

$$< p_T >= \frac{35\pi p_1}{256} \quad \text{and} \quad < p_T^2 >= \frac{p_1^2}{4} \tag{6.5}$$

Proton induced Drell-Yan

- E866 $p + p/d \to \mu^+ + \mu^- + X$ at 800 GeV/c

  The relevant E866 data are unpublished but available from Jason Webb's thesis [4]. The invariant form of cross section, $E\frac{d^3\sigma}{dp^3}$ is provided as a function of p_T for mass range 4.2 – 8.7 GeV and 10.85 – 16.85

GeV and x_F varying from -0.05 to 0.8.

$$E\frac{d^3\sigma}{dp^3} = \frac{2E}{\pi\sqrt{s}}\frac{d^2\sigma}{dx_F dp_T^2} \tag{6.6}$$

Using the functional form proposed by Kaplan, the data are fitted to obtain mean p_T for each data set. The data also contain information about the $< M >$ and $< x_F >$ for each p_T distribution. Solving the following two equations for a given mass and x_F to obtain a quadratic equation whose roots are x_1 and x_2

$$\tau = \frac{M^2}{s} = x_1 x_2 \qquad\qquad x_F = x_1 - x_2$$

Thus one obtains

$$x_2^2 + x_F x_2 - M^2/s = 0$$

where $\sqrt{s} = 38.763$ GeV for $p_{\text{beam}} = 800$ GeV

$$x_1 = \frac{1}{2}[x_F + (x_F^2 + \frac{4M^2}{s})^{1/2}] \qquad\qquad x_2 = \frac{1}{2}[-x_F + (x_F^2 + \frac{4M^2}{s})^{1/2}] \tag{6.7}$$

Table 6.2 and 6.3 presents $< p_T >$ and $< p_T^2 >$ obtained from Kaplan fit to hydrogen and deuterium data. respectively.

x_F	x_1	x_2	$< p_T >$	$< p_T^2 >$
$4.2 < M < 5.2$; $< M >= 4.65$ or $\tau = 0.01439$				
0.12	0.194	0.074	1.216 ± 0.043	2.007 ± 0.143
0.25	0.298	0.482	1.192 ± 0.021	1.927 ± 0.069
0.43	0.461	0.031	1.083 ± 0.021	1.593 ± 0.063
0.62	0.642	0.022	0.986 ± 0.036	1.321 ± 0.098
$5.2 < M < 6.2$; $< M >= 5.68$ or $\tau = 0.02147$				
0.12	0.218	0.098	1.214 ± 0.066	2.002 ± 0.218
0.27	0.334	0.064	1.215 ± 0.021	2.005 ± 0.071
0.44	0.484	0.044	1.122 ± 0.019	1.709 ± 0.058
0.62	0.652	0.032	1.020 ± 0.026	1.413 ± 0.073
$6.2 < M < 7.2$; $< M >= 6.69$ or $\tau = 0.02978$				
0.11	0.236	0.126	1.138 ± 0.093	1.758 ± 0.289
0.28	0.362	0.082	1.206 ± 0.023	1.974 ± 0.076
0.44	0.499	0.059	1.179 ± 0.013	1.886 ± 0.043
0.63	0.674	0.044	1.045 ± 0.027	1.483 ± 0.078
$7.2 < M < 8.7$; $< M >= 8.05$ or $\tau = 0.04312$				
0.10	0.263	0.163	1.239 ± 0.044	2.085 ± 0.148
0.26	0.375	0.115	1.277 ± 0.023	2.214 ± 0.080
0.44	0.522	0.082	1.212 ± 0.019	1.993 ± 0.064
0.62	0.683	0.063	1.053 ± 0.028	1.506 ± 0.081
$10.85 < M < 12.85$; $< M >= 11.25$ or $\tau = 0.08423$				
0.10	0.350	0.240	1.453 ± 0.741	2.864 ± 2.922
0.26	0.462	0.182	1.407 ± 0.109	2.686 ± 0.417
0.44	0.584	0.144	1.336 ± 0.071	2.424 ± 0.260
0.62	0.726	0.116	1.271 ± 0.103	2.193 ± 0.357
$12.85 < M < 16.85$; $< M >= 13.18$ or $\tau = 0.1156$				
0.27	0.500	0.230	1.833 ± 0.584	4.558 ± 2.905
0.45	0.632	0.182	1.261 ± 0.319	2.159 ± 1.092
0.64	0.786	0.146	0.864 ± 0.428	1.013 ± 1.005

Table 6.2: $< p_T >$ (in GeV/c) and $< p_T^2 >$ (in GeV^2/c^2) for E866 p+p Drell-Yan in different mass and x_F bins; the x_1 and x_2 are calculated using the tabulated $< x_F >$ value and $< M >$

x_F	x_1	x_2	$< p_T >$	$< p_T^2 >$
$4.2 < M < 5.2; < M >= 4.65$ or $\tau = 0.01439$				
0.12	0.194	0.074	1.173 ± 0.028	1.867 ± 0.090
0.25	0.298	0.482	1.221 ± 0.016	2.023 ± 0.053
0.43	0.461	0.031	1.085 ± 0.016	1.597 ± 0.048
0.62	0.642	0.022	1.035 ± 0.027	1.454 ± 0.077
$5.2 < M < 6.2; < M >= 5.68$ or $\tau = 0.02147$				
0.12	0.218	0.098	1.191 ± 0.054	1.926 ± 0.177
0.27	0.334	0.064	1.201 ± 0.018	1.958 ± 0.058
0.44	0.484	0.044	1.123 ± 0.013	1.710 ± 0.041
0.62	0.652	0.032	1.035 ± 0.018	1.504 ± 0.053
$6.2 < M < 7.2; < M >= 6.69$ or $\tau = 0.02978$				
0.11	0.236	0.126	1.211 ± 0.065	1.990 ± 0.216
0.28	0.362	0.082	1.249 ± 0.018	2.117 ± 0.061
0.44	0.499	0.059	1.170 ± 0.014	1.857 ± 0.045
0.63	0.674	0.044	1.021 ± 0.017	1.414 ± 0.048
$7.2 < M < 8.7; < M >= 8.05$ or $\tau = 0.04312$				
0.10	0.263	0.163	1.292 ± 0.030	2.266 ± 0.108
0.26	0.375	0.115	1.281 ± 0.016	2.229 ± 0.059
0.44	0.522	0.082	1.203 ± 0.014	1.965 ± 0.046
0.62	0.683	0.063	1.086 ± 0.018	1.600 ± 0.055
$10.85 < M < 12.85; < M >= 11.25$ or $\tau = 0.08423$				
0.10	0.350	0.240	1.730 ± 0.513	4.060 ± 2.407
0.26	0.462	0.182	1.286 ± 0.059	2.244 ± 0.206
0.44	0.584	0.144	1.226 ± 0.043	2.042 ± 0.145
0.62	0.726	0.116	1.167 ± 0.070	1.849 ± 0.223
$12.85 < M < 16.85; < M >= 13.18$ or $\tau = 0.1156$				
0.27	0.500	0.230	1.529 ± 0.452	3.171 ± 1.878
0.45	0.632	0.182	1.263 ± 0.121	2.165 ± 0.416
0.64	0.786	0.146	1.156 ± 0.127	1.813 ± 0.400

Table 6.3: $< p_T >$ (in GeV/c) and $< p_T^2 >$ (in GeV^2/c^2) for E866 p+d Drell-Yan in different mass and x_F bins; the x_1 and x_2 are calculated using the tabulated $< x_F >$ value and $< M >$

- E772 $p + d \rightarrow \mu^+ + \mu^- + X$ at 800 GeV/c

  The invariant form of cross section $Ed^3\sigma/dp^3$ (in units $pb/GeV^2/nucleon$) is tabulated for different mass bins with x_F in the range $[0.1, 0.3]$ [7, 8]. The p_T distribution was analysed in each mass bins to obtain the mean p_T. The result is tabulated in table 6.4

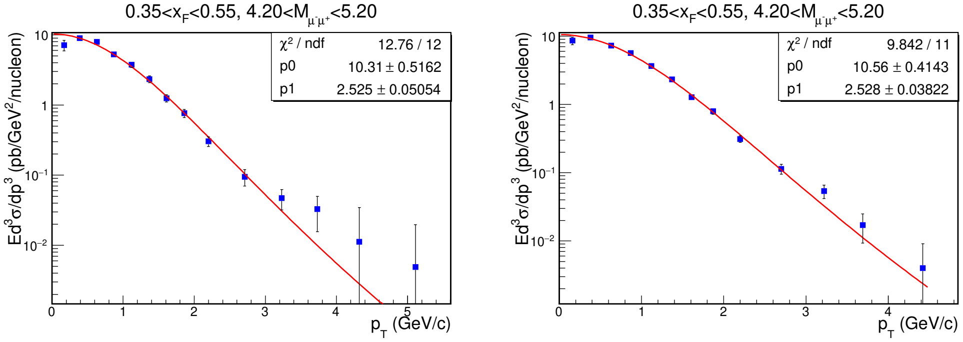

(a) Hydrogen (b) Deuterium

Figure 6.2: Kaplan fits to hydrogen data (left) and deuterium data (right) for $0.15 < x_F < 0.35$ and $4.2 < M_{\mu^-\mu^+} < 5.2$ GeV/c^2 bin. Similar fits have been performed for all the x_F and $M_{\mu^-\mu^+}$ bin to get the the value of $< p_T >$ and $< p_T^2 >$ shown in table 6.2 and 6.3.

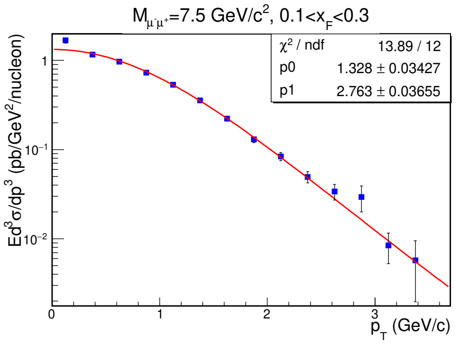

Figure 6.3: Kaplan fit for $M_{\mu^-\mu^+}$=7.5 GeV/c^2 bin (E772).

M	p_1	$< p_T >$	$< p_T^2 >$
5.5	2.758 ± 0.029	1.184 ± 0.012	1.901 ± 0.040
6.5	2.660 ± 0.025	1.142 ± 0.011	1.768 ± 0.034
7.5	2.763 ± 0.036	1.186 ± 0.015	1.908 ± 0.050
8.5	2.728 ± 0.043	1.171 ± 0.018	1.860 ± 0.058
11.5	2.746 ± 0.136	1.179 ± 0.058	1.885 ± 0.187
12.5	2.694 ± 0.197	1.157 ± 0.084	1.814 ± 0.265
13.5	2.753 ± 0.492	1.182 ± 0.211	1.894 ± 0.678
14.5	3.137 ± 1.570	1.347 ± 0.674	2.460 ± 2.462

Table 6.4: $< p_T >$ (in GeV/c) and $< p_T^2 >$ (in GeV^2/c^2) for p+d Drell-Yan in different mass bins for E772 experiment

- E288 $p + Pt \to \mu^+ + \mu^- + X$ at 200/300/400 GeV/c

  The invariant form of cross section $Ed^3\sigma/dp^3$ (in units $cm^2/GeV^2/nucleon$) is tabulated for different mass bins at three different proton beam energy [6]. The p_T distribution was analysed in each mass bin to obtain the mean p_T. The result is tabulated in table 6.5

M	p_1	$< p_T >$	$< p_T^2 >$	$\sqrt{\tau}$=M(bin center)/$\sqrt{s}$	x_F=$\sqrt{\tau}(e^{<y>} - e^{-<y>})$
p_{beam} = 200 GeV/c, $< y >= 0.40$					
4-5	2.268 ± 0.040	0.974 ± 0.017	1.285 ± 0.046	0.23	0.191
5-6	2.283 ± 0.050	0.980 ± 0.021	1.303 ± 0.058	0.28	0.234
6-7	2.322 ± 0.058	0.997 ± 0.025	1.347 ± 0.067	0.34	0.277
7-8	2.269 ± 0.101	0.974 ± 0.043	1.287 ± 0.115	0.39	0.319
8-9	2.246 ± 0.198	0.964 ± 0.085	1.261 ± 0.223	0.44	0.362
9-10	2.742 ± 0.438	1.177 ± 0.188	1.879 ± 0.601	0.49	0.404
p_{beam} = 300 GeV/c, $< y >= 0.21$					
4-5	2.458 ± 0.052	1.055 ± 0.022	1.510 ± 0.064	0.19	0.08
5-6	2.447 ± 0.042	1.051 ± 0.018	1.496 ± 0.051	0.23	0.098
6-7	2.590 ± 0.050	1.112 ± 0.021	1.677 ± 0.065	0.27	0.116
7-8	2.594 ± 0.071	1.114 ± 0.030	1.682 ± 0.092	0.32	0.133
8-9	2.457 ± 0.085	1.055 ± 0.036	1.509 ± 0.105	0.36	0.152
9-10	2.423 ± 0.099	1.040 ± 0.042	1.467 ± 0.120	0.40	0.169
10-11	2.454 ± 0.211	1.054 ± 0.090	1.505 ± 0.259	0.44	0.187
11-12	4.028 ± 2.718	1.730 ± 1.167	4.056 ± 5.474	0.48	0.205
p_{beam} = 400 GeV/c, $< y >= 0.03$					
5-6	2.746 ± 0.034	1.179 ± 0.014	1.885 ± 0.047	0.20	0.012
6-7	2.744 ± 0.018	1.178 ± 0.007	1.882 ± 0.025	0.24	0.014
7-8	2.853 ± 0.022	1.225 ± 0.009	2.034 ± 0.032	0.27	0.016
8-9	2.809 ± 0.028	1.206 ± 0.012	1.972 ± 0.039	0.31	0.19
9-10	3.019 ± 0.034	1.296 ± 0.014	2.278 ± 0.051	0.35	0.021
10-11	3.003 ± 0.046	1.289 ± 0.019	2.254 ± 0.069	0.38	0.023
11-12	2.732 ± 0.041	1.173 ± 0.017	1.865 ± 0.057	0.42	0.025
12-13	2.960 ± 0.153	1.271 ± 0.065	2.190 ± 0.226	0.46	0.027
13-14	2.809 ± 0.262	1.206 ± 0.112	1.972 ± 0.368	0.49	0.029

Table 6.5: $< p_T >$ (in GeV/c) and $< p_T^2 >$ (in GeV^2/c^2) for p+d Drell-Yan in different mass bins for E288 experiment for $p_{\rm beam}$ = 200 GeV, 300 GeV and 400 GeV.

- E605 $p + Cu \to \mu^+ + \mu^- + X$ at 800 GeV/c

  The invariant form of cross section $Ed^3\sigma/dp^3$ (in units $cm^2/GeV^2/nucleon$) is tabulated for different mass bins with x_F in the range $(-0.1, 0.2)$ [30]. The p_T distribution was analysed in each mass bin to obtain the mean p_T. The result is tabulated in table 6.6

M	$\sqrt{\tau}$	$< x_F >$	p_1	$< p_T >$
7-8	0.194	0.1	3.24 ± 0.12	1.39 ± 0.05
8-9	0.219	0.1	3.16 ± 0.04	1.36 ± 0.02
10.5-11.5	0.284	0.1	3.06 ± 0.04	1.31 ± 0.02
11.5-13.5	0.323	0.1	3.09 ± 0.04	1.32 ± 0.02
13.5-18	0.400	0.1	2.96 ± 0.08	1.27 ± 0.04

Table 6.6: $< p_T >$ (in GeV/c) and $< p_T^2 >$ (in GeV^2/c^2) for p+Cu Drell-Yan in different mass bins for E605 experiment

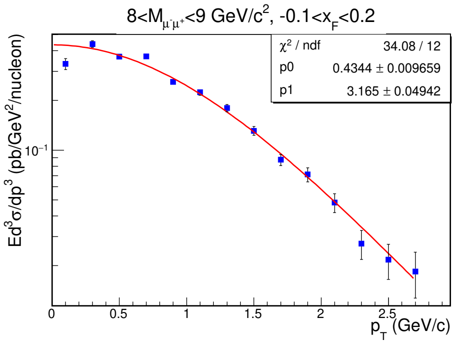

Figure 6.4: Kaplan fit for $M_{\mu^-\mu^+}$=8-9 GeV/c^2 bin for E605 experiment.

Antiproton induced Drell-Yan

- E537 $\bar{p} + W \rightarrow \mu^+ + \mu^- + X$ at 125 GeV/c

  $d^2\sigma/dmdp_T^2$ (in units $cm^2/GeV^3/nucleon$) and $d^2\sigma/dxdp_T^2$ (in units $cm^2/GeV^2/nucleon$) as a function of p_T^2 is tabulated for different mass bin and x_F bins [55]. The p_T distribution was analysed in each mass bins to obtain the mean p_T. The result is tabulated in table 6.7

M	p_1	$< p_T >$	$< p_T^2 >$
4-4.5	2.123 ± 0.090	.911 ± .038	1.127 ± 0.095
4.5-5	1.872 ± 0.136	.804 ± .058	0.876 ± 0.127
5-5.5	2.109 ± 0.179	.905 ± .076	1.112 ± 0.188
5.5-6	1.577 ± 0.422	.677 ± .181	0.621 ± 0.332

x_F	p_1	$< p_T >$	$< p_T^2 >$
-0.1-0	2.353 ± 0.296	1.010 ± 0.127	1.384 ± 0.348
0-0.1	2.095 ± 0.193	0.899 ± 0.083	1.097 ± 0.202
0.1-0.2	2.238 ± 0.177	0.961 ± 0.076	1.252 ± 0.198
0.2-0.3	1.979 ± 0.143	0.849 ± 0.061	0.979 ± 0.141
0.3-0.4	2.102 ± 0.157	0.902 ± 0.067	1.105 ± 0.165
0.4-0.5	2.048 ± 0.222	0.879 ± 0.095	1.048 ± 0.227
0.5-0.6	2.193 ± 0.419	0.941 ± 0.180	1.202 ± 0.460

Table 6.7: $< p_T >$ (in GeV/c) and $< p_T^2 >$ (in GeV^2/c^2) for $\bar{p}$+W Drell-Yan in different mass and x_F bins for E537 experiment

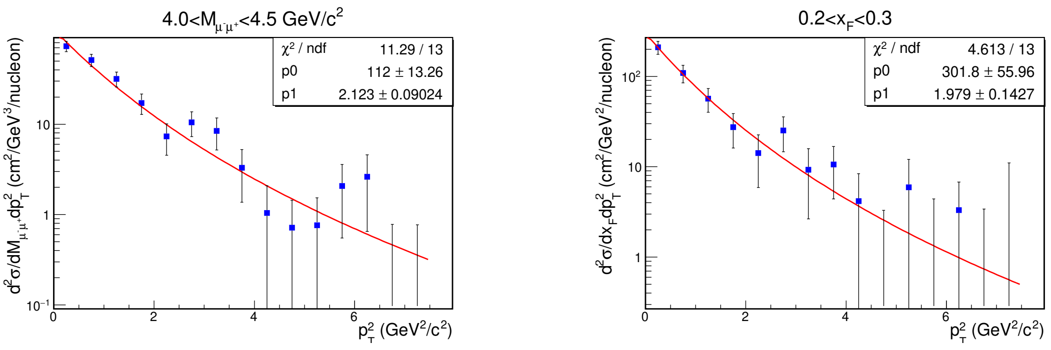

(a) Kaplan fit to E537 antiproton data in $M_{\mu^-\mu^+}$=4-4.5 GeV/c^2 bin.

(b) Kaplan fit to E537 antiproton data in x_F=0.2-0.3 bin.

Figure 6.5

Pion induced Drell-Yan

- E537 $\pi^- + W \rightarrow \mu^+ + \mu^- + X$ at 125 GeV/c

  $d^2\sigma/dmdp_T^2$ (in units $cm^2/GeV^3/nucleon$) and $d^2\sigma/dxdp_T^2$ (in units $cm^2/GeV^2/nucleon$) as a function of p_T^2 is tabulated for different mass bin and x_F bins [55]. The p_T distribution was analysed in each mass bins to obtain the mean p_T. The result is tabulated in table 6.8

M	p_1	$< p_T >$	$< p_T^2 >$
4-4.5	2.245 ± 0.059	.964 ± .025	1.260 ± 0.066
4.5-5	2.235 ± 0.091	.959 ± .039	1.249 ± 0.102
5-5.5	2.23 ± 0.138	.957 ± .059	1.243 ± 0.154
5.5-6	2.363 ± 0.164	1.014 ± .070	1.396 ± 0.194

x_F	p_1	$< p_T >$	$< p_T^2 >$
-0.1-0	2.104 ± 0.232	0.903 ± 0.099	1.107 ± 0.244
0-0.1	1.914 ± 0.156	0.822 ± 0.067	0.916 ± 0.150
0.1-0.2	2.384 ± 0.122	1.023 ± 0.052	1.421 ± 0.146
0.2-0.3	2.238 ± 0.099	0.961 ± 0.043	1.252 ± 0.111
0.3-0.4	2.303 ± 0.100	0.989 ± 0.043	1.326 ± 0.116
0.4-0.5	2.262 ± 0.106	0.971 ± 0.045	1.279 ± 0.120
0.5-0.6	2.487 ± 0.143	1.068 ± 0.061	1.546 ± 0.178

Table 6.8: $< p_T >$ (in GeV/c) and $< p_T^2 >$ (in GeV^2/c^2) for π^-+W Drell-Yan in different mass and x_F bins for E537 experiment

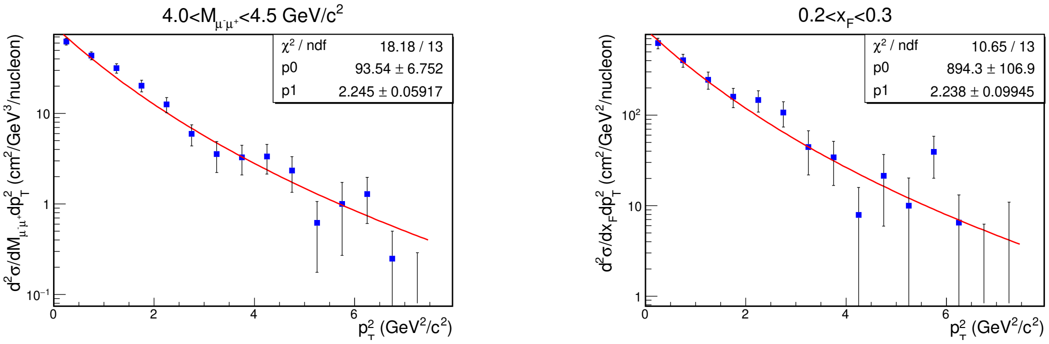

(a) Kaplan fit to E537 pion data in $M_{\mu^-\mu^+}$=4-4.5 GeV/c^2 bin.

(b) Kaplan fit to E537 pion data in x_F=0.2-0.3 bin.

Figure 6.6

- E615 $\pi^- + W \to \mu^+ + \mu^- + X$ at 252 GeV/c

  $d^2\sigma/dmdp_T$ (in units $cm^2/GeV/nucleon$) and $d^2\sigma/dxdp_T$ (in units $cm^2/GeV/nucleon$) as a function of p_T is tabulated for different mass bins and x_F bins [36]. The tabulated cross section was divided by $2p_T$ to get the cross section as $d^2\sigma/dmdp_T^2$ and $d^2\sigma/dxdp_T^2$. The p_T distribution was analysed in each mass and x_F bin to obtain the mean p_T. The result is tabulated in table 6.9

M	$\sqrt{\tau}$	p_1	$< p_T >$	$< p_T^2 >$
4.05-4.50	.19	2.553 ± 0.015	1.09 ± .01	1.63 ± 0.02
4.50-4.95	.22	2.607 ± 0.019	1.11 ± .01	1.70 ± 0.02
4.95-5.40	.24	2.645 ± 0.022	1.14 ± .01	1.75 ± 0.03
5.40-5.85	.26	2.737 ± 0.031	1.17 ± .01	1.87 ± 0.04
5.85-6.75	.29	2.723 ± 0.031	1.16 ± .01	1.85 ± 0.04
6.75-7.65	.33	2.685 ± 0.043	1.15 ± .01	1.80 ± 0.06
7.65-9.00	.38	2.805 ± 0.045	1.20 ± .01	1.96 ± 0.06
9.00-10.35	.44	2.587 ± 0.056	1.11 ± .02	1.67 ± 0.07
10.35-11.70	.51	2.660 ± 0.138	1.14 ± .06	1.77 ± 0.18
11.70-13.05	.57	2.475 ± 0.252	1.06 ± .12	1.53 ± 0.31

x_F	p_1	$< p_T >$	$< p_T^2 >$
0.00-0.10	2.67 ± 0.05	1.14 ± .02	1.78 ± 0.07
0.10-0.20	2.70 ± 0.04	1.16 ± .01	1.82 ± 0.04
0.20-0.30	2.68 ± 0.03	1.15 ± .01	1.79 ± 0.04
0.30-0.40	2.75 ± 0.03	1.18 ± .01	1.89 ± 0.04
0.40-0.50	2.65 ± 0.02	1.14 ± .01	1.76 ± 0.03
0.50-0.60	2.54 ± 0.02	1.09 ± .01	1.62 ± 0.03
0.60-0.70	2.45 ± 0.02	1.05 ± .01	1.50 ± 0.02
0.70-0.80	2.31 ± 0.02	0.99 ± .01	1.33 ± 0.02
0.80-0.90	1.92 ± 0.03	0.82 ± .01	0.92 ± 0.02
0.90-1.00	1.37 ± 0.04	0.58 ± .01	0.46 ± 0.03

Table 6.9: $< p_T >$ (in GeV/c) and $< p_T^2 >$ (in GeV^2/c^2) for π^-+W Drell-Yan in different mass and x_F bins for E615 experiment

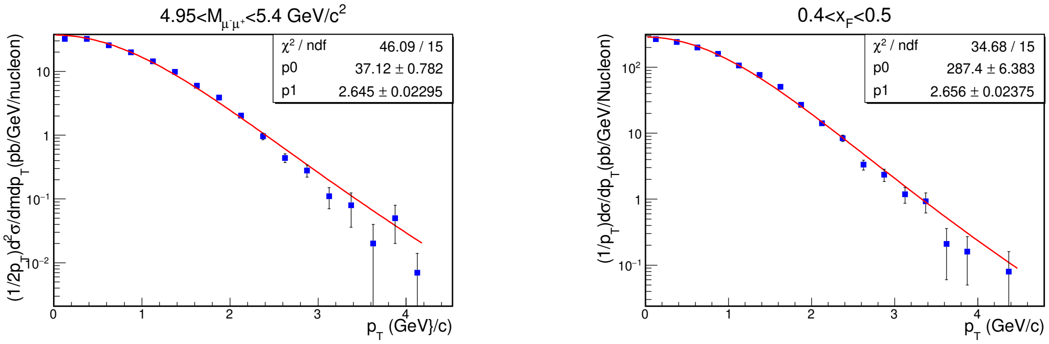

(a) Kaplan fit to E615 pion data in $M_{\mu^-\mu^+}$=4.95-5.4 GeV/c^2 bin.

(b) Kaplan fit to E615 pion data in x_F=0.4-0.5 bin.

Figure 6.7

- NA10 $\pi^- + W \rightarrow \mu^+ + \mu^- + X$ at 194/284 GeV/c

  $1/p_T d^3\sigma/dmdydp_T$ (in units $nb/GeV^3/nucleon$) as a function of p_T is tabulated for different mass bins and y bins [56]. The p_T distribution was analysed in each mass and y bin to obtain the mean p_T. The result is tabulated in table 6.10

M	p_1	$< p_T >$	$< p_T^2 >$	M	p_1	$< p_T >$	$< p_T^2 >$
$p_{\text{beam}=194GeV/c}$ $y = 0.0 - 0.2$				$p_{\text{beam}=284GeV/c}$ $y = 0.0 - 0.2$			
$4.5 - 5.5$	2.36 ± 0.02	$1.01 \pm .00$	1.39 ± 0.02	$4.5 - 5.5$	2.76 ± 0.02	$1.18 \pm .01$	1.90 ± 0.03
$5.5 - 6.5$	2.64 ± 0.02	$1.13 \pm .00$	1.74 ± 0.02	$5.5 - 6.5$	2.86 ± 0.03	$1.22 \pm .01$	2.04 ± 0.04
$6.5 - 7.5$	2.72 ± 0.03	$1.17 \pm .01$	1.85 ± 0.04	$6.5 - 7.5$	2.98 ± 0.04	$1.28 \pm .02$	2.21 ± 0.06
$7.5 - 8.5$	2.62 ± 0.02	$1.12 \pm .01$	1.72 ± 0.04	$7.5 - 8.5$	2.91 ± 0.06	$1.25 \pm .02$	2.11 ± 0.08
$11 - 15$	2.58 ± 0.4	$1.11 \pm .17$	1.67 ± 0.52	$11 - 15$	2.68 ± 0.13	$1.15 \pm .06$	1.80 ± 0.18
$y = 0.2 - 0.4$				$y = 0.2 - 0.4$			
$4.5 - 5.5$	2.60 ± 0.00	$1.12 \pm .00$	1.70 ± 0.01	$4.5 - 5.5$	2.80 ± 0.02	$1.20 \pm .00$	1.95 ± 0.03
$5.5 - 6.5$	2.66 ± 0.01	$1.14 \pm .00$	1.76 ± 0.02	$5.5 - 6.5$	2.92 ± 0.03	$1.25 \pm .01$	2.12 ± 0.04
$6.5 - 7.5$	2.65 ± 0.02	$1.14 \pm .00$	1.76 ± 0.02	$6.5 - 7.5$	2.86 ± 0.04	$1.23 \pm .02$	2.05 ± 0.06
$7.5 - 8.5$	2.66 ± 0.03	$1.14 \pm .01$	1.76 ± 0.04	$7.5 - 8.5$	2.99 ± 0.06	$1.28 \pm .02$	2.24 ± 0.08
$11 - 15$	2.66 ± 0.12	$1.14 \pm .05$	1.77 ± 0.16	$11 - 15$	2.83 ± 0.14	$1.22 \pm .06$	2.00 ± 0.20
$y = 0.4 - 0.6$				$y = 0.4 - 0.6$			
$4.5 - 5.5$	2.62 ± 0.01	$1.12 \pm .00$	1.72 ± 0.01	$4.5 - 5.5$	2.72 ± 0.02	$1.17 \pm .01$	1.86 ± 0.04
$5.5 - 6.5$	2.64 ± 0.02	$1.13 \pm .00$	1.74 ± 0.02	$5.5 - 6.5$	2.85 ± 0.04	$1.22 \pm .01$	2.03 ± 0.05
$6.5 - 7.5$	2.60 ± 0.02	$1.12 \pm .00$	1.68 ± 0.02	$6.5 - 7.5$	2.90 ± 0.05	$1.24 \pm .02$	2.10 ± 0.08
$7.5 - 8.5$	2.61 ± 0.04	$1.12 \pm .02$	1.70 ± 0.04	$7.5 - 8.5$	2.90 ± 0.07	$1.24 \pm .03$	2.10 ± 0.10
$11 - 15$	2.38 ± 0.2	$1.02 \pm .08$	1.42 ± 0.24	$11 - 15$	2.94 ± 0.37	$1.26 \pm .16$	2.17 ± 0.55

Table 6.10: $< p_T >$ (in GeV/c) and $< p_T^2 >$ (in GeV^2/c^2) for pi^-+W Drell-Yan in different M and y bins for two different beam energies.

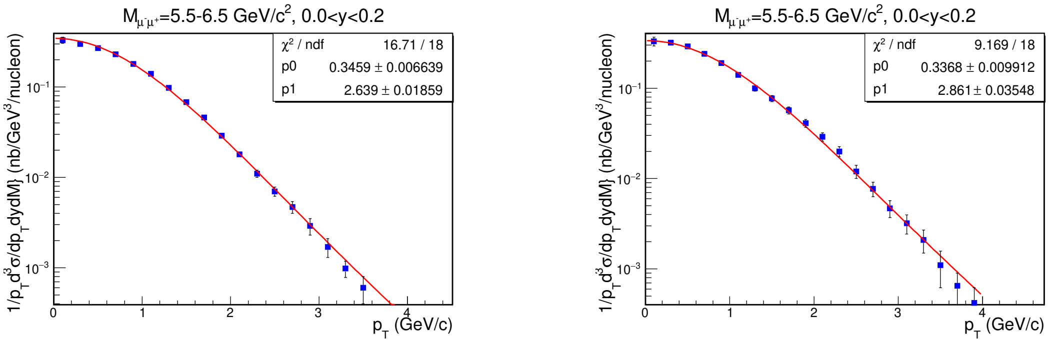

(a) Kaplan fit to NA10 194 GeV pion data in $M_{\mu^-\mu^+}$=5.5-6.5 GeV and y=0.0-0.2.

(b) Kaplan fit to NA10 284 GeV pion data in $M_{\mu^-\mu^+}$=5.5-6.5 GeV and y=0.0-0.2..

Figure 6.8

6.3 $\sqrt{s}$ dependence of $< p_T >$

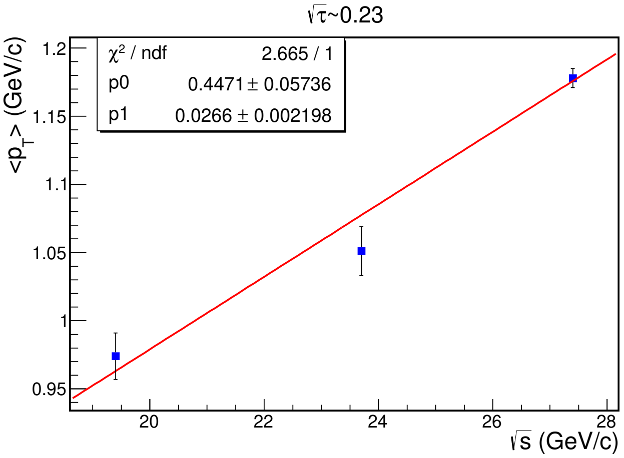

Figure 6.9: $< p_T >$ plotted as a function of $\sqrt{s}$ at $\sqrt{\tau} \sim 0.23$ for E288. The data points correspond to the highlighted rows in table 6.5. The points are fit with a straight line, $0.45 + 0.027\sqrt{s}$. The $< p_T >$ is increasing with $\sqrt{s}$. However, it should be noted that the corresponding x_F values are also decreasing; data from E866 show increase in p_T with decreasing x_F.

The results shown in figure 6.9 have been taken from E288 data at three different beam energies for similar values of scaling variable $\sqrt{\tau}$. Similar plots have been presented in various references [24, 54, 6, 5]. The constant term in the linear fit is interpreted as coming from the intrinsic transverse momentum of the quarks k_T. In Kenyon's paper $\sqrt{s}$ dependence of $< p_T >$ has also been reported for E288 data combined with Omega collaboration data for $\sqrt{\tau}= 0.22$ [24]. The fit parameters are $0.45 + 0.025\sqrt{s}$ similar to the results shown in 6.9. Additionally, results exist from a conference presentation by Corden *et. al.* [57] for $\sqrt{\tau}$ $= 0.28$. According to this result, $< p_T >$ is fitted as $0.54 + 0.029\sqrt{s}$. The constant term is slightly higher for $\sqrt{\tau} = 0.28$.

6.4 M dependence of $< p_T >$

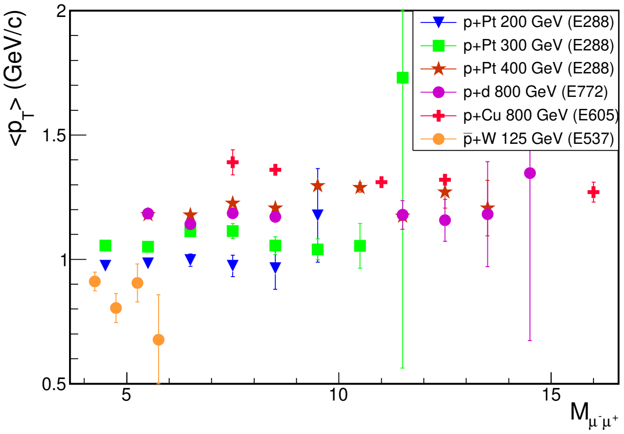

(a) Proton-induced Drell-Yan

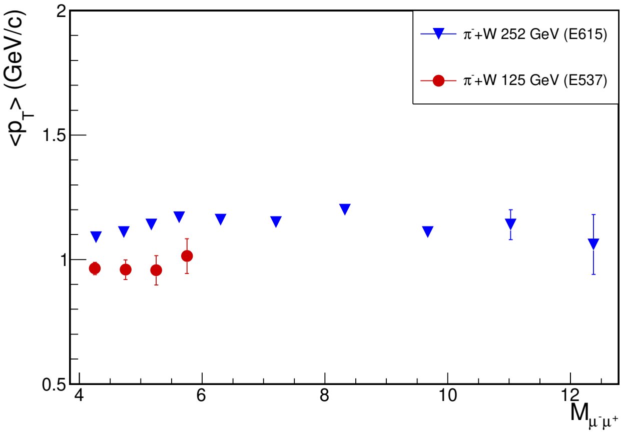

(b) Pion-induced Drell-Yan

Figure 6.10: The $< p_T >$ obtained in different $M_{\mu^-\mu^+}$ bin plotted as a function of $M_{\mu^-\mu^+}$. The different colors correspond to data from various experiments. The top plot is for proton and antiproton induced Drell Yan measurements. The bottom plot shows data from pion induced Drell Yan measurements. The data does not show any clear dependence on $M_{\mu^-\mu^+}$.

The results does not show significant mass dependence. However, there are some interesting features shown in figure 6.10a and 6.10b. Firstly as the beam energy increases the $< p_T >$ value increases. Secondly, the heavier targets have higher $< p_T >$. Results from several experiments have shown the effect of p_T broadening in heavier targets [58, 59, 60]

6.5 x_F dependence of $< p_T >$

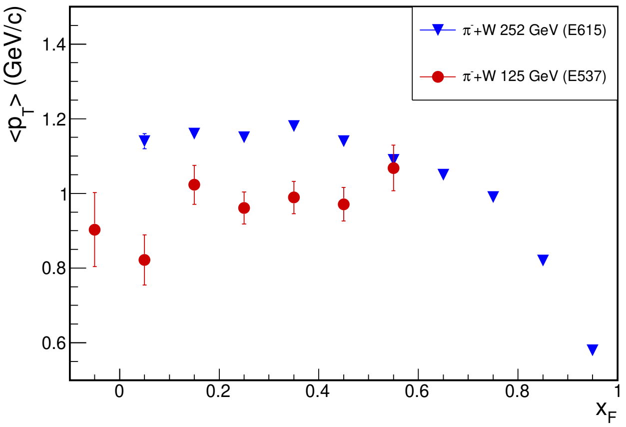

Figure 6.11: $< p_T >$ as a function of x_F obtained by analysing pion induced Drell-Yan data from E615 and E537.

The $< p_T >$ was first shown to have x_F dependence by pion induced Drell-Yan experiment E615 [36]. The $< p_T >$ is flat up to $x_F \sim 0.4$. Beyond $x_F \sim 0.4$ there is a strong dependence on x_F. Pion data from E537 is extending only up to 0.6 and also have poor statistics. Analysis of E866 data shows a similar strong dependence of $< p_T >$ on x_F. This result is observed for first time for proton induced Drell-Yan. A hand waving argument for understanding this trend is that as x_F ($\sim 2p_l/\sqrt{s}$) increases, the total centre of mass energy is used up in the longitudinal momentum, hence the transverse component of the momentum

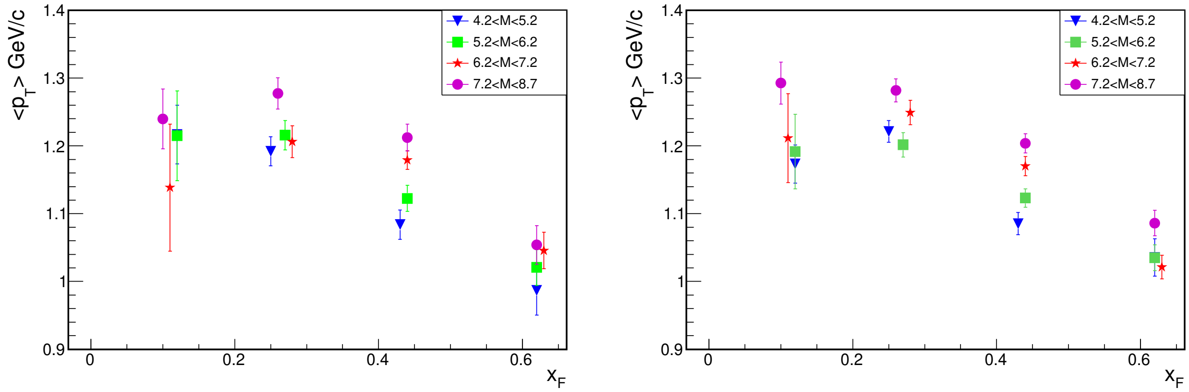

(a) $< p_T >$ plotted as function of x_F for LH_2 target

(b) $< p_T >$ plotted as function of x_F for LD_2 target

Figure 6.12: The $< p_T >$ obtained in different $M_{\mu^-\mu^+}$ and x_F bin from E866 [4] plotted as a function of x_F. The data clearly shows decrease in $< p_T >$ with increasing x_F. The different colors correspond to different mass bins. For low x_F values the $< p_T >$ does not seem to have any mass dependence. However, for higher x_F bins, $< p_T >$ is increasing with $M_{\mu^-\mu^+}$.

decreases. This trend is supported by NLO calculation performed by Ching-Him Leung [61].

6.6 Beam-type dependence of p_T

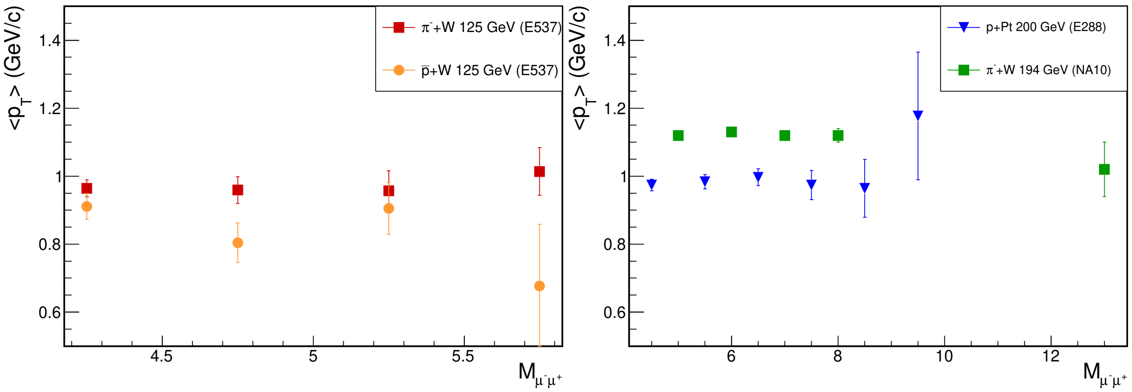

Figure 6.13: The $< p_T >$ obtained in different $M_{\mu^-\mu^+}$ bin is plotted as a function of x_F for π^-, $\bar{p}$ and p beam at comparable beam energies. The left figure shows a comparison of $< p_T >$ from 125 GeV π^- and $\bar{p}$ beam induced Drell-Yan. Right figure shows a comparison of $< p_T >$ for 200 GeV p and 194 GeV π^- beam induced Drell-Yan.

At similar beam energy, the $< p_T >$ for π induced Drell-Yan is higher as compared to the p induced Drell Yan, and $< p_T >$ for $\bar{p}$ is lower than π^-. The difference between antiproton and pion $< p_T >$ is not as significant. 120 GeV SeaQuest p_T data from $p + W$ interactions can add important information in understanding the dependence of p_T on beam type.

Chapter 7

Transverse momentum distribution from SeaQuest

7.1 Introduction

The study presented in this chapter was motivated by the analysis of existing Drell-Yan transverse momentum data described in chapter 6. It focusses on analysis of transverse momentum data from SeaQuest for LD_2 and LH_2. The centre of mass energy $\sqrt{s}$ = 15.01 GeV/c for SeaQuest experiment makes the transverse momentum data interesting as it is the lowest $\sqrt{s}$ amongst the existing Drell-Yan data. There are several exciting physics topics that can be studied from the SeaQuest data.

- Dependence of $< p_T >$ on $\sqrt{s}$
  The LD_2 and LH_2 data are analysed to get $< p_T >$ at $\sqrt{s}$=15.01 GeV. The SeaQuest data along with data from existing Drell-Yan experiments at similar values of scaling variable $\sqrt{\tau}$ is utilized to extrapolate the $< p_T >$ to the intercept value which is interpreted as originating from the intrinsic k_T of the quarks.

- Dependence of $< p_T >$ on x_F and M
  Study the possible dependence of $< p_T >$ on x_F and M. There is only one published result on possible dependence of p_T on x_F from pion induced Drell-Yan in E615 experiment[36]. Similar trend was also observed in unpublished E866 p+p and p+d data. The analysis from E866 p_T data is shown in chapter 6. SeaQuest data also exhibit similar behaviour (discussed in this chapter).

- Nuclear dependence of p_T distribution
  Studies are being done by other members in SeaQuest collaboration to obtain $\Delta < p_T^2 >$(=$< p_T^2 >_A$ $- < p_T^2 >_{LD2}$), which is the measure of broadening of p_T distribution (as compared to LD_2) in nuclear targets due to multiple scattering of quarks/anti-quarks in nuclear medium. Here A refers to the nuclear targets, Tungsten, Iron and Carbon. The expression of $\Delta < p_T^2 >$ requires information about $< p_T^2 >$ from LD_2. Hence, the methods and preliminary results presented in this chapter will be useful for studying the p_T broadening effects in nuclear targets.

7.2 Method

The methodology used for analysis is the same as described in chapter 4. The only difference is that the mass fit results are now projected onto p_T and the DY yield in each p_T bin is obtained as

$$N_{DY}(p_T) = N_{data} - N_{flask} - N_{J/\Psi} - N_{\Psi'} - N_{mixbkg}. \tag{7.1}$$

The yield in each bin is corrected for acceptance in that p_T bin.

7.3 Results

7.3.1 p_T distribution for Deuterium and Hydrogen data integrated over all x_F and M range

p_T bin (GeV)	$d\sigma/dp_T(\times 10^{-2})$	Stat. error$(\times 10^{-2})$
0.00-0.25	0.300513	0.009203
0.25-0.50	0.785850	0.015833
0.50-0.75	1.036640	0.019370
0.75-1.00	0.968041	0.020953
1.00-1.25	0.696715	0.021366
1.25-1.50	0.423877	0.022389
1.50-1.75	0.222041	0.025673
1.75-2.00	0.167534	0.023301
2.00-2.25	0.065445	0.028757

Table 7.1: p+d Drell-Yan p_T distribution (in nb/GeV) for $x_F = (-0.1, 0.95)$ and $M = (4.2\text{ GeV}, 8.8\text{ GeV})$

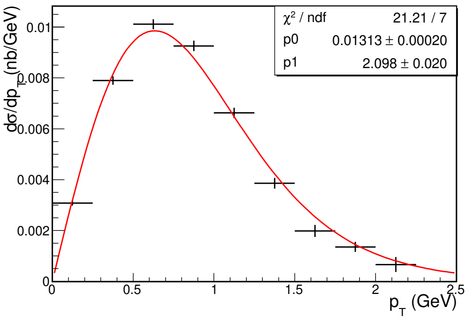

Figure 7.1: Kaplan fit to p+d data for $x_F = (-0.1, 0.95)$ and $M = (4.2\text{ GeV}, 8.8\text{ GeV})$. The $< p_T >$ value obtained from the fit using equation 6.7 is 0.901 ± 0.008 GeV.

p_T bin (GeV)	$d\sigma/dp_T(\times10^{-2})$	Stat. error$(\times10^{-2})$
0.00-0.25	0.142483	0.005122
0.25-0.50	0.355969	0.008761
0.50-0.75	0.456982	0.011045
0.75-1.00	0.431939	0.011965
1.00-1.25	0.309736	0.013173
1.25-1.50	0.167725	0.014260
1.50-1.75	0.104554	0.015176
1.75-2.00	0.088655	0.014923
2.00-2.25	0.008963	0.017207

Table 7.2: p+p Drell-Yan p_T distribution (in nb/GeV) for $x_F = (-0.1, 0.95)$ and $M = (4.2\text{ GeV}, 8.8\text{ GeV})$

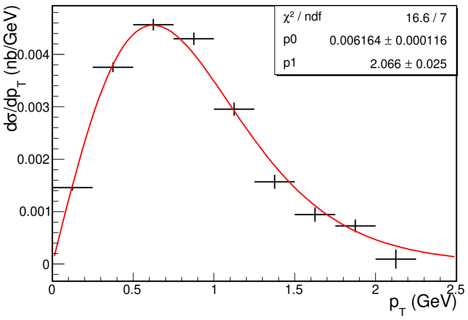

Figure 7.2: Kaplan fit to p+p data for $x_F = (-0.1, 0.95)$ and $M = (4.2\text{ GeV}, 8.8\text{ GeV})$. The $< p_T >$ value obtained from the fit using equation 6.7 is 0.887 ± 0.011 GeV.

The mean p_T obtained is plotted below as a function of $\sqrt{s}$ including data from E288 for similar value of $\sqrt{\tau} \sim 0.32 \pm 0.01$.

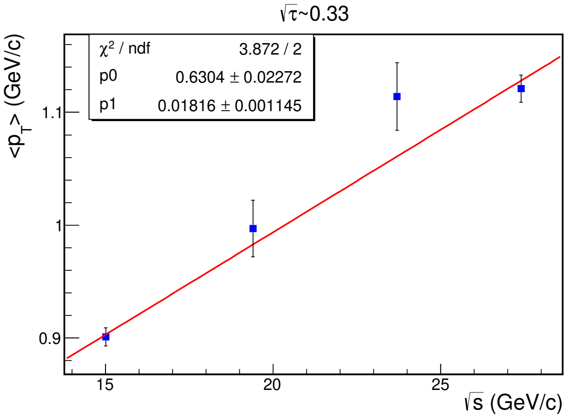

Figure 7.3: $< p_T >$ plotted as a function of $\sqrt{s}$ at $\sqrt{\tau} \sim 0.32 - 0.33$ for E906 (lowest $\sqrt{s}$) and E288. The data points for E288 are taken from analysis of E288 transverse momentum data (table 6.5). The data are fit using a linear function, resulting in straight line given by $0.63 + 0.018\sqrt{s}$. The $< p_T >$ is increasing with $\sqrt{s}$.

7.3.2 p_T distribution for Deuterium and Hydrogen data in different x_F bins

This section presents results from analysis of transverse momentum data for LD_2 and LH_2 in four x_F bins.

Deuterium

p_T bin (GeV)	$d\sigma/dp_T(\times 10^{-2})$	Stat. error$(\times 10^{-2})$
0.00-0.25	0.092351	0.011926
0.25-0.50	0.214132	0.020709
0.50-0.75	0.292736	0.024647
0.75-1.00	0.311301	0.032344
1.00-1.25	0.230786	0.037882
1.25-1.50	0.126533	0.039617
1.50-1.75	0.058446	0.043752
1.75-2.00	0.103070	0.036111
2.00-2.25	0.016981	0.056746

Table 7.3: p+d Drell-Yan p_T distribution (in nb/GeV) for $x_F = (-0.1, 0.15)$ and $M = (4.2\text{ GeV}, 8.8\text{ GeV})$

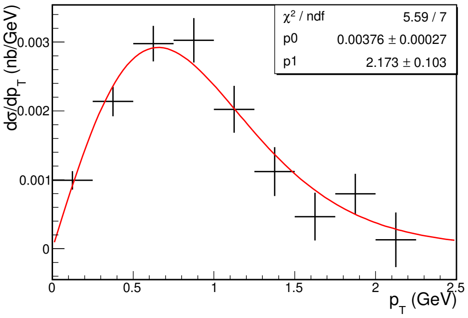

Figure 7.4: Kaplan fit to p+d data for $x_F = (-0.1, 0.15)$ and $M = (4.2\text{ GeV}, 8.8\text{ GeV})$.The $< p_T >$ value obtained from the fit using equation 6.7 is 0.933 ± 0.044 GeV.

p_T bin (GeV)	$d\sigma/dp_T(\times 10^{-2})$	Stat. error$(\times 10^{-2})$
0.00-0.25	0.089811	0.005829
0.25-0.50	0.234177	0.009467
0.50-0.75	0.319816	0.012089
0.75-1.00	0.276019	0.012431
1.00-1.25	0.184998	0.012846
1.25-1.50	0.107834	0.014568
1.50-1.75	0.052784	0.020219
1.75-2.00	0.062100	0.016540
2.00-2.25	0.025087	0.018614

Table 7.4: p+d Drell-Yan p_T distribution (in nb/GeV) for $x_F = [0.15, 0.35)$ and $M = (4.2\text{ GeV}, 8.8\text{ GeV})$

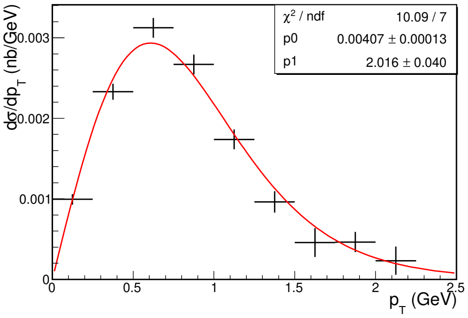

Figure 7.5: Kaplan fit to p+d data for $x_F = [0.15, 0.35)$ and $M = (4.2\text{ GeV}, 8.8\text{ GeV})$.The $< p_T >$ value obtained from the fit using equation 6.7 is 0.865 ± 0.017 GeV.

p_T bin (GeV)	$d\sigma/dp_T(\times 10^{-2})$	Stat. error$(\times 10^{-2})$
0.00-0.25	0.068699	0.003384
0.25-0.50	0.180572	0.005832
0.50-0.75	0.228834	0.006734
0.75-1.00	0.207071	0.006939
1.00-1.25	0.155051	0.006632
1.25-1.50	0.082505	0.006087
1.50-1.75	0.039961	0.005207
1.75-2.00	0.024352	0.004681
2.00-2.25	0.010615	0.006676

Table 7.5: p+d Drell-Yan p_T distribution (in nb/GeV) for $x_F = [0.35, 0.55)$ and $M = (4.2\text{ GeV}, 8.8\text{ GeV})$

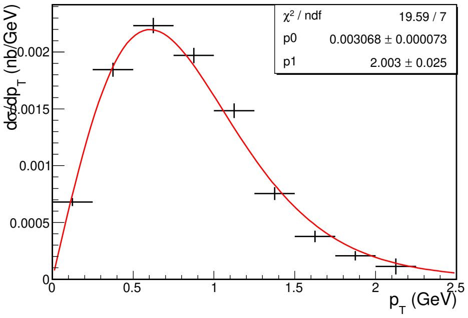

Figure 7.6: Kaplan fit to p+d data for $x_F = [0.35, 0.55)$ and $M = (4.2\text{ GeV}, 8.8\text{ GeV})$. The $< p_T >$ value obtained from the fit using equation 6.7 is 0.860 ± 0.011 GeV.

p_T bin (GeV)	$d\sigma/dp_T(\times 10^{-2})$	Stat. error$(\times 10^{-2})$
0.00-0.25	0.030706	0.001555
0.25-0.50	0.077741	0.002696
0.50-0.75	0.092259	0.003088
0.75-1.00	0.084207	0.002979
1.00-1.25	0.048255	0.002572
1.25-1.50	0.031740	0.002275
1.50-1.75	0.015347	0.002091
1.75-2.00	0.007392	0.002321
2.00-2.25	0.001709	0.001870

Table 7.6: p+d Drell-Yan p_T distribution (in nb/GeV) for $x_F = [0.55, 0.8)$ and $M = (4.2\text{ GeV}, 8.8\text{ GeV})$

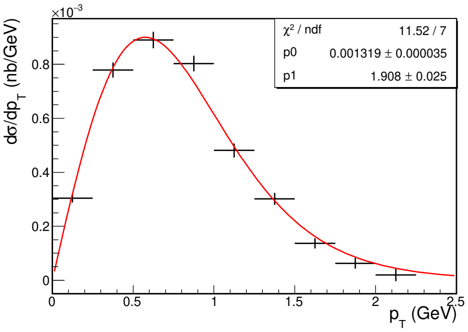

Figure 7.7: Kaplan fit to p+d data for $x_F = [0.55, 0.8)$ and $M = (4.2\text{ GeV}, 8.8\text{ GeV})$. The $< p_T >$ value obtained from the fit using equation 6.7 is 0.819 ± 0.011 GeV.

Hydrogen

p_T bin (GeV)	$d\sigma/dp_T(\times 10^{-2})$	Stat. error$(\times 10^{-2})$
0.00-0.25	0.048919	0.007188
0.25-0.50	0.110836	0.011941
0.50-0.75	0.138999	0.015179
0.75-1.00	0.113862	0.017659
1.00-1.25	0.072359	0.021387
1.25-1.50	0.022840	0.026644
1.50-1.75	-0.006597	0.029923
1.75-2.00	0.067248	0.022022
2.00-2.25	-0.032670	0.062112

Table 7.7: p+p Drell-Yan p_T distribution (in nb/GeV) for $x_F = (-0.1, 0.15)$ and $M = (4.2\text{ GeV}, 8.8\text{ GeV})$

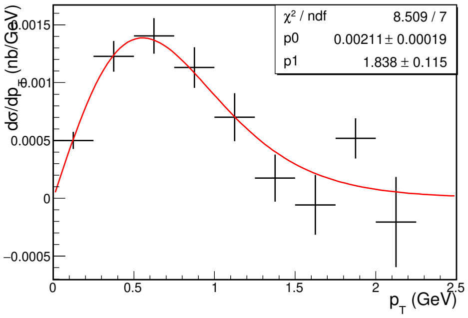

Figure 7.8: Kaplan fit to p+p data for $x_F = (-0.1, 0.15)$ and $M = (4.2\text{ GeV}, 8.8\text{ GeV})$. The $< p_T >$ value obtained from the fit using equation 6.7 is 0.789 ± 0.05 GeV.

p_T bin (GeV)	$d\sigma/dp_T(\times 10^{-2})$	Stat. error$(\times 10^{-2})$
0.00-0.25	0.038017	0.002900
0.25-0.50	0.099680	0.004893
0.50-0.75	0.123768	0.006093
0.75-1.00	0.123017	0.007036
1.00-1.25	0.078648	0.007820
1.25-1.50	0.038177	0.008078
1.50-1.75	0.022717	0.009679
1.75-2.00	0.015798	0.009034
2.00-2.25	0.006599	0.008475

Table 7.8: p+p Drell-Yan p_T distribution (in nb/GeV) for $x_F = [0.15, 0.35)$ and $M = (4.2\text{ GeV}, 8.8\text{ GeV})$

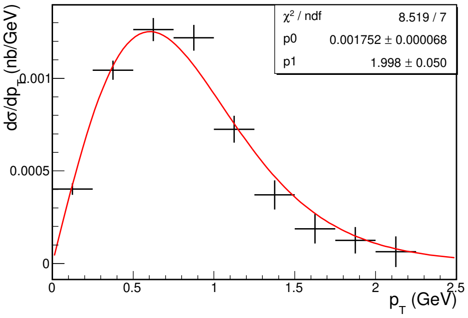

Figure 7.9: Kaplan fit to p+p data for $x_F = [0.15, 0.35)$ and $M = (4.2\text{ GeV}, 8.8\text{ GeV})$. The $< p_T >$ value obtained from the fit using equation 6.7 is 0.858 ± 0.021 GeV.

p_T bin (GeV)	$d\sigma/dp_T(\times10^{-2})$	Stat. error$(\times10^{-2})$
0.00-0.25	0.031526	0.001792
0.25-0.50	0.075037	0.002917
0.50-0.75	0.095177	0.003503
0.75-1.00	0.080764	0.003459
1.00-1.25	0.061081	0.003511
1.25-1.50	0.029939	0.003605
1.50-1.75	0.019028	0.003274
1.75-2.00	0.018280	0.003014
2.00-2.25	-0.001256	0.003721

Table 7.9: p+p Drell-Yan p_T distribution (in nb/GeV) for $x_F = [0.35, 0.55)$ and $M = (4.2\text{ GeV}, 8.8\text{ GeV})$

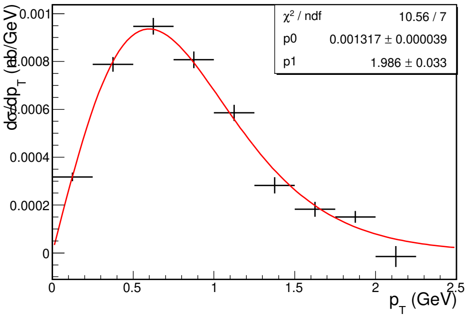

Figure 7.10: Kaplan fit to p+p data for $x_F = [0.35, 0.55)$ and $M = (4.2\text{ GeV}, 8.8\text{ GeV})$. The $< p_T >$ value obtained from the fit using equation 6.7 is 0.853 ± 0.014 GeV.

p_T bin (GeV)	$d\sigma/dp_T(\times10^{-2})$	Stat. error$(\times10^{-2})$
0.00-0.25	0.012958	0.000796
0.25-0.50	0.030805	0.001370
0.50-0.75	0.038426	0.001721
0.75-1.00	0.035560	0.001560
1.00-1.25	0.021979	0.001491
1.25-1.50	0.013384	0.001303
1.50-1.75	0.006772	0.001194
1.75-2.00	0.002430	0.001220
2.00-2.25	0.001467	0.000885

Table 7.10: p+p Drell-Yan p_T distribution (in nb/GeV) for $x_F = [0.55, 0.8)$ and $M = (4.2\text{ GeV}, 8.8\text{ GeV})$

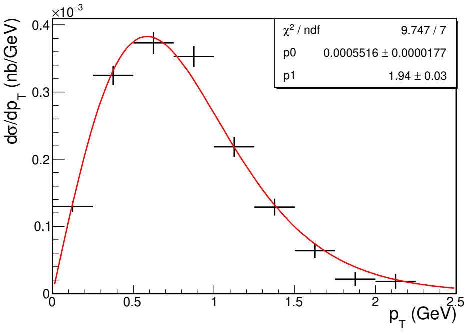

Figure 7.11: Kaplan fit to p+p data for $x_F = [0.55, 0.8)$ and $M = (4.2\text{ GeV}, 8.8\text{ GeV})$. The $< p_T >$ value obtained from the fit using equation 6.7 is 0.833 ± 0.013 GeV.

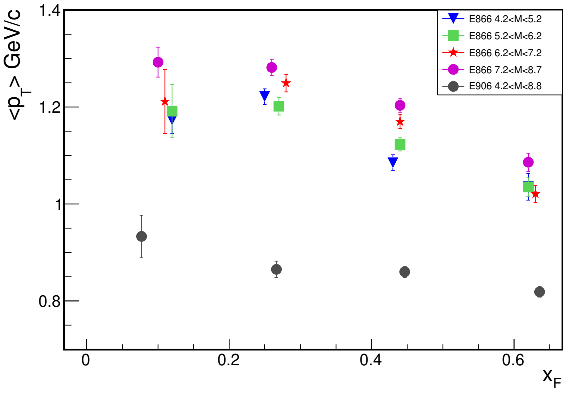

Figure 7.12: x_F dependence of $< p_T >$ for SeaQuest p+d data. It is compared with p+d data from E866. The SeaQuest $< p_T >$ is expected to be lower than E866 because of lower $\sqrt{s}$.

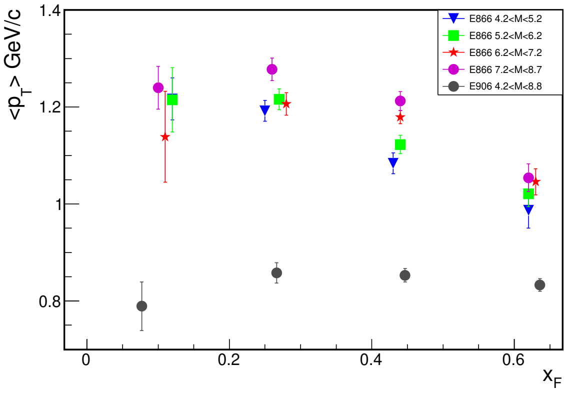

Figure 7.13: x_F dependence of $< p_T >$ for SeaQuest p+p data. It is compared with p+p data from E866. The SeaQuest $< p_T >$ is expected to be lower than E866 because of lower $\sqrt{s}$.

Differential cross section $d\sigma/dp_T$ were calculated in four x_F bins using the NLO code [42] to check any systematic dependence of $< p_T >$ on x_F. The NLO code used for this calculation does not take care of infrared divergences at low p_T region arising in the QCD calculation. Hence, while fitting the p_T distribution from NLO calculation, low p_T region has been ignored. To get better estimate of p_T distribution shape, especially at low p_T, the resummation code provided in [62] should be used.

Figure 7.14 and 7.15 shows $d\sigma/dp_T$ in four x_F bins. The calculation was performed at $\sqrt{s}$=15.01 GeV with mass cut from 4.2 GeV to 8.8 GeV. The fit result (p_1) shows decrease with increasing x_F.

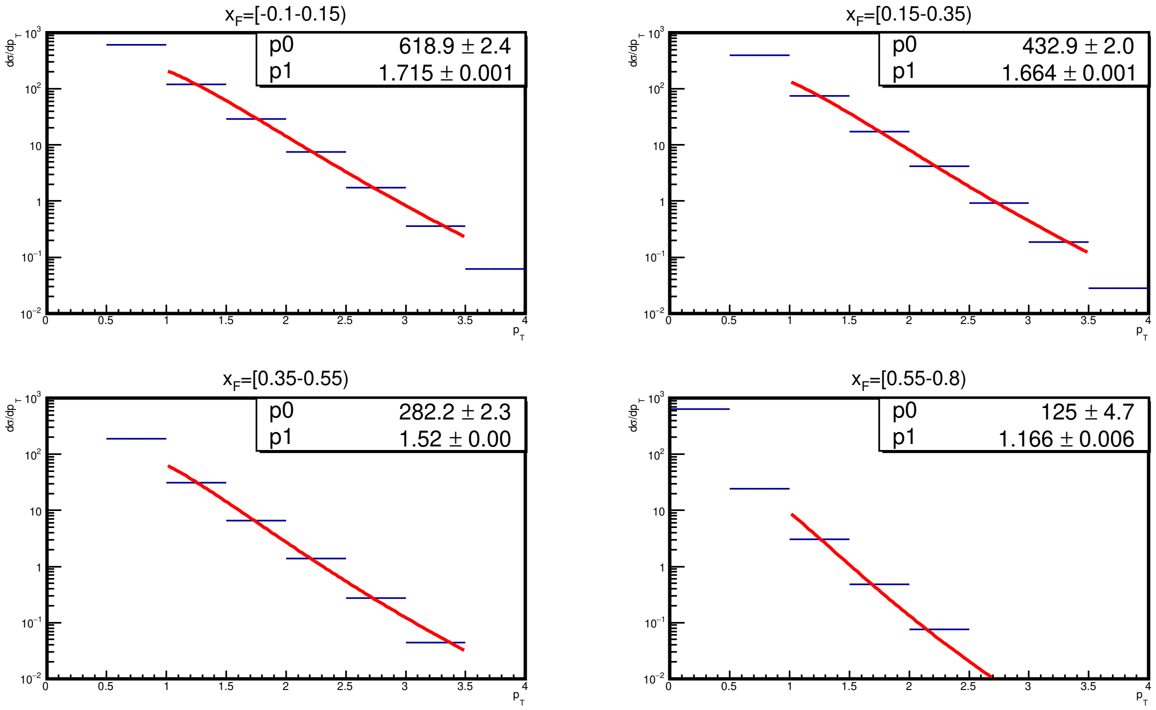

Figure 7.14: p_T distribution from p+d NLO calculation in different x_F bins also suggest dependence of $< p_T >$ on x_F. The distribution with Kaplan functional form in p_T range 1 GeV-3.5 GeV.

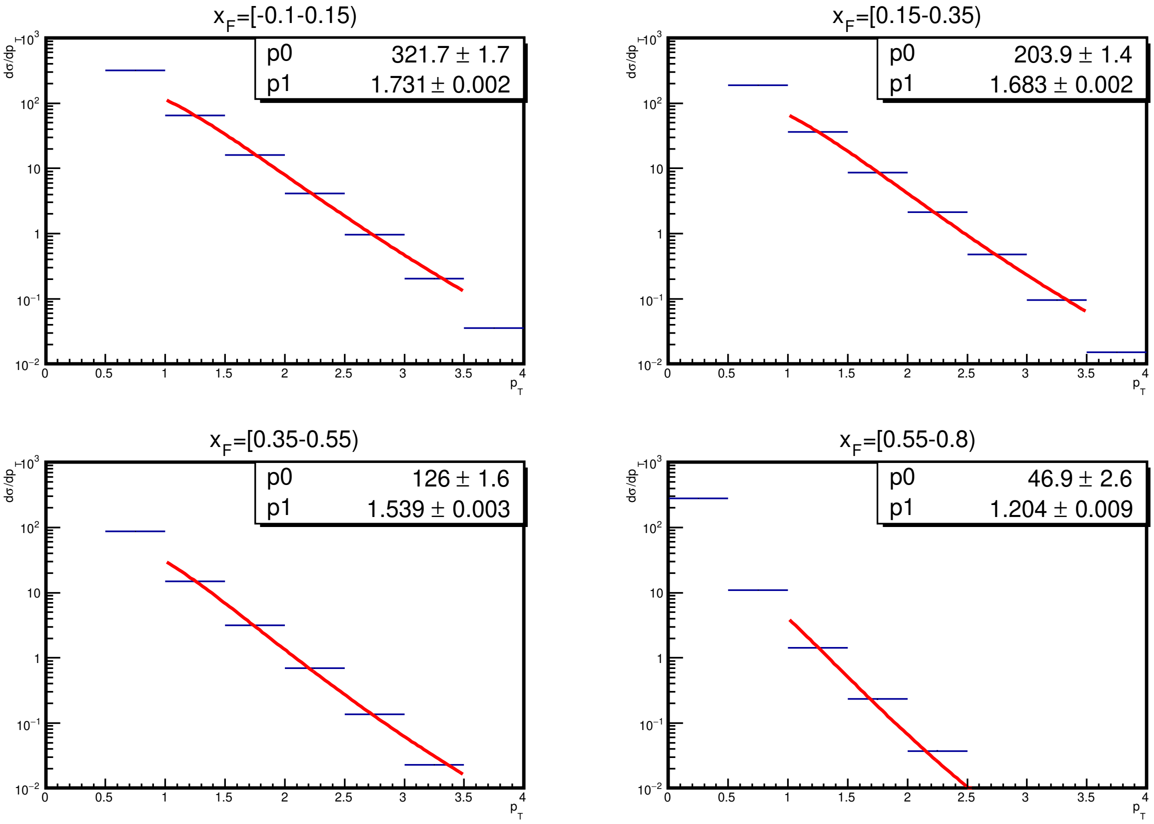

Figure 7.15: p_T distribution from p+p NLO calculation in different x_F bins also suggest dependence of $< p_T >$ on x_F. The distribution with Kaplan functional form in p_T range 1 GeV-3.5 GeV.

7.3.3 p_T distribution for Deuterium and Hydrogen data in different M bins

This section presents results from analysis of transverse momentum data for LD_2 and LH_2 in four M bins.

Deuterium

p_T bin (GeV)	$d\sigma/dp_T(\times 10^{-2})$	Stat. error$(\times 10^{-2})$
0.00-0.25	0.264061	0.010992
0.25-0.50	0.684132	0.019016
0.50-0.75	0.873793	0.022824
0.75-1.00	0.791620	0.024096
1.00-1.25	0.582572	0.025095
1.25-1.50	0.287964	0.026624
1.50-1.75	0.156116	0.032908
1.75-2.00	0.141301	0.025983
2.00-2.25	0.067996	0.056541

Table 7.11: p+d Drell-Yan p_T distribution (in nb/GeV) for $M = (4.2\text{ GeV}, 5.2\text{ GeV})$ and $x_F = (-0.1, 0.95)$

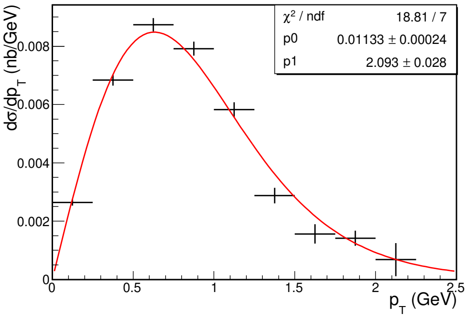

Figure 7.16: Kaplan fit to data for $M = (4.2\text{ GeV}, 5.2\text{ GeV})$ and $x_F = (-0.1, 0.95)$. The $< p_T >$ value obtained from the fit using equation 6.7 is 0.898 ± 0.012 GeV.

p_T bin (GeV)	$d\sigma/dp_T(\times 10^{-2})$	Stat. error$(\times 10^{-2})$
0.00-0.25	0.039243	0.002121
0.25-0.50	0.104561	0.003473
0.50-0.75	0.135456	0.004080
0.75-1.00	0.128306	0.004433
1.00-1.25	0.088042	0.004512
1.25-1.50	0.061142	0.004034
1.50-1.75	0.029735	0.004090
1.75-2.00	0.012515	0.004575
2.00-2.25	0.007154	0.004133

Table 7.12: p+d Drell-Yan p_T distribution (in nb/GeV) for $M = [5.2\text{ GeV}, 6.2\text{ GeV})$ and $x_F = (-0.1, 0.95)$

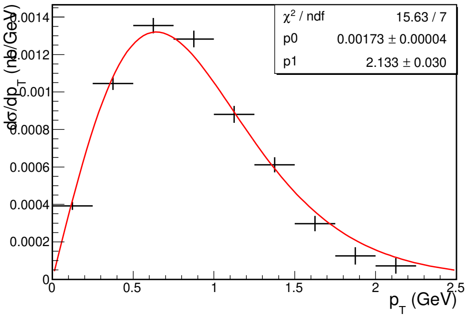

Figure 7.17: Kaplan fit to data for $M = [5.2\text{ GeV}, 6.2\text{ GeV})$ and $x_F = (-0.1, 0.95)$. The $< p_T >$ value obtained from the fit using equation 6.7 is 0.915 ± 0.005 GeV.

p_T bin (GeV)	$d\sigma/dp_T(\times 10^{-2})$	Stat. error$(\times 10^{-2})$
0.00-0.25	0.008068	0.000658
0.25-0.50	0.017078	0.001023
0.50-0.75	0.022509	0.001201
0.75-1.00	0.020400	0.001216
1.00-1.25	0.014321	0.001238
1.25-1.50	0.011451	0.001029
1.50-1.75	0.005381	0.000741
1.75-2.00	0.003925	0.000787
2.00-2.25	0.002381	0.000886

Table 7.13: p+d Drell-Yan p_T distribution (in nb/GeV) for $M = [6.2\text{ GeV}, 7.2\text{ GeV})$ and $x_F = (-0.1, 0.95)$

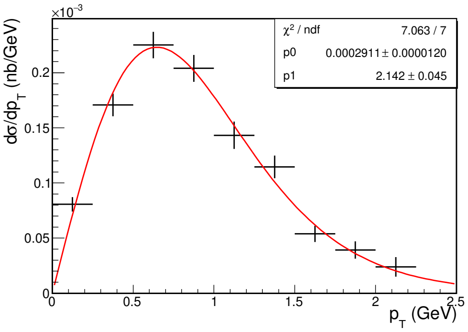

Figure 7.18: Kaplan fit to data for $M = [6.2\text{ GeV}, 7.2\text{ GeV})$ and $x_F = (-0.1, 0.95)$. The $< p_T >$ value obtained from the fit using equation 6.7 is 0.919 ± 0.019 GeV.

p_T bin (GeV)	$d\sigma/dp_T(\times 10^{-2})$	Stat. error$(\times 10^{-2})$
0.00-0.25	0.001546	0.000307
0.25-0.50	0.003124	0.000461
0.50-0.75	0.003387	0.000528
0.75-1.00	0.003820	0.000542
1.00-1.25	0.002703	0.000488
1.25-1.50	0.002435	0.000498
1.50-1.75	0.001408	0.000363
1.75-2.00	0.000329	0.000205
2.00-2.25	-0.000009	0.000009

Table 7.14: p+d Drell-Yan p_T distribution (in nb/GeV) for $M = [7.2\text{ GeV}, 8.8\text{ GeV})$ and $x_F = (-0.1, 0.95)$

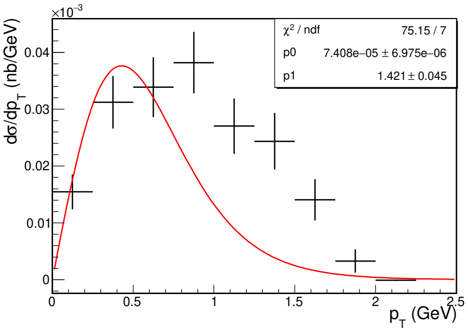

Figure 7.19: The fit for last mass bin failed.

Hydrogen

p_T bin (GeV)	$d\sigma/dp_T(\times 10^{-2})$	Stat. error$(\times 10^{-2})$
0.00-0.25	0.127478	0.005945
0.25-0.50	0.322851	0.010686
0.50-0.75	0.401092	0.012870
0.75-1.00	0.370814	0.014120
1.00-1.25	0.258507	0.014870
1.25-1.50	0.116959	0.017469
1.50-1.75	0.072334	0.018552
1.75-2.00	0.077520	0.016559
2.00-2.25	0.001606	0.025135

Table 7.15: p+p Drell-Yan p_T distribution (in nb/GeV) for $M = (4.2\text{ GeV}, 5.2\text{ GeV})$ and $x_F = (-0.1, 0.95)$

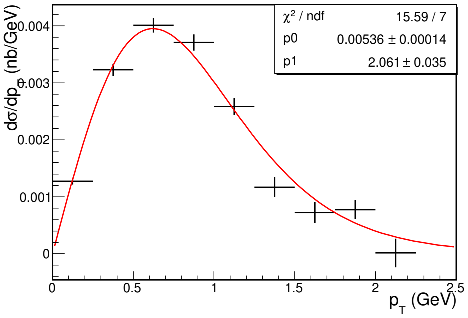

Figure 7.20: Kaplan fit to data for $M = (4.2\text{ GeV}, 5.2\text{ GeV})$ and $x_F = (-0.1, 0.95)$. The $< p_T >$ value obtained from the fit using equation 6.7 is 0.885 ± 0.015 GeV.

p_T bin (GeV)	$d\sigma/dp_T(\times 10^{-2})$	Stat. error$(\times 10^{-2})$
0.00-0.25	0.017936	0.001251
0.25-0.50	0.051063	0.002030
0.50-0.75	0.059694	0.002386
0.75-1.00	0.058268	0.002582
1.00-1.25	0.039750	0.002920
1.25-1.50	0.025379	0.002599
1.50-1.75	0.013370	0.002834
1.75-2.00	0.008073	0.002787
2.00-2.25	0.000062	0.004396

Table 7.16: p+p Drell-Yan p_T distribution (in nb/GeV) for $M = [5.2\text{ GeV}, 6.2\text{ GeV})$ and $x_F = (-0.1, 0.95)$

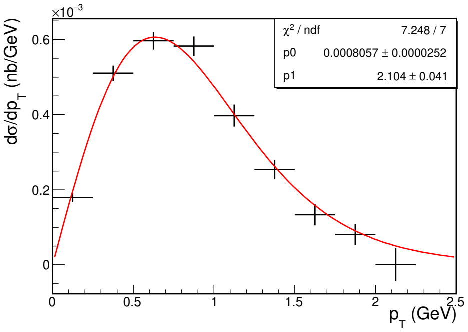

Figure 7.21: Kaplan fit to data for $M = [5.2\text{ GeV}, 6.2\text{ GeV})$ and $x_F = (-0.1, 0.95)$. The $< p_T >$ value obtained from the fit using equation 6.7 is 0.903 ± 0.018 GeV.

p_T bin (GeV)	$d\sigma/dp_T(\times 10^{-2})$	Stat. error$(\times 10^{-2})$
0.00-0.25	0.004014	0.000350
0.25-0.50	0.008714	0.000584
0.50-0.75	0.010414	0.000758
0.75-1.00	0.010062	0.000738
1.00-1.25	0.006590	0.000817
1.25-1.50	0.004697	0.000568
1.50-1.75	0.003419	0.000493
1.75-2.00	0.000913	0.000459
2.00-2.25	0.001506	0.000510

Table 7.17: p+p Drell-Yan p_T distribution (in nb/GeV) for $M = [6.2\text{ GeV}, 7.2\text{ GeV})$ and $x_F = (-0.1, 0.95)$

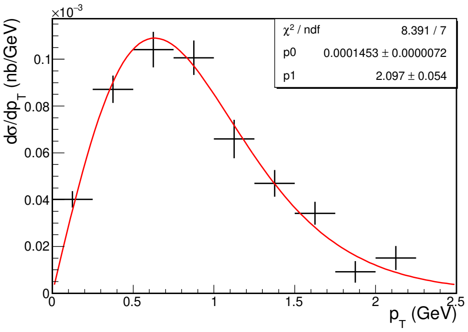

Figure 7.22: Kaplan fit to data for $M = [6.2\text{ GeV}, 7.2\text{ GeV})$ and $x_F = (-0.1, 0.95)$. The $< p_T >$ value obtained from the fit using equation 6.7 is 0.900 ± 0.023 GeV.

p_T bin (GeV)	$d\sigma/dp_T(\times 10^{-2})$	Stat. error$(\times 10^{-2})$
0.00-0.25	0.000569	0.000135
0.25-0.50	0.001112	0.000251
0.50-0.75	0.001419	0.000347
0.75-1.00	0.002038	0.000330
1.00-1.25	0.001411	0.000318
1.25-1.50	0.000924	0.000313
1.50-1.75	0.000650	0.000181
1.75-2.00	0.000437	0.000179
2.00-2.25	0.000152	0.000152

Table 7.18: p+p Drell-Yan p_T distribution (in nb/GeV) for $M = [7.2\text{ GeV}, 8.8\text{ GeV})$ and $x_F = (-0.1, 0.95)$

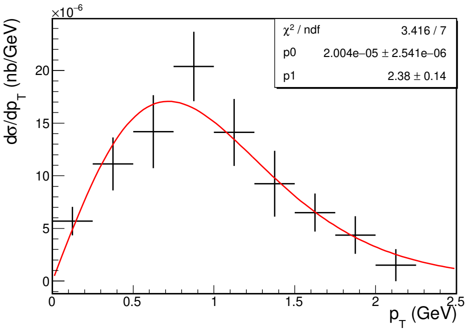

Figure 7.23: Kaplan fit to data for $M = [7.2\text{ GeV}, 8.8\text{ GeV})$ and $x_F = (-0.1, 0.95)$. The $< p_T >$ value obtained from the fit using equation 6.7 is 1.022 ± 0.06 GeV.

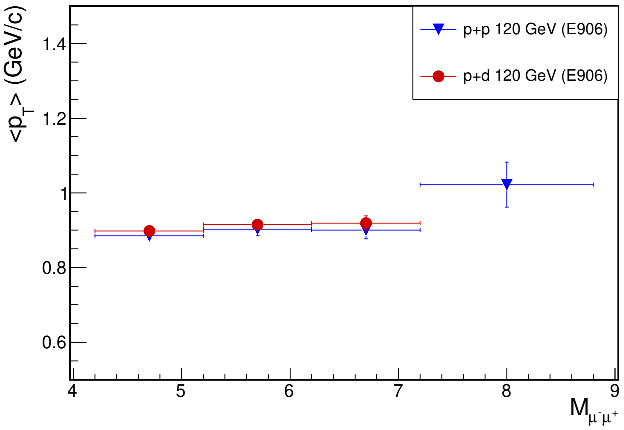

Figure 7.24: Calculated $< p_T >$ for p+p and p+d SeaQuest data plotted as a function of dimuon mass M.

Chapter 8

Discussion

In this chapter, the p+d cross section from SeaQuest is compared with existing DY cross section results from E866 (p+d) and E772 (p+d) data. Cross section ratio ($\sigma_{pd}/2\sigma_{pp}$) versus x_2 obtained from double differential absolute cross section in x_1 and x_2 is also presented.

8.1 Comparison with other experiments

The scaling form of Drell-Yan cross-section is useful in comparing experimental measurements at different $\sqrt{s}$. The right hand side of equation 8.1 depends on the value of x_B (x_1) and x_T (x_2) and the parton density function for a given set of x_B and x_T.

$$M^3 \frac{d^2\sigma}{dM dx_F} = \frac{8\pi\alpha^2}{9} \frac{x_B x_T}{x_B + x_T} \sum_i Q_i^2 [q_{i,B}(x_B)\bar{q}_{i,T}(x_T) + \bar{q}_{i,B}(x_B) q_{i,T}(x_T)] \tag{8.1}$$

For identical values of x_F ($= x_B - x_T$) and τ ($= x_B x_T$), irrespective of $\sqrt{s}$, the cross section $M^3 d^2\sigma/dM dx_F$ is predicted to be identical if scaling holds true. Figure 8.1 shows the scaling test results from CERN ISR experiment [5]. The CERN ISR measurements are at $\sqrt{s}$ = 44 GeV and 62 GeV. Within experimental uncertainty, the data from this experiment validate the scaling behaviour. Similarly, measurements from E288 experiment at three different $\sqrt{s}$ = 19.4, 23.8, and 27.4 GeV have been reported in [6, 21] (Figure 8.2) and within experimental uncertainty, the scaling behaviour is observed. Absolute cross sections from p+A interactions have also been measured in experiments such as NA3 (p+Pt at $\sqrt{s}$ = 27.3 GeV[63]) and Fermilab experiment E605[30] (p+Cu at $\sqrt{s}$ = 38.8 GeV). SeaQuest nuclear target absolute cross section measurement can provide interesting comparison with these measurements and test for scaling.

This thesis is focused on p+d and p+p absolute cross section measurements. p+d absolute measurements were also reported by Fermilab experiment E772 [7, 8] and E866 [4]. These absolute measurements are compared with preliminary cross section measurements from SeaQuest tabulated in Chapter 5. It is crucial to note in the above comparison that the definition of x_F used for E866 and E772 are different from E906. The definition $x_F = 2p_l/\sqrt{s}/(1 - M^2/s)$ used in E906 takes into account the fraction of center of mass

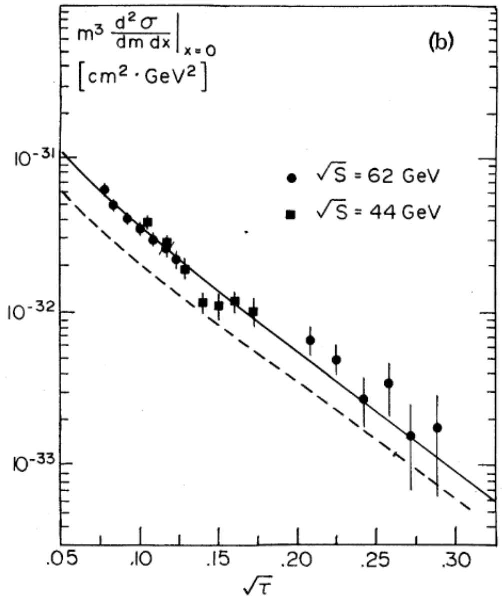

Figure 8.1: Scaling form of cross section from CERN ISR plotted as a function of $\sqrt{\tau}$ for $x = 0$. The figure is taken from [5]

energy $\sqrt{s}$ used up in the mass of dimuon M. The denominator $1 - M^2/s$ or $1 - \tau$ cannot be ignored in the case of SeaQuest where τ values are large enough to not be dropped. Even in the case of E866 or E772, for high mass or high $\sqrt{\tau}$, the x_F value would increase. Table 8.1 shows a tabulation of the change in x_F at different values of M at E866 and E772 $\sqrt{s}$ value. The x_F for low mass (or low $\sqrt{\tau}$) is not affected as much. However, the x_F value for high mass data are affected significantly when SeaQuest definition of x_F is considered. In short, the x_F value would increase if the E906 definition is to be used for E866 or E772 data. Hence, the dimuons contributing to certain x_F bin in the shown figure would migrate to higher x_F bin. Part of the discrepancy between E906 and E866 or E772 can be attributed to the inconsistent definition of x_F being used. Hence, the comparison shown in Figures 8.3 and 8.4 should be repeated by changing the x_F definition in either E906 data or E866/E772 for consistency.

Figure 8.3 shows that for the low x_F regions ($0.05 < x_F < 0.5$), the E906 results are in good agreement with the E866 and E772 results, consistent with ‘scaling’. It is also noteworthy that the E906 data extend the coverage in $\sqrt{\tau}$ to significantly higher values.

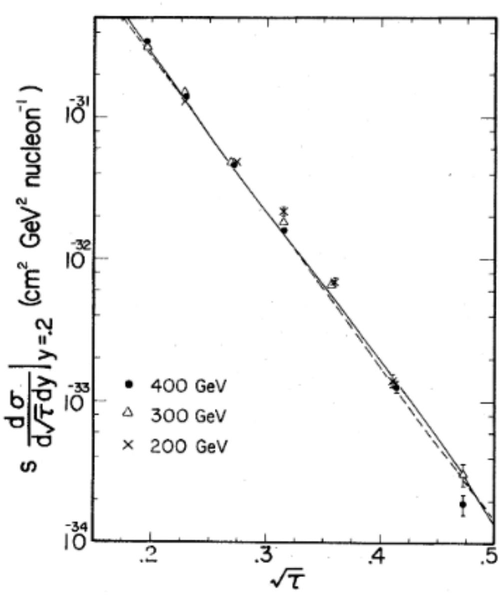

Figure 8.2: Scaling form of cross section from E288 plotted as a function of $\sqrt{\tau}$ for $y = 0.2$. The figure is taken from [6]

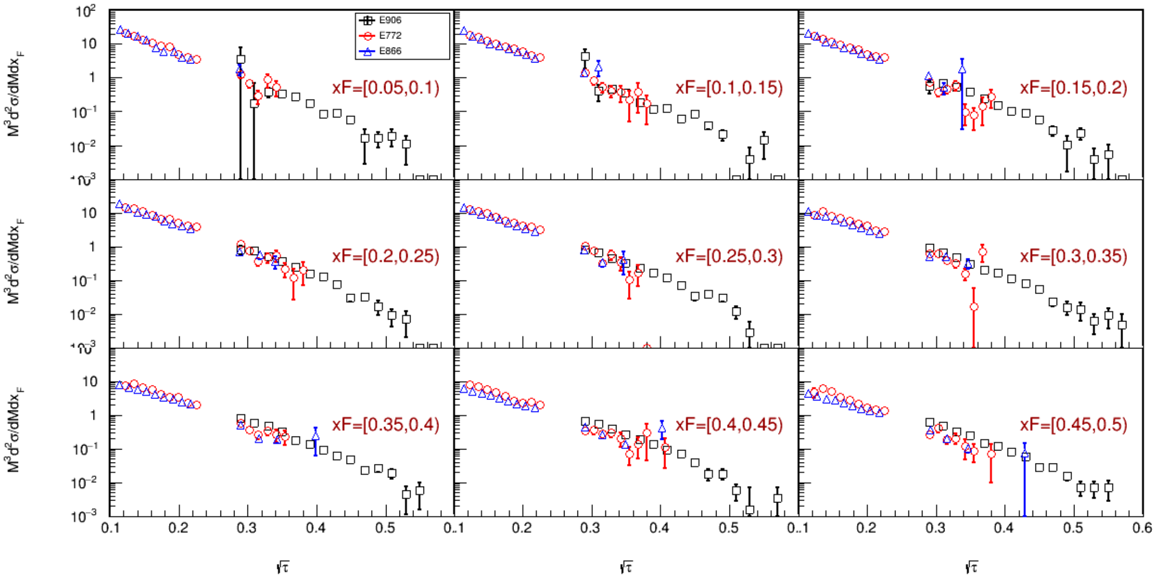

Figure 8.3: p+d scaling form cross section $M^3d^2\sigma/dMdx_F$ plotted Vs $\sqrt{\tau}$ for E866 (open blue triangles)[4], E772 (open red circles)[7, 8] and E906 measurements (open black squares) in x_F range 0.05-0.5. The error bars are statistical. E906 systematic error can be found in chapter 5.

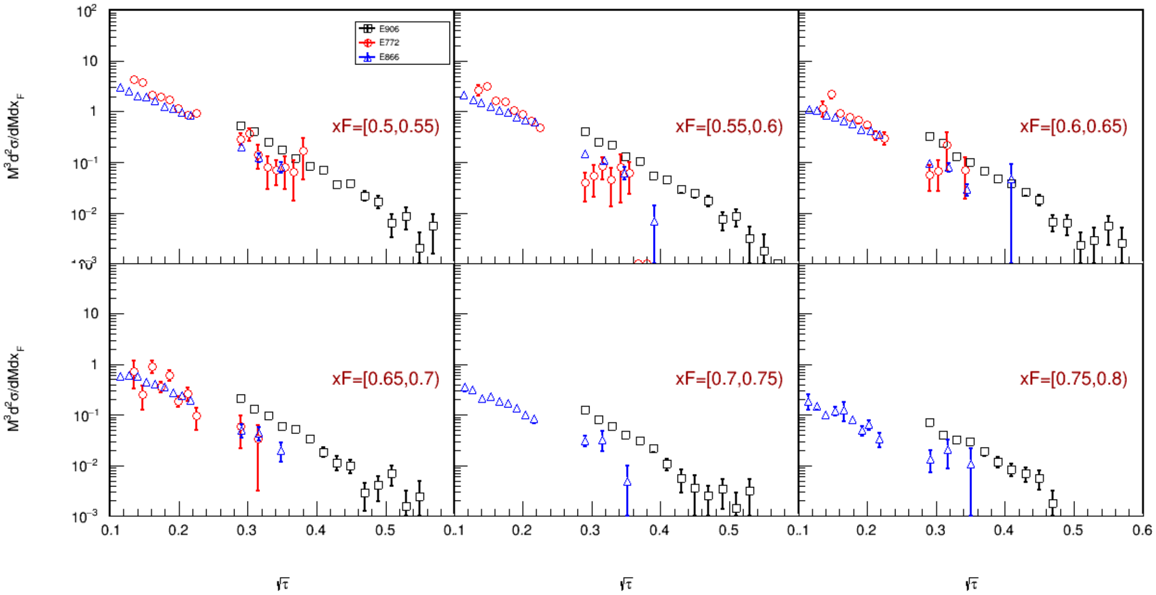

Figure 8.4: p+d scaling form cross section $M^3d^2\sigma/dMdx_F$ plotted Vs $\sqrt{\tau}$ for E866 (open blue triangles)[4], E772 (open red circles)[7, 8] and E906 measurements (open black squares) in x_F range 0.5-0.8. The error bars are statistical. E906 systematic error can be found in chapter 5.

x_F	x'_F					
	M = 5 GeV	M = 6 GeV	M = 7 GeV	M = 8 GeV	M = 11 GeV	M = 13 GeV
0.00	0.00	0.00	0.00	0.00	0.00	0.00
0.05	0.05	0.05	0.05	0.05	0.05	0.06
0.10	0.10	0.10	0.10	0.10	0.11	0.11
0.15	0.15	0.15	0.16	0.16	0.16	0.17
0.20	0.20	0.20	0.21	0.21	0.22	0.23
0.25	0.25	0.26	0.26	0.26	0.27	0.28
0.30	0.31	0.31	0.31	0.31	0.33	0.34
0.35	0.36	0.36	0.36	0.37	0.38	0.39
0.40	0.41	0.41	0.41	0.42	0.43	0.45
0.45	0.46	0.46	0.47	0.47	0.49	0.51
0.50	0.51	0.51	0.52	0.52	0.54	0.56
0.55	0.56	0.56	0.57	0.57	0.60	0.62
0.60	0.61	0.61	0.62	0.63	0.65	0.68
0.65	0.66	0.67	0.67	0.68	0.71	0.73
0.70	0.71	0.72	0.72	0.73	0.76	0.79
0.75	0.76	0.77	0.78	0.78	0.82	0.84
0.80	0.81	0.82	0.83	0.84	0.87	0.90

Table 8.1: Table showing the change in x_F is using the definition as $x'_F = x_F/(1 - M^2/s)$ for M = 5, 6, 7 GeV at $\sqrt{s} = 38.8$ GeV

8.2 p+d/2(p+p) cross section ratios

The main goal of the SeaQuest experiment is to measure the ratio of $\bar{d}/\bar{u}$ up to Bjorken-$x = 0.45$. The ratio $\bar{d}/\bar{u}$ can be accessed by measurement of the cross-section ratio $\sigma_{pd}/2\sigma_{pp}$. Preliminary results on cross section ratio obtained from SeaQuest have been presented in several conferences and thesis [64, 65, 66, 67]. The cross section ratio results have been presented as a single differential in $x_2(x_T)$.

In this section, the method from chapter 4 has been used to obtain cross section ratio as double differential ($d^2\sigma/dx_1dx_2$) by analysing hydrogen and deuterium target in $x_1(x_B)$ and $x_2(x_T)$ bins. Tables 8.2 and 8.3 shows $d^2\sigma/dx_1dx_2$ ($d^2\sigma/dx_Bdx_T$). The ratio $\sigma_{pd}/2\sigma_{pp}$ is shown in figure 8.5. Within statistical uncertainty, there doesn't appear to be any dependence of cross section on $x_1(x_B)$. Addition of data from later runs will enhance the statistical accuracy of the result shown here and will facilitate a better insight into the dependence of cross section ratio on both x_1 and x_2.

	$d^2\sigma/dx_Bdx_T$ ($\times 10^{-2}$)		
x_T bin	$x_B = [0.3, 0.5)$	$x_B = [0.5, 0.6)$	$x_B = [0.6, 0.7)$
0.100-0.130			0.834371 ± 0.068378
0.130-0.160		5.088020 ± 0.359591	3.835650 ± 0.163377
0.160-0.195	3.149650 ± 0.320281	10.696600 ± 0.453850	1.924650 ± 0.076142
0.195-0.240	7.859360 ± 0.503432	5.020560 ± 0.207921	0.751637 ± 0.035928
0.240-0.290	8.871130 ± 0.549769	1.859900 ± 0.100920	0.329766 ± 0.019791
0.290-0.350	4.502340 ± 0.321136	0.860698 ± 0.050343	0.124609 ± 0.010202
0.350-0.450	1.107910 ± 0.119319	0.229091 ± 0.018760	0.029493 ± 0.004700

Table 8.2: Hydrogen Drell-Yan cross section $d^2\sigma/dx_Bdx_T$ (nb) for different x_B and x_T bins. Errors are statistical only.

	$d^2\sigma/dx_Bdx_T$ ($\times 10^{-2}$)		
x_T bin	$x_B = [0.3, 0.5)$	$x_B = [0.5, 0.6)$	$x_B = [0.6, 0.7)$
0.100-0.130			1.897940 ± 0.138847
0.130-0.160		12.717800 ± 0.745401	8.277990 ± 0.286185
0.160-0.195	8.332100 ± 0.645055	22.519000 ± 0.815922	4.407420 ± 0.139311
0.195-0.240	17.763800 ± 0.947621	11.589000 ± 0.371875	1.796310 ± 0.064830
0.240-0.290	18.880000 ± 0.895770	4.279400 ± 0.168207	0.769669 ± 0.034144
0.290-0.350	10.267200 ± 0.528367	1.831810 ± 0.081070	0.279931 ± 0.016803
0.350-0.450	2.441290 ± 0.189815	0.485203 ± 0.031854	0.080462 ± 0.007889

Table 8.3: Deuterium Drell-Yan cross section $d^2\sigma/dx_Bdx_T$ (nb) for different x_B and x_T bins. Errors are statistical only.

Figure 8.5 shows that $\sigma_{pd}/2\sigma_{pp}$ are all greater than unity, consistent with $\bar{d} > \bar{u}$. It is expected that future PDF global fits can include the double differential cross sections of $\sigma(p+d)$ and $\sigma(p+p)$ from this analysis to determine the precise x dependence of $\bar{d}(x)/\bar{u}(x)$ (as well as $\bar{d}(x) - \bar{u}(x)$).

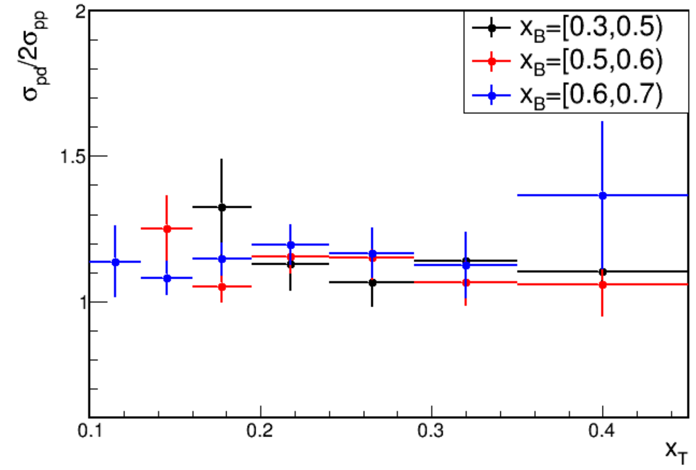

Figure 8.5: $\sigma_{pd}/2\sigma_{pp}$ obtained from ratio of absolute double differential cross section $d^2\sigma/dx_1dx_2$ for p+d and p+p.

Chapter 9

Conclusion and Future Prospects

Since its discovery the Drell-Yan process has been an interesting and active area of research for studying the dynamics of partons and has established its importance for validating QCD as the theory of strong interaction. Several beam types have been utilized to explore PDFs of valence and sea quarks using Drell-Yan mechanism. For example, as proton does not contain valence antiquarks, the Drell-Yan process with a proton beam is sensitive to antiquark (sea) distribution in the target nucleon. On the other hand, beams such as antiproton or pions contain anti-up or anti-down as valence quarks, and these beams are used to probe the valence quark distribution in the target nucleon. Hence, together with DIS data, Drell-Yan measurements play a crucial role in constraining the parton distribution functions (PDFs). Improvements in PDFs help in making more precise predictions for future measurements, which in turn validate and/or further improve the PDFs.

In this thesis, absolute differential cross sections have been obtained from p+p and p+d Drell-Yan interaction measured at SeaQuest (using run II and run III data). These results from SeaQuest cover kinematic region at large x and complement existing Drell-Yan data for future global PDF analysis. The error bands from NLO calculations of cross sections demonstrate large uncertainties in the PDFs at large Bjorken-x. SeaQuest data will have significant impact in constraining both sea and valence quark PDFs, specifically, improved constraints on $\bar{d}(x) + \bar{u}(x)$ together with $\bar{d}(x)/\bar{u}(x)$ measurement will provide better estimate of $\bar{d}(x) - \bar{u}(x)$. Results on Drell-Yan transverse momentum distribution from SeaQuest have also been obtained. These data provide the opportunity to study the p_T distribution at lowest value of $\sqrt{s}$ to date. The dependence of $< p_T >$ on $\sqrt{s}$ is in agreement with QCD predictions that $< p_T >$ increases linearly with $\sqrt{s}$.

Dependence of $< p_T >$ on M and x_F have also been presented. The $< p_T >$ does not show any clear dependence on M which is in agreement with results from existing Drell-Yan data. However, $< p_T >$ shows a clear dependence on x_F, especially for the LD_2 data. The analysis of E866 p+p and p+d data performed in this research also shows this trend. The x_F dependence of $< p_T >$ is also supported by NLO calculations.

The results presented in this thesis include run II and run III data which are approximately 50% of the total collected data at SeaQuest. The analysis of run IV, V and VI data are underway. The data from the later runs are expected to have wider acceptance due to the installation of a new wire chamber aimed to further extend the range in x_T.

The FPGA4 (single muon trigger) data in later runs have been collected with lower prescale value, unlike run II and III data, where the high prescale value resulted in poor statistics in single muon trigger data. With improved statistics, the mix background shape will be more reliable and result in reduced systematic error arising because of the uncertainty in the normalization of mix background.

The absolute measurements provide an opportunity to check for scaling violations in Drell-Yan process. The evidence of scaling violations is observed in DIS measurements, however such an observation remains to seen in DY process. One of the main reasons is that fixed target Drell-Yan process is generally dominated by contribution from valence quark(high-x) annihilating with antiquark from sea (low x). Hence the effect of scaling violation is partially canceling the scaling violation effects. Improved statistical precision and better knowledge of mix background sample will be able to improve the cross section measurements and hence can provide useful insights on scaling violation in Drell-Yan process.

Additionally, better knowledge of mix background normalization and shape will also improve the understanding of transverse momentum distribution from Drell-Yan process. The shape of transverse distribution and hence the mean value of p_T is sensitive to both the shape and normalization of mix background.

Improvements in both statistical and systematic errors will make SeaQuest results, on absolute measurements as well as ratios, a significant contribution in enhancing our knowledge about QCD.

References

[1] J. H. Christenson et al. Observation of massive muon pairs in hadron collisions. *Phys. Rev. Lett.*, 25(21):1523–1526, 1970. xi, 4, 5

[2] L. Isenhower et al. Polarized Drell-Yan Measurements with the Fermilab Main Injector 1. 2019. xii, 37

[3] W. K. Tung. Drell-Yan NLO program, via email. xii, 40, 41

[4] J. C. Webb. Measurement of continuum dimuon production in 800 GeV/c proton-nucleon collisions. *Ph.D. Thesis, New Mexico State University*, 2002. xiv, xv, 8, 13, 106, 107, 120, 137, 139, 140

[5] D. Antreasyan et al. Dimuon scaling comparison at 44 and 62 GeV. *Phys. Rev. Lett.*, 48(5):302–304, 1982. xv, 7, 118, 137, 138

[6] A. S. Ito et al. Measurement of the continuum of dimuons produced in high-energy proton-nucleus collisions. *Phys. Rev. D*, 23(3):604–633, 1981. xv, 106, 112, 118, 137, 139

[7] P. L. McGaughey et al. Cross sections for the production of high-mass muon pairs from 800 GeV proton bombardment of H2. *Phys. Rev. D*, 50(5):3038–3045, 1994. xv, 106, 110, 137, 139, 140

[8] P. L. McGaughey et al. Erratum: Cross sections for the production of high-mass muon pairs from 800 GeV proton bombardment of ^2H [Phys. Rev. D 50, 3038 (1994)]. *Phys. Rev. D.*, 60(11):119903, 1999. xv, 106, 110, 137, 139, 140

[9] E. Rutherford. Collision of particles with light atoms. IV. An anomalous effect in nitrogen. *Philos. Mag.*, 90(SUPPL.1):31–37, 2010. 1

[10] E. Rutherford. LIII. Collision of α particles with light atoms III. Nitrogen and oxygen atoms. *London, Edinburgh, Dublin Philos. Mag. J. Sci.*, 37(222):571–580, 1919. 1

[11] J. Chadwick. The Existence of a Neutron. *Proc. R. Soc. A Math. Phys. Eng. Sci.*, 136(830):692–708, 1932. 1

[12] M. Gell-Mann. A Schematic Model of Baryons and Mesons. *Phys. Lett.*, 8:214–215, 1964. 1

[13] G. Zweig. An SU(3) Model for Strong Interaction Symmetry and its Breaking. *CERN Report No. 8182/TH.401*, 1964. 1

[14] G. Zweig. An SU(3) Model for Strong Interaction Symmetry and its Breaking II. *CERN Report No. 8419/TH.412*, 1964. 1

[15] H. W. Kendall. Deep inelastic scattering: Experiments on the proton and the observation of scaling. *Rev. Mod. Phys.*, 63(3):597–614, 1991. 2

[16] J. D. Bjorken. Asymptotic Sum Rules at Infinite Momentum. *Phys. Rev.*, 179:1547–1553, 1969. 2, 3

[17] M. Breidenbach et al. Observed Behavior of Highly Inelastic Electron-Proton Scattering. *Phys. Rev. Lett.*, 23:935–939, 1969. 3

[18] R. P. Feynman. Very High-Energy Collisions of Hadrons. *Phys. Rev. Lett.*, 23:1415–1417, 1969. 3

[19] S. D. Drell and T. M. Yan. Erratum: Massive lepton-pair production in hadron-hadron collisions at high energies (Physical Review Letters (1970) 25, 13), 1970. 4

[20] S. D. Drell and T. M. Yan. Massive lepton-pair production in hadron-hadron collisions at high energies. *Phys. Rev. Lett.*, 25(5):316–320, 1970. 4

[21] J. K. Yoh et al. Study of scaling in hadronic production of dimuons. *Phys. Rev. Lett.*, 41(10):684–687, 1978. 7, 137

[22] D. Antreasyan et al. Measurement of dimuon production at $s^{1/2}$= 62 GeV. *Phys. Rev. Lett.*, 45(11):863–866, 1980. 8

[23] C. Kourkoumelis et al. Study of massive electron pair production at the CERN intersecting storage rings. *Phys. Lett. B*, 91(3-4):475–480, 1980. 8

[24] I. R. Kenyon. The Drell-Yan process. *Reports Prog. Phys.*, 45:1261–1313, 1982. 8, 36, 118

[25] D. J. Gross and F. Wilczek. Ultraviolet behavior of non-abelian gauge theories. *Phys. Rev. Lett.*, 30(26):1343–1346, 1973. 9

[26] H. D. Politzer. Reliable perturbative results for strong interactions? *Phys. Rev. Lett.*, 30(26):1346–1349, 1973. 9

[27] E. L. Berger, L. E. Gordon, and M. Klasen. Massive lepton pairs as a prompt photon surrogate. *Phys. Rev. D - Part. Fields, Gravit. Cosmol.*, 58(7), 1998. 10

[28] D.A. Ross and C. T. Sachrajda. Flavour symmetry breaking in antiquark distributions. *Nuclear Physics B*, 149(3):497–516, 1979. 13

[29] R. D. Ball et al. Parton distributions for the LHC run II. *J. High Energy Phys.*, 2015(4):1–148, 2015. 13, 71

[30] G. Moreno et al. Dimuon production in proton-copper collisions at $\sqrt{s}$=38.8 GeV. *Phys. Rev. D*, 43(9):2815–2835, 1991. 13, 106, 113, 137

[31] K. Nakano. Check on Cerenkov+QIE Saturation. *SeaQuest doc-db 1417-v2*, 2015. 19

[32] GEANT4 Collaboration. Geant4 user's guide for application developers. http://geant4.web.cern.ch/geant4/UserDocumentation/UsersGuides/ForApplicationDeveloper/html/. 2016. 32

[33] M. Geelhoed. Thickness of the instrumentation package upstream. *SeaQuest doc-db 1092-v1*, 2014. 34

[34] D. M. Kaplan et al. Study of the high-mass dimuon continuum in 400-GeV proton-nucleus collisions. *Phys. Rev. Lett.*, 40(7):435–438, 1978. 36

[35] J. C. Peng et al. $\bar{d}/\bar{u}$ asymmetry and the origin of the nucleon sea. *Phys. Rev. D - Part. Fields, Gravit. Cosmol.*, 58(9):092004, 1998. 36

[36] J. S. Conway et al. Experimental study of muon pairs produced by 252-GeV pions on tungsten. *Phys. Rev. D*, 39(1):92–122, 1989. 37, 55, 106, 116, 120, 122

[37] J. C. Collins and D. E. Soper. Angular distribution of dileptons in high-energy hadron collisions. *Phys. Rev. D*, 16(7):2219–2225, 1977. 37

[38] D. F. Geesaman and T. Chang. Angle Transformation to Photon Rest System. *SeaQuest doc-db 1926-v1*, 1998. 37

[39] F. Coester. Systematic approach to Inclusive Lepton Pair Production. *SeaQuest doc-db 1286*, 1989. 39

[40] S. Catani and M. Grazzini. Next-to-Next-to-Leading-Order Subtraction Formalism in Hadron Collisions and its Application to Higgs-Boson Production at the Large Hadron Collider. *Phys. Rev. Lett.*, 98(22):222002, 2007. 40, 70, 71

[41] S. Catani et al. Vector Boson Production at Hadron Colliders: A Fully Exclusive QCD Calculation at Next-to-Next-to-Leading Order. *Phys. Rev. Lett.*, 103(8):082001, 2009. 40, 70, 71

[42] M. Grazzini et al. http://theory.fi.infn.it/grazzini/dy.html. 2009. 40, 129

[43] S. Prasad. K-factor. *SeaQuest doc-db 1747-v2*, 2016. 40

[44] M. H. Schub et al. Measurement of J ψ and ψ' production in 800 GeV/c proton-gold collisions. *Phys. Rev. D*, 52(3):1307–1315, 1995. 41

[45] S. Prasad. Submitting MC jobs on grid. *SeaQuest doc-db 3049-v2*, 2018. 42

[46] R. E. Kalman. A new approach to linear filtering and prediction problems. *J. Fluids Eng. Trans. ASME*, 82(1):35–45, 1960. 45, 49

[47] K. Nagai. Procedure for making messy MC data. *SeaQuest doc-db 2630-v2*, 2017. 65

[48] S. Prasad. Hodoscope Efficiency. *SeaQuest doc-db 1609-v1*, 2016. 67

[49] D. F. Geesaman. Handling the liquid target contamination and densities. *SeaQuest doc-db 4993-v4*, 2019. 68

[50] C. H. Leung. New mass fit using TFractionFitter. *SeaQuest doc-db 7016-v1*, 2019. 70

[51] M. Geelhoed. SeaQuest Run 1 Beam Intensity Record. *SeaQuest doc-db 457-v2*, 2012. 70

[52] B. Tice and D. Christian. Absolute Normalization - Beam Inhibit and DAQ Deadtime. *SeaQuest doc-db 1212-v3*, 2015. 70

[53] S. Dulat et al. New parton distribution functions from a global analysis of quantum chromodynamics. *Phys. Rev. D*, 93(3):033006, 2016. 71

[54] W. J. Stirling and M. R. Whalley. A compilation of Drell-Yan cross sections. *J. Phys. G Nucl. Part. Phys.*, 19(D):D1–D102, 1993. 106, 118

[55] E. Anassontzis et al. High-mass dimuon production in $\bar{p}$N and π^-N interactions at 125 GeV/ c. *Phys. Rev. D*, 38(5):1377–1403, 1988. 106, 114, 115

[56] M. P. Frazao-Bordalo e Sa. Study of the transverse momentum distribution of muon pairs produced in π-W interactions at 194 and 284 GeV/c. *Ph.D. Thesis, Orsay : Paris Univ.*, 1986. 106, 117

[57] M. Corden et al. Production of muon pairs in the continuum region by 39.5 GeV/c $\pi\pm$, K$\pm$, p and p-beams incident on a tungsten target. *Phys. Lett. B*, 96(3-4):417–421, 1980. 118

[58] M. A. Vasiliev et al. Parton energy loss limits and shadowing in Drell-Yan dimuon production. *Phys. Rev. Lett.*, 83(12):2304–2307, 1999. 119

[59] P. L. McGaughey, J. M. Moss, and J. C. Peng. High energy hadron induced dilepton production from nucleons and nuclei. *Annu. Rev. Nucl. Part. Sci.*, 49(1):217–253, 1999. 119

[60] P. Bordalo et al. Observation of a nuclear dependence of the transverse momentum distribution of massive muon pairs produced in hadronic collisions. *Phys. Lett. B*, 193(2-3):373–375, 1987. 119

[61] C. H. Leung. Private communication. 121

[62] D. de Florian, G. Ferrera, and M. Grazzini. http://theory.fi.infn.it/grazzini/dy.html. 2010. 129

[63] J. Badier et al. Experimental determination of the π meson structure functions by the Drell-Yan mechanism. *Z Phys. C Part. Fields*, 18(4):281–287, 1983. 137

[64] S. Miyasaka. Probing Flavor Asymmetry of Anti-quarks in the Proton by Drell-Yan Experiment SeaQuest. *Ph.D. Thesis, Tokyo Institute of Technology*, 2016. 141

[65] K. Nagai. Recent Measurement of Flavor Asymmetry of Antiquarks in the Proton by Drell–Yan Experiment SeaQuest at Fermilab. *Ph.D. Thesis, Tokyo Institute of Technology*, 2017. 141

[66] B. Kerns. A measurement of the x dependent sea flavor asymmetry at SeaQuest. *Ph.D. Thesis, University of Illinois, Urbana-Champaign*, 2018. 141

[67] A. Tadepalli. Light Anti-Quark Flavor Asymmetry in the Nucleon Sea and the Nuclear Dependence of Anti-Quarks in Nuclei at the SeaQuest Experiment. *Ph.D. Thesis, The State University of New Jersey, Rutgers*, 2019. 141